Laser-Based Thermometry over Long Distances

Teemu Tomberg

School of Electrical Engineering

Thesis submitted for examination for the degree of Master of Science in Technology.

Espoo 25.1.2016

Thesis supervisor:

Prof. Erkki Ikonen

Thesis advisor:

D.Sc. (Tech.) Tuomas Hieta

Aalto University
School of Electrical
Engineering

AALTO UNIVERSITY
SCHOOL OF ELECTRICAL ENGINEERING

ABSTRACT OF THE
MASTER'S THESIS

Author: Teemu Tomberg

Title: Laser-Based Thermometry over Long Distances

Date: 25.1.2016 Language: English Number of pages: 7+72

Department of Signal Processing and Acoustics

Professorship: Optical Technology

Supervisor: Prof. Erkki Ikonen

Advisor: D.Sc. (Tech.) Tuomas Hieta

Electronic distance meters are routinely used in many long-distance applications to accurately determine the distance between two points. Currently, the instruments are reaching towards relative uncertainties of 10^{-7}, the main obstacle being the uncertainty in the refractive index of air. The refractive index is conventionally calculated from the meteorological observations of the ambient air using either Edlén or Ciddor equations. However, the accuracy of these equations is often limited by inaccuracy in the integral meteorological observations. Temperature, which has to be known at ~ 100 mK level, is by far the most significant uncertainty source in many advanced distance measurements making accurate temperature meters a key for improving the quality of modern ranging instruments. A solution is to use laser absorption spectroscopy for non-invasive measuring of the average temperature of air between the two points of interest.

In this thesis, a laser-based thermometer is constructed for accurate determination of the refractive index of air over long distances. The thermometer, which is based on direct absorption spectroscopy of oxygen transition near 770 nm, is demonstrated for the first time in real field conditions up to 864 m in distance in a typical distance measurement configuration. The results prove that the instrument can achieve RMS noise well below 100 mK and accuracy of ± 300 mK using 120 s measurement time, which is to our knowledge the best reported resolution for such a long distance.

Keywords: Temperature, Spectroscopy, Refractice index of air

AALTO-YLIOPISTO
SÄHKÖTEKNIIKAN KORKEAKOULU

DIPLOMITYÖN
TIIVISTELMÄ

Tekijä: Teemu Tomberg

Työn nimi: Laseriin perustuva pitkän matkan lämpötilamittaus

Päivämäärä: 25.1.2016 Kieli: Englanti Sivumäärä: 7+72

Signaalinkäsittelyn ja akustiikan laitos

Professuuri: Optinen teknologia

Työn valvoja: Prof. Erkki Ikonen

Työn ohjaaja: TkT Tuomas Hieta

Elektronisia pituusmittalaitteita käytetään rutiininomaisesti monissa tarkoissa pitkän matkan mittaussovelluksissa. Näistä laitteista parhaimpien suhteelliset mittausepävarmuudet lähestyvät jo suuruusluokkaa 10^{-7}, jossa merkittävimpänä epävarmuuskomponenttina on usein ilman taitekerroin. Taitekerroin lasketaan yleensä säähavaintojen avulla Edlén- tai Ciddor-yhtälöistä, jolloin ilman lämpötilan mittaustarkkuus on usein rajoittava tekijä. Jotta pituusmittauksessa saavutettaisiin suuruusluokkaa 10^{-7} oleva suhteellinen epävarmuus, tulee mitattavan matkan keskimääräinen lämpötila tuntea ~ 100 mK tarkkuudella. Tarkat lämpötilamittaukset ovat siten avainasemassa modernien pituusmittalaitteiden kehityksessä. Mahdollinen ratkaisu on hyödyntää laserabsorptiospektroskopiaa ilman keskimääräisen lämpötilan määrittämiseksi mitattavalla matkalla.

Tässä diplomityössä on toteutettu laseriin perustuva lämpömittari, jonka avulla parannetaan ilman efektiivisen taitekertoimen määrittämistä pitkillä matkoilla. Lämpömittari perustuu suoraan hapen transition absorptiospektroskopiaan lähellä 770 nm aallonpituutta. Instrumentin toiminta havainnollistettiin ensimmäistä kertaa kenttämittauksin aina 864 metrin mittausetäisyyteen asti. Tulokset osoittavat, että laite voi saavuttaa selvästi alle 100 mK kohinatason ja ± 300 mK tarkkuuden käyttäen 120 sekunnin mittausaikaa. Saavutettu resoluutio on tietääksemme paras raportoitu tulos näin pitkälle matkalle.

Avainsanat: Lämpötila, Spektroskopia, Ilman taitekerroin

Preface

I want to thank my advisor D.Sc. (Tech) Tuomas Hieta for his truly excellent guidance and help on this thesis, as well as my co-workers PhD Thomas Fordell and PhD Jari Peltola at VTT Technical Research Centre of Finland Ltd. for their help and answers to my many questions, and Professor Erkki Ikonen from Aalto University School of Electrical Engineering for his help on finishing this thesis. I'm also especially thankful for D.Sc. (Tech) Jorma Jokela from the Finnish Geospatial Research Institute for his expertise in the field of geodesy and guidance during the field measurements of this thesis.

I would also like to thank Professor Ilkka Tittonen from Aalto University School of Electrical Engineering and D.Sc. (Tech) Mikko Merimaa at VTT for making my work in this field of science, proven to be most exciting, possible.

Otaniemi, 25.1.2016

Teemu T. Tomberg

Contents

Symbols and abbreviations

Symbols

α	absorption coefficient
β	Dicke narrowing coefficient
δ	line shift per unit pressure
γ	HWHM
γ'	$1/e$ half width
γ''	FWHM
γ_D	Doppler HWHM
γ_L	Lorentzian HWHM
ν	frequency
A	line area
c	speed of light
d	corrected distance
d'	distance displayed by EDM
D_0	optical diffusion coefficient
d_0	scale correction
d_1	constant correction
E_η	lower state energy
E'_η	calibrated lower state energy
f	focal length
h	Planck's constant
I	received intensity
I_0	initial intensity
K'	first velocity correction
k_B	Boltzmann constant
l	etalon length
L_{OPL}	optical path length
m	molecule mass
n	phase refractive index
n_{ref}	reference refractive index
N_A	Avokadro constant
n_g	group refractive index
N_g	group refractivity
N_L	group refractivity of moist air
n_L	group refractive index of moist air
p	pressure
p_o	partial pressure of dry air
q	volume mixing ratio
Q	total internal partition sum
RH	relative humidity
S	spectral line intensity
T	temperature in Kelvin
t	temperature in Celsius
u	number density of absorbing molecules
w_0	$1/e^2$ beam radius
w_s	spot radius

Operators

$*$ convolution
$\cdot$ multiplication

Abbreviations

DAQ	data acquisition
DFB	distributed feedback
DMM	digital multimeter
EDM	electronic distance meter
EMRP	European Metrology Research Programme
EO-IM	electro-optic intensity modulator
EOM	electro-optic modulator
FGI	Finnish Geospatial Research Institute
FMI	Finnish Meteorological Institute
FSR	free spectral range
FWHM	full width at half maximum
GNSS	global navigation satellite system
GPIB	general purpose interface bus
HWHM	half width at half maximum
IAG	international association of geodesy
NTP	normal temperature and pressure
OPL	optical path length
PD	photodiode
PM	polarisation maintaining
ppm	parts per million
RMS	root mean square
RSD	relative standard deviation
SCM	soft collision model
SI	Système international d'unités
SM	single mode
TDLAS	tunable diode laser absorption spectroscopy
TEC	thermoelectric cooler
WMAS	wavelength modulation absorption spectroscopy

1 Introduction

1.1 Spectroscopy-based laser thermometry

Temperature is one the most important quantities in all fields of natural science as well as in our daily lives. It is a major influencer in many natural phenomena, such as thermal expansion, thermoelectric effect, electrical resistance and piezoelectric effect, which has allowed man to develop an extensive range of different methods for thermometry [1, 2]. Thermometers can be coarsely classified into invasive and non-invasive methods, depending on the nature of contact between the measuring instrument and the object of interest. Invasive methods are the most common including devices such as thermocouples and liquid-in-glass thermometers. Non-invasive methods are often more complex and expensive, but can offer great benefits, for example when measuring objects that can not be disturbed, in high temperature or chemically reactive applications such as combustion gases or plasma. Most of the non-invasive methods exploit the specific properties of the electromagnetic spectrum, such as absorption, emission, scattering or luminescence and are referred to as spectroscopy-based methods. A noteworthy exception to spectroscopy-based methods of non-invasive thermometry is a technique of using propagation speed of ultrasonic bursts [3]. Spectroscopy is a branch of science that studies the interactions between matter and electromagnetic radiation. It is a vast field, including various sub-fields [4], of which tunable diode laser absorption spectroscopy (TDLAS) is treated in this thesis [5, 6].

From a range of spectroscopic methods for gas sensing, absorption-based sensors offer excellent selectivity and sensitivity when a spectrally narrow light source is used to probe a spectrally narrow feature [5, 6]. This has resulted in wide interest on using laser absorption spectroscopy for non-invasive temperature sensing in gases, since it potentially allows fast and continuous *in-situ* monitoring of the object of interest. In recent years, after tunable diode lasers in room temperature became common, a majority of the research has focused on combustion gases of industrial and engine applications at elevated temperatures [7–22]. In addition to temperature, these applications benefit from knowledge of several other combustion parameters, such as mass flux, pressure and velocity, the measurement of which can be implemented in the same spectroscopic instrument. Therefore, it is possible to develop an *all-in-one* combustion gas meter with spectroscopic tools. The combustion environments are often extremely harsh, which is why wavelength modulation absorption spectroscopy (WMAS) with $2f$ detection has gained the most attention [9, 10, 13–16, 18, 19, 21, 22], although direct absorption spectroscopy has also proven successful [8, 20]. In general, the focus has been on rapid measurements of H_2O transitions in the near infrared region, with moderate accuracy and on short distances of 20 m or far less. A drawback in most of the setups has been the optical complexity required by WMAS, a need of constant calibration or use of a known reference gas cell [16, 23]. Also, spectroscopic probing of temperature distributions has been demonstrated using several transitions with different temperature sensitivities [17, 19]. Moreover, to the authors best knowledge, only the earlier research related to this thesis, has reported

spectroscopic measurements of ambient temperature over long distances [24, 25].

1.2 Temperature in long distance measurements

Spectroscopy is a complicated tool and therefore a strong motivation is required for its use. In outdoor or industrial environments, local and rapid variations in temperature are likely to occur. In such conditions, invasive and local or point-based measurement methods of thermometry quickly fail as practical and accurate solution for determining the spatial average temperature over a long path, whereas in the spectroscopic method the averaging is inherent. Such a thermometry is nowadays required when the distance of a long path is measured with optical instruments to a relative uncertainty of as low as 10^{-7} in challenging environments. This level of accuracy is already required for example when constructing and monitoring current and future long-distance tunnel projects or the enormous particle accelerator facilities used in high-energy physics, when establishing local ties between different geodetic instruments on geodetic fundamental stations, or when monitoring crustal deformations at critical sites, such as nuclear power plants or future carbon dioxide repositories [26].

Currently there are in general two different measurement techniques that can be considered when seeking the relative uncertainties of 10^{-7} in distance measurements of several hundreds meters up to kilometres. First, is the Global Navigation Satellite System (GNSS)-based method that determines the distance between two antennas from 3D coordinates inferred from GNSS signal reception. Second, are the Electronic distance meters (EDM) which are based on the direct propagation of an electromagnetic wave between two reference points. The GNSS-based method has, in principle, unlimited range whereas EDM is limited by the visibility of the two points. Neither of the methods, however, is currently capable of achieving traceability to the SI definition of the metre over the required distance and uncertainty in atmospheric conditions. GNSS suffers from various effects, such as signal reflections by the ground, obstacles in the antenna neighbourhood, delays in the ionosphere and troposphere and antenna phase centre variations. These effects are often unpredictable and require independent site calibration, which is time-consuming or even impossible to perform. [26]

EDM on the other hand predominantly suffers from insufficient determination of the effective refractive index of air over the entire measurable distance as the length scale is derived directly from the speed of light. On short fixed distances and in a laboratory environment, optical refractometers can be used to experimentally determine the refractive index to a high accuracy [27]. However, in outdoor or industrial environments one must rely on parameter-based Edlén and Ciddor equations [27–29] which can reach an uncertainty in the 10^{-8} range when the parameters, including temperature, pressure, water vapour concentration and CO_2 concentration, are known to high enough accuracy [27]. Table 1 expresses sensitivity of the refractive index of air to these parameters at 633 nm under standard ambient conditions.

Besides the achievable accuracy of the measurable value in Table 1, one must be concerned about the expected gradients of the environmental variables. Often a

meteorological instrument outputs a result that is a local approximation of the real measurand, whereas determining the effective refractive index over a long distance requires a knowledge of the entire weather profile over the measurement line. The effective refractive index can then be obtained by calculated the refractive index for each point of the profile separately and averaging the results. The above procedure may be simplified by taking the mean of the meteorological measurements before calculating the refractive index ones. This will introduce small errors due to non-linearity of the refractive index equations. In general, for distances up to 1 km in normal weather and ground level, the errors are estimated to be well below 0.01 part per million (ppm), based on example in [30] and additional calculations, and therefore negligible.

Next, requirements of the meteorological measurements should be considered in more detail. Ambient pressure and CO_2 concentrations are generally considered homogeneous and they are readily measured to sufficient accuracy by commercial instruments. However, pressure changes with altitude about 0.12 hPa/m and should be taken into account if the height difference over the line is several meters or more. Moreover, CO_2 concentration can be presumed constant if the measurement environment does not especially encourage otherwise. Humidity is a challenging quantity to measure and it may change significantly over some hundreds of meters if circumstances are unfavourable. A slightest wind however is usually enough to level the differences. Also, humidity has a relatively small effect on the refractive index of air, although it gets elevated at higher, for example in 35 ℃ , temperatures. If nonetheless high gradients in humidity are expected, accurate spectroscopic methods are also available for determining the integral humidity over the measurement distance [31]. In general, local knowledge of the relative humidity with uncertainty of 5 % is sufficient and achievable using standard weather stations.

Similarly to humidity, temperature can experience strong gradients [32] and the refractive index is rather sensitive to its variations. In most cases, the uncertainty in the refractive index of air is dominated by the uncertainty in temperature [32]. Traditionally, temperature has been determined at one or both terminals of the measurement line with conventional invasive thermometers, such as mercury-in-glass, platinum resistance or electronic thermometers. For short distances, for example below 1 km, the meteorological measurements are often only taken at the instrument station [30]. However, in demanding meteorological applications, a dense array of such thermometers along the line is also in use [32]. The traditional procedure works well in some cases, such as when measuring in laboratory, outdoors in favourable weather conditions and generally over short distances close to ground level. For challenging conditions, experimental and theoretical models based on various observations, such as weather, time of day and elevation angle of the sun, have been developed for improved compensation of the refractive index of air. These models try to predict for example the turbulences and temperature gradients at different altitudes, caused by heat transfer between air and ground [30]. However, on distances up to kilometres or in especially challenging environments, even a dense array of thermometers may not always lead to accurate enough approximation of the effective refractive index of air or it becomes very impractical. In such cases, a laser-based method has proven to be

a viable solution [25].

Table 1: Variation in temperature, pressure, relative humidity and CO_2 concentration that will results in 10^{-7} increase in the refractive index of air under standard ambient conditions. Results are based on the modified Edlén's formula at wavelength of 633 nm.

Parameter	Temperature	Pressure	Relative Humidity	CO_2 Conc.
Nominal Value	20 ℃	1013 hPa	50 %	400 ppm
Difference	-0.11 ℃	+0.37 hPa	-11.6 %	+690 ppm

The appropriate refractive index of air in optical distance measurement depends on the operation principle of the instrument. A displacement measuring interferometer requires phase refractive index, whereas a ranging instrument, measuring the propagation delay of optical pulses, requires the group refractive index. The phase index describes the velocity of an individual phase front and group index the velocity of the envelope of the pulse. When the dispersion is small, the two are linked by the following relation

$$n_g = n + \nu \frac{\mathrm{d}n}{\mathrm{d}\nu}, \tag{1}$$

where n is the phase refractive index and ν the frequency [29]. Although the aforementioned modified Edlén's formulae and the results in Table 1 are for phase refractive index, the results hold true for the group index as well. The International Association of Geodesy (IAG) recommends using the computer procedure by Ciddor & Hill in determining the group refractive index of air for electronic distance measurements [28, 29, 33]. This thesis uses the simpler approximative formula, recommended by IAG, to determine the refractive index of air. The procedure and the equations for calculating the approximative refractive index are repeated here for convenience [33]

$$N_g = (n_g - 1)10^6 = 287.6155 + \frac{4.88660\,\mathrm{m}^2}{\lambda^2} + \frac{0.06800\,\mathrm{m}^4}{\lambda^4} \tag{2}$$

$$N_L = (n_L - 1)10^6 = \left(\frac{273.15\,\mathrm{K}}{1013.25\,\mathrm{hPa}} \cdot \frac{N_g p}{T}\right) - \frac{11.27 \frac{\mathrm{K}}{\mathrm{hPa}} p_s}{T}. \tag{3}$$

Equation 2 is an approximation for the group refractivity of air N_g with 375 ppm CO_2 content at temperature of $T = 273.15$ K, pressure of $p = 1013.15$ hPa and partial water vapor pressure of $p_s = 0.0$ hPa. Changes in pressure, temperature and humidity can be accounted with Equation 3, where N_L is the group refractivity of moist air and n_L the corresponding refractive index. These estimates deviate, for example, less than 0.25 ppm from the accurate Ciddor formulation between -30 ℃ and +45 ℃, at 1000 hPa pressure, 100% relative humidity and for wavelength

of 650 nm and 850 nm [33]. The accuracy of the approximation is enough for the resolution of the spectroscopic instrument in this thesis, as discussed in Section 6.

1.3 Contribution of this thesis

The European Metrology Research Programme (EMRP) project SIB60 Surveying, related to this thesis, focuses on reducing the uncertainty of the scale in long-distance metrology for measurements up to 1 km and fostering traceability to the SI units. The contribution of this thesis relates to the optical measurement in air, in particular on the in-line compensation of the refractive index along the entire beam path with a targeted relative uncertainty of 10^{-7} over a distance of 1 km. The goal is to determine the average temperature of the air volume traversed by a laser beam of the measuring instrument to best possible accuracy and precision, preferably to 100 mK.

To accomplish this goal, a laser-based thermometer based on direct absorption spectroscopy of oxygen, referred to as "Oxytherm" from now on, was constructed at the Centre for Metrology and Accreditation (Mittatekniikan keskus, MIKES), which is part of VTT Technical Research Centre of Finland Ltd. The work in this thesis included construction of a new laser-based thermometer and development of methods to analyse the data. In addition, the performance of the setup was evaluated in laboratory and, especially, in an outdoor measurement campaign at Nummela standard baseline in Vihti, Finland, at the end of September 2015 for distances up to 864 m.

The reminder of this thesis is organized in the following way. Section 2 explains the principles of absorption spectroscopy and how it can be used for thermometry. Section 3 describes in detail the optics, electronics and software comprising the experimental setup. Section 4 outlines the field measurements that were performed to validate and evaluate the performance of the thermometer. Section 5 describes the data analysis methods and calibration of the instrument. The results of the field measurements are presented and discussed in Section 6 and conclusions, together with an outlook, is provided in Section 7.

2 Absorption spectroscopy

Absorption spectroscopy refers to a range of techniques, often employed in fields such as analytical chemistry, molecular physics and astronomy, which often determine the presence or amount of substance in a sample by measuring the absorption of electromagnetic radiation as a function of wavelength. Most of the earliest methods were based on a monochromator and broad-spectrum light sources, whereas nowadays monochromatic laser techniques, including TDLAS, are commonly used.

This section explains the principles of absorption spectroscopy that are relevant in the experimental study of this thesis. The chosen method of spectroscopy allows measurement of the absorption line-profile of a certain transition of gaseous oxygen in air (subsections 2.1 and 2.2), which in return allows determination of the average temperature of the absorbent molecules, explained in Subsection 2.3. Major factors affecting the line-profile and temperature solution are also explained in this subsection. Selection of the oxygen transition, best suited for the application, is explained in Subsection 2.4.

2.1 Absorption of light

In optical measurements intensity of incident light is often the only observable that can be directly measured. With calculations, also other properties can be discovered, such as the optical absorption coefficient α. The absorption coefficient is a fundamental quantity in spectroscopy describing a relation between initial and received intensities I_0 and I, respectively. This relationship is commonly known as the Beer-Lambert law, given as

$$I = I_0 e^{-\alpha L_{OPL}}, \tag{4}$$

where L_{OPL} is the optical path length (OPL). The absorption coefficient is commonly expressed in dimension of cm^{-1} and OPL in cm in order to match with the spectroscopic wave number unit cm^{-1}.

The Beer-Lambert law shows its usefulness when the absorption coefficient is expressed as a function of number density of absorbing molecules u [molecules/cm^3], the normalized line shape function $f(\nu, \nu_{\eta\eta'}, T, p)$ [$1/\mathrm{cm}^{-1}$] and the spectral line intensity $S_{\eta\eta'}(T)$ [cm^{-1}/(molecule cm^{-2})] as [34]

$$\alpha_{\eta\eta'}(\nu, T, p) = u(T, p)\, S_{\eta\eta'}(T)\, f(\nu, \nu_{\eta\eta'}, T, p). \tag{5}$$

Equation 5 holds true for a single transition at frequency $\nu_{\eta\eta'}$ between lower and upper states η and η', with p being the pressure, T the temperature and ν the wave number. The number density $u(T, p)$ of absorbing molecules per unit path length can be derived from the ideal gas law as in Equation 6

$$u(T, p) = \frac{q\, p}{k_B\, T}, \tag{6}$$

where q is the volume mixing ratio and k_B the Boltzmann constant. For moist air, p is the partial pressure of dry air and q approximately 0.2095 in the case of oxygen.

Thus, by measuring the absorption as a function of frequency ν the line-profile, and many other quantities, can be determined.

2.2 Line-profiles

The Bohr condition states that in order for absorption to take place the incident light must have a frequency that satisfies $\nu = (E_{\eta'} - E_{\eta})/h$, where $E_{\eta'}$ and E_{η} are energies of the involved energy states, and h is the Planck's constant. This condition implies that the exciting light would need to exactly match the energy difference of the states, which has been found not to be true. In reality, a range of frequencies will be effective and a transition has a line-profile $f(\nu)$ that is a result of several broadening mechanisms, including Doppler- and pressure broadening which are treated in this thesis, as well as the natural line width.

A line-profile is characterised by line width, which is most commonly expressed as half width at half maximum (HWHM) in units of cm^{-1}. Also such values as full width at half maximum (FWHM) and $1/e$ half width (occasionally also $1/e^2$) are extensively used to describe a line width. This thesis shall denote the HWHM by γ, which relates to 1/e half width, in the case of Gaussian line-profile, by $\gamma' = \gamma/\sqrt{\ln 2}$ and to FWHM by $\gamma'' = 2\gamma$.

Collisions between atoms or molecules in pressurized gas causes them to decay prematurely from their exited state. These events lead to shortened life time of the excited state thus broadening the absorption profile. This phenomenon, known as pressure broadening, has a Lorentzian line shape and is a dominant broadening mechanism in the lower atmosphere. The normalized Lorentzian profile is defined as [5]

$$f_L(\nu, \nu_{\eta\eta'}, T, p) = \frac{1}{\pi} \frac{\gamma_L(p,T)}{\gamma_L(p,T)^2 + (\nu - \nu_{\eta\eta'})^2}, \tag{7}$$

where p denotes pressure, T temperature and $\nu_{\eta\eta'}$ the centre frequency. Although also some other homogeneous broadening mechanisms has Lorentzian line shapes, it is not necessary to consider them separately as their contribution can be added to the Lorentzian line width γ_L. One of these is the natural line width, which arises from the finite life time of the excited states according to the uncertainty principle, and is the fundamental minimum of the transition line width.

Doppler broadening is an inhomogeneous mechanism caused by thermal motion of molecules. Its extent depends on the relative motion between an absorbing particle and an incident photon, which gives rise to a Doppler shift in the absorbed light. The broadening is not equal to all molecules in a gas and is thus characterized by a Gaussian line-profile, the normalized version of which is defined as [5]

$$f_D(\nu, \nu_{\eta\eta'}, T) = \frac{\sqrt{\ln 2}}{\gamma_D(T)\sqrt{\pi}} e^{-\ln 2 \left(\frac{\nu - \nu_{\eta\eta'}}{\gamma_D(T)}\right)^2}. \tag{8}$$

The line-profile that accounts for both Doppler and collisional broadening is called the Voigt profile. It is defined as a convolution of the Lorentzian and Gaussian profiles as [5]

$$\begin{aligned} f_V(\nu, \nu_{\eta\eta'}, T, p) &= f_D(\nu, \nu_{\eta\eta'}, T) * f_L(\nu, \nu_{\eta\eta'}, T, p) \\ &= \frac{\gamma_D}{\gamma_L \pi}\sqrt{\frac{\ln 2}{\pi}} \int_{-\infty}^{+\infty} \frac{e^{-\ln 2\left(\frac{\nu-\nu'-\nu_{\eta\eta'}}{\gamma_D(T)}\right)^2}}{\gamma_L(p,T)^2 + (\nu' - \nu_{\eta\eta'})^2}. \end{aligned} \tag{9}$$

Several numerical approximations are available in the literature for rapid and accurate calculation of the Voigt profile. This thesis uses one provided by Abrarov et al. [35] that is an improved version of the Humlíček algorithm [36].

In some cases, including this thesis, an even more elaborate description of the absorption line can be useful. The Voigt profile does not take into account the collision induced velocity changes, which will narrow the Voigt profile especially in low pressure [5]. This so called Dicke narrowing can be taken into consideration in different ways, using statistical models of the collisions. Most commonly known is the Galatry profile, also termed the soft collision model (SCM). The SCM assumes that the velocity of the absorber after the collision strongly correlates with that prior to the collision, implying that the collision absorbers are heavy related to the perturbers. An opposite model would be the Rautian line shape function, also called the hard collision model [37]. This thesis uses the standardized form of the SCM given as [37–40]

$$G(x', y, z) = \frac{1}{\pi\gamma'_D}\mathrm{Re}\left[\frac{1}{\frac{1}{2z} + y - ix'} M\left(1; 1 + \frac{1}{2z} + \frac{y - ix'}{z}; \frac{1}{2z^2}\right)\right]. \tag{10}$$

Here M is the confluent hypergeometric function that can be calculated rapidly using a numerical approximation. In Matlab *kummer*[1] function is available. The three dimensionless parameters x', y and z are described as follows:

$$x' = \frac{\nu - \nu_{\eta\eta'}}{\gamma'_D} - \frac{\delta}{\gamma'_D} p, \tag{11}$$

$$y = \frac{\gamma_L}{\gamma'_D} p, \tag{12}$$

$$z = \frac{k_B\, T\, p}{2\pi\, c\, m\, \gamma'_D\, D_0}, \tag{13}$$

where k_B is the Boltzmann constant, m the molecule mass, c the speed of light, D_0 the optical diffusion coefficient and δ the line shift per unit pressure, which can be neglected as the absolute frequency was not interesting in the measurements. The diffusion coefficient is a function of temperature and some constants related to the gas species. For O_2 molecules in normal temperature and pressure (NTP) air its

[1] Available online: http://www.mathworks.com/matlabcentral/fileexchange/29766-confluent-hypergeometric-function/content/kummer.m

value is $D_0 \approx 0.2$ cm^2/s and can be considered constant as the Galatry profile is quite insensitive to its expected variations [41, 42]. The Doppler half width can be determined using

$$\gamma_D = g_0 \, \nu_{\eta\eta'} \sqrt{\frac{T}{N_A \, m}}, \tag{14}$$

where $g_0 = 3.58 \cdot 10^{-7} \sqrt{\frac{\text{g}}{\text{K mol}}}$ and N_A is the Avokadro constant [5].

In addition to the theoretical calculation of the z-parameter, it can be determined using experimental data obtained for example by Robichaud *et al.* [43]. They measured a Dicke narrowing coefficient of $\beta = 0.0197$ cm^{-1}atm^{-1} [2] for the transition used in the experimental work of this thesis. The narrowing coefficient β is more frequently used in theoretical literature than the z-parameter, and it is related to the Doppler width as $z = \beta \, p / \gamma'_D$ [44]. The theoretical value is in good agreement with the experimental results.

Figure 1 illustrates how the presented line-profiles compare to each other. In the figure, all the profiles are normalized to unit area, and the half widths are set equal. In practise, the suitability of each profile to the measurement data is best evaluated by examining the residuals as in Section 5.

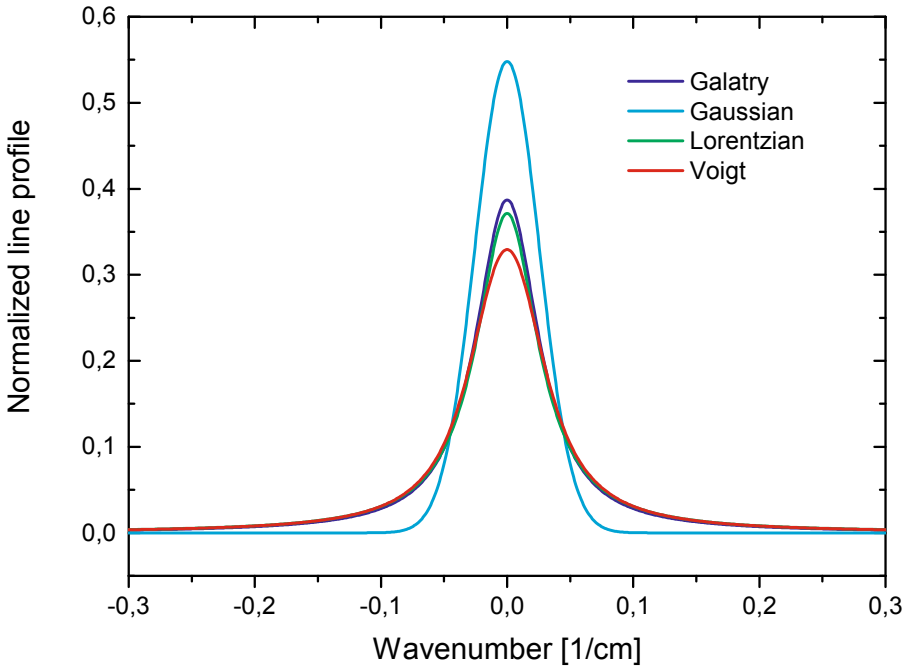

Figure 1: Different line-profiles of equal 0.03 cm^{-1} half widths and areas normalized to one.

[2] Note: cm^{-1}atm^{-1} = 0.295872 MHz/Pa

2.3 Thermometry using laser spectroscopy

A gas in equilibrium has its energy levels populated according to the Boltzmann distribution that is essentially a function of temperature. If a transition from a lower state η to an upper state η' has probability of P, then after a temperature change the transition would have a probability of P' that can be predicted by the Boltzmann distribution. Therefore, spectral line intensity, a fundamental spectroscopic property of the absorbing species, can used to deduce the gas average temperature as long as the gas follows the Boltzmann distribution, which in general is true. The temperature dependent spectral line intensity $S_{\eta\eta'}(T)$ is

$$S_{\eta\eta'}(T) = S_{\eta\eta'}(T_{ref})\frac{Q(T_{ref})}{Q(T)}\exp\left(-\frac{hcE_\eta}{k_B}\left(\frac{1}{T}-\frac{1}{T_{ref}}\right)\right)\frac{1-\exp\left(\frac{-hc\nu_{\eta\eta'}}{k_BT}\right)}{1-\exp\left(\frac{-hc\nu_{\eta\eta'}}{k_BT_{ref}}\right)}, \quad (15)$$

where $S_{\eta\eta'}(T_{ref})$ is the line intensity at a reference temperature, h is the Planck constant, c is the speed of light, k_B is the Boltzmann constant, $Q(T)$ is the total internal partition sum and E_η is the lower state energy [34, 45]. The third factor on the right side of Equation 15 accounts for the ratio of Boltzmann populations. The fourth factor accounts for the effect of stimulated emission, which is negligible at wavelengths below 2.5 μm and temperatures below 2500 K [7].

The temperature of an absorbing gas can be determined using measured absorption in Equation 5 and known values of $S_{\eta\eta'}(T_{ref})$, E_η and $u(T,p)$. When performing the most accurate outdoor thermometry, environmental changes affecting the number density of absorbing molecules has to be taken into account. In normal expected weather conditions, temperature, pressure and relative humidity can change significantly during a day. Temperature and pressure variations affect the number of absorbing molecules directly through the ideal gas law and humidity by changing the atmospheric composition. A good approximation is that the composition of dry air stays constant. Hence, the partial pressure of dry air can be calculated as $p_o = p - p_s\,RH$, where RH is the measured relative humidity and p_s is the saturation vapour pressure of water approximated by the Arden Buck equation

$$p_s = 6.1121\,\text{hPa}\exp\left[\left(18.729-\frac{t}{227.3\,^\circ\text{C}}\right)\frac{t}{t+257.87\,^\circ\text{C}}\right], \quad (16)$$

where $t = T - 273.15$ is the temperature in Celsius [46].

In this thesis, the average temperature T of the gas along the absorbing path was numerically solved using equations

$$A = S'_{\eta\eta'}(T_{ref})\,L_{OPL}\,u(p_{ref},T_{ref})\frac{Q(T_{ref})}{Q(T)} \cdot \exp\left[-\frac{hcE'_\eta}{k_B}\left(\frac{1}{T}-\frac{1}{T_{ref}}\right)\right]\frac{1+\frac{p-p_s(T)RH-p_{ref}}{p_{ref}}}{1+\frac{T-T_{ref}}{T_{ref}}}, \quad (17)$$

$$
\begin{aligned}
Q(T) &= g_1 + g_2 \cdot T + g_3 \cdot T^2 + g_4 \cdot T^3, \\
g_1 &= 0.35923, \\
g_2 &= 0.73534\,\mathrm{K}^{-1}, \\
g_3 &= -0.6487 \cdot 10^{-4}\,\mathrm{K}^{-2}, \\
g_4 &= 0.13073 \cdot 10^{-6}\,\mathrm{K}^{-3},
\end{aligned}
\tag{18}
$$

where A is the measured line area, which was determined from the measurements by fitting the Galatry line-profile to the absorption profile. $S'_{\eta\eta'}(T_{ref})$ and E'_η are the calibrated values of $S_{\eta\eta'}(T_{ref})$ and E_η that include all system dependent unknown constants, such as temperature dependencies and systematic error in L_{OPL}. The total internal partition sum Q is approximated with a third order polynomial in Equation 18 according to calculations by Gamache *et al.* [45]. The reference value of the partial pressure of dry air is designated by p_{ref} and calculated as $p_{ref} = p'_{ref} - p_s(T_{ref})RH_{ref}/100$ with p'_{ref}, RH_{ref} and T_{ref} being reference values, chosen to be 1013 hPa, 50 % and 296 K respectively. the molecule density evaluated at the reference pressure and temperature is designated by $u(p_{ref}, T_{ref})$. The last factor in Equation 17 accounts for the environmental corrections to the molecule density. The corrections can qualitatively understood as follows. Increasing temperature makes the gas more sparse through increased thermal motion so the line intensity must decrease. Pressure on the other hand behaves inversely. Higher pressure makes the gas more dense so the line intensity must increase.

Uncertainty estimates for pressure, humidity and length measurements, which are necessary for an uncertainty of 100 mK in the obtained temperature, are presented in Table 2. The values are only approximative as their effect on temperature is not strictly linear and specific conditions always affect the solution. The nominal values of the parameters were selected so that they best reflect the conditions in the measurements of this thesis.

Besides the presented temperature solving method based directly on spectral line intensity, it is possible to determine the temperature using absorption peak value or intensity ratio of two absorption lines [47]. The peak value method together with baseline measurement is computationally relatively simple. Unfortunately, it suffers intensely from dependence on pressure changes. In addition, any random interferences on the absorption peak would distort the measurement. The method is therefore considered unsuitable for long distance field measurements. The ratio measurement is robust against environmental changes, interferences and has been mostly used in the recent studies [7–22]. It can also achieve great sensitivity if the two transition are well chosen. However, the needed laser system for measuring two lines is more complicated and the relative intensity drifting of the laser diodes can pose a problem. Moreover, in the application of this thesis, suitable absorption lines were not available for the intended long distance.

Table 2: Variation in pressure, relative humidity or distance and their effect on the obtained temperature. The reference parameters are as listed above and the transition specific parameters are $E'_\eta = 1245.3\,\mathrm{cm}^{-1}$ and $S'_{\eta\eta'}(T_{ref}) = 9.16 \cdot 10^{-26}\,\mathrm{cm}^{-1}/(\mathrm{molecule\ cm}^{-2})$. The parameters were selected so that they result in nominal temperature value of 15.00 ℃. As a first order approximation, changes in multiple parameters can be approximated by a linear combination of individual changes.

Parameter Nominal Value	Pressure 1014 hPa	Relative Humidity 64 %	Distance 860.5 m	Temperature 15.00 ℃
Difference	-1.4 hPa	-	-	100 mK
Difference	-	8.2 %	-	100 mK
Difference	-	-	-1.2 m	100 mK
Difference	-	-	-1.0 m	84 mK
Difference	-	10 %	-	123 mK
Difference	-1 hPa	-	-	71 mK

2.4 Line selection

For the proposed method of spectroscopic thermometry, on path lengths up to 1 km, a magnetic-dipole transition of O_2 *A*-band [48] at 12999.96 cm^{-1} (769.23 nm) was found suitable for the task. The selection was based on results of spectral simulations using line parameters from the HITRAN[3] 2012 database [49]. Multiple criteria were taken into account, such as availability of suitable light sources and optical components, transition spectral intensity and its sensitivity to temperature. The results of the simulations are presented in Figures 2, 3 and 4.

Of all major atmospheric gases (N_2, O_2, Ar, CO_2 and H_2O) oxygen was found most suitable for spectroscopic thermometry as its expected concentration in ambient conditions is near constant (unlike water's) and it has suitable transitions in the A-band, which are on relatively short wavelengths and reasonably well isolated from transitions of other molecules (unlike N_2, Ar and CO_2). The issue with wavelength is that high quality lasers and optical components need to be available. CO_2 has suitable transitions near the telecom region (close to 1550 nm), where good quality optics are abundant, and it would be a good alternative if the CO_2 concentration in atmosphere were more stable. Also, the beam divergence would be significantly higher on the longer wavelengths.

As Figure 2 shows, most of the transitions near the centre of the oxygen A-band are practically fully saturated on the intended 1 km OPL. Some weak transition with good temperature sensitivities exist on the shorter wavelength end, as the two shown in Figure 3, where the temperature sensitivity is defined as an absolute change

[3]Further information on HITRAN available from their website: www.hitran.com

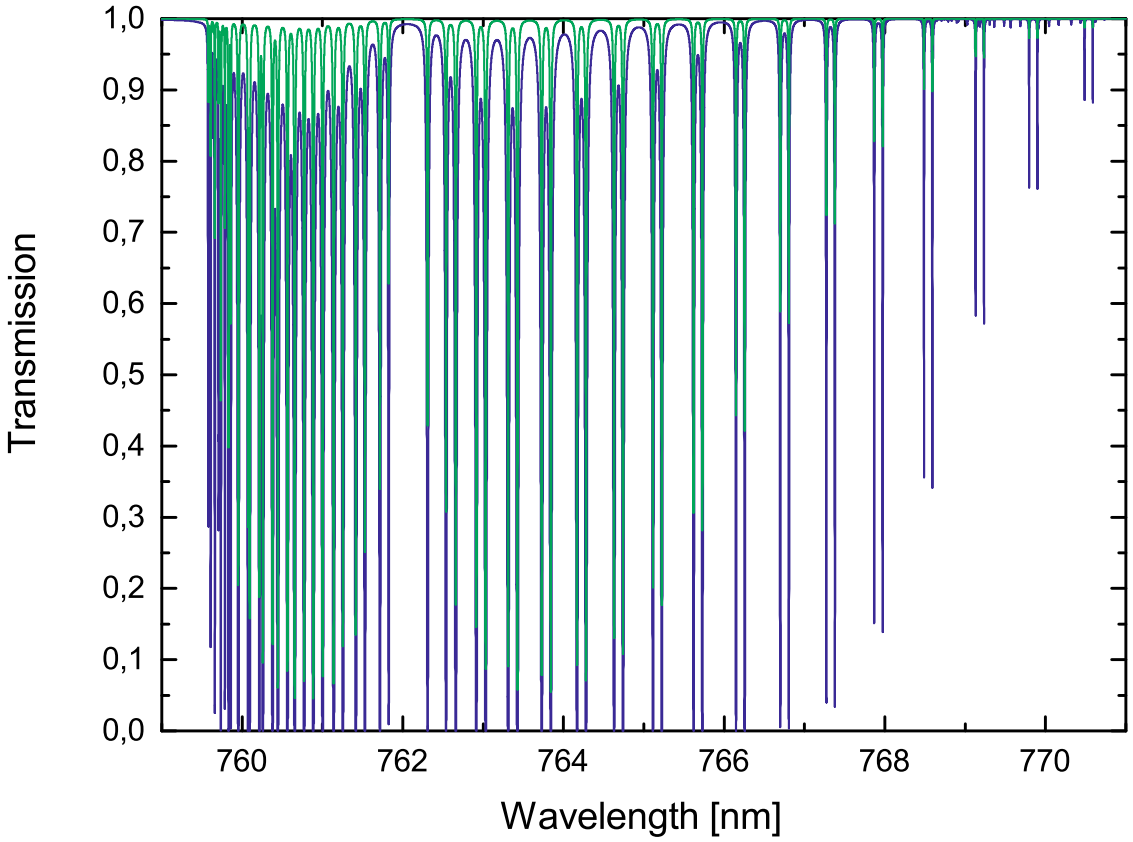

Figure 2: Simulated transimission of oxygen A-band in dry air (20.95 % O_2, 1013 hPa, 296 K) for 1000 m optical path length. Overlaid with green is the same spectrum simulated on a 100 m optical path length.

in the peak transmission, positive values meaning decrease in transmission. Either of the two weak transition, with temperature dependencies shown, can be used for spectroscopic thermometry, although the analysis due to spectral interference would be more complex than in the case of well isolated transition. On the other hand, well isolated and sufficiently weak transitions with similar temperature dependency can be found at the longer wavelength end of the A-band as depicted in Figure 4. The transition indicated by green arrow was chosen for its optimal line intensity and based on availability of high quality lasers. The simulated temperature sensitivity for the transmission of the transition is 0.53%/K, which translates to relative change of 1.7%/K in the line intensity. For sensing temperature changes of 0.1 K or less, the instrument would need to be sensitive enough to measure relative changes better than 0.17% in the line intensity. Some of the HITRAN 2012 database values for the selected transition are listed in Table 3 [49].

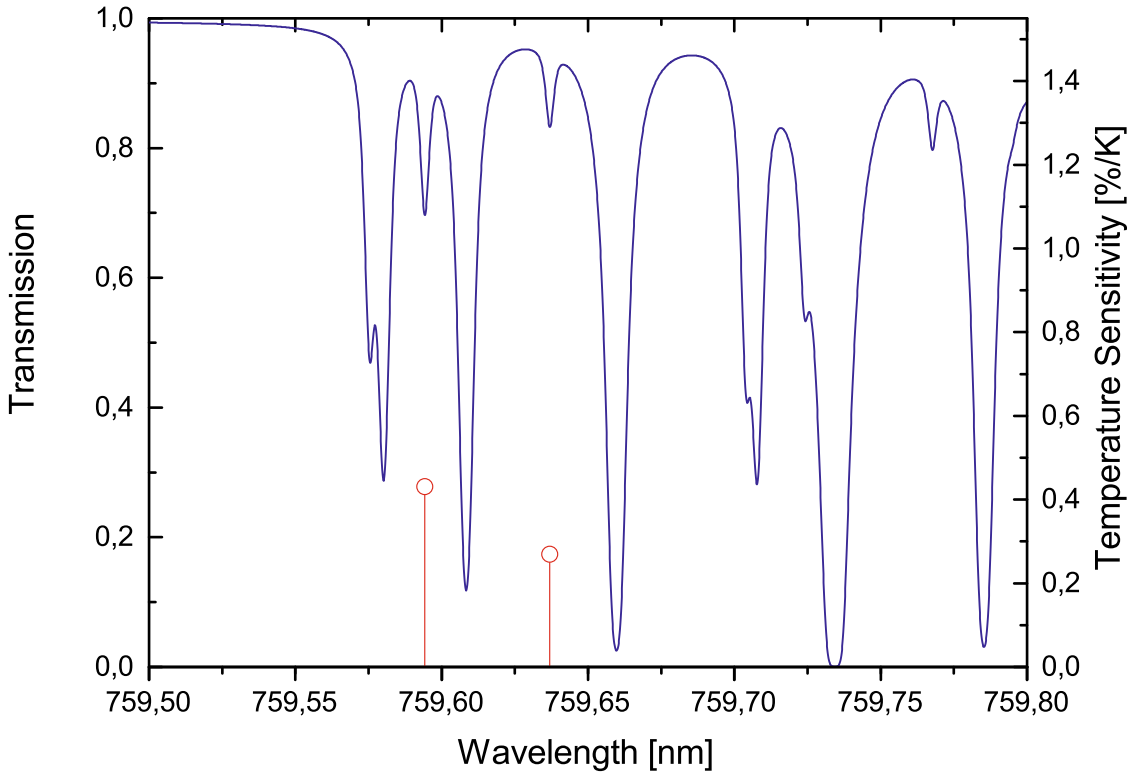

Figure 3: Close up of the simulated oxygen A-band in Figure 2 for 1000 m optical path length. The absolute change in transmission as a function of temperature is indicated by the red drop lines, positive values meaning decrease in transmission.

Table 3: Selection of HITRAN 2012 parameters for the oxygen transition, used in the experiments of this thesis. Abbreviation MOL stands for molecule. Note: $\mathrm{cm}^{-1}\mathrm{atm}^{-1} = 0.295872\,\mathrm{MHz/Pa}$

	Parameters	Value
ν	Vacuum wave number	12999.956891 cm^{-1}
S	Intensity at standard 296 K	$1.099 \cdot 10^{-25}\mathrm{cm}^{-1}/(\mathrm{MOL\ cm}^{-2})$
γ_{air}	Air-broadened HWHM at 296 K	0.0332 cm^{-1} atm^{-1}
γ_{self}	Self-broadened HWHM at 296 K	0.0350 cm^{-1} atm^{-1}
E''	Lower-state energy	1248.2031 cm^{-1}
n	Temperature-dependent exponent for γ_{air}	0.63
δ	Air pressure-induced line shift at 296 K	-0.009200 cm^{-1} atm^{-1}
Q''	Lower-state "local" quanta	P29 P29

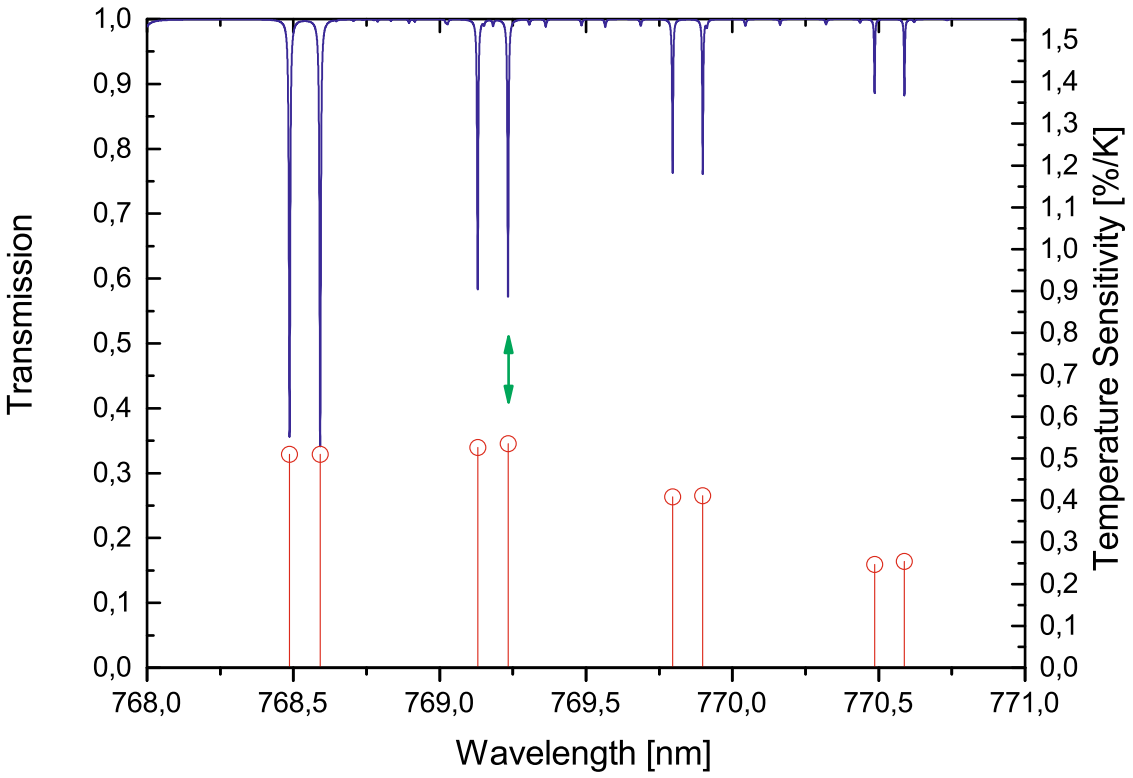

Figure 4: Close up of the simulated oxygen A-band in Figure 2 for 1000 m optical path length. The relative change in transmission as a function of temperature is indicated by the red drop lines, positive values meaning decrease in transmission. The green arrow points out the chosen line.

3 Instrumentation

This section explains in detail the optical, electronic and programmatic methods that were used in performing the measurements of this thesis. The methods follow the same principles as in [24] and [25]. However, several refinements have been made to a more simple and robust design. The final measurement configuration, used in field measurements, is outlined in Figure 5. The main components are, starting from the left: weather station, rack cabinet, transmission (Tx) end tripod, receiving (Rx) end tripod and receiver electronics box. All the Tx electronics, optics and computer were built inside the rack cabinet and the Rx electronics box contained only batteries and simple electronics required to send the photo detector signal back to the Tx end.

In the following subsections, the components of the configuration are thoroughly explained.

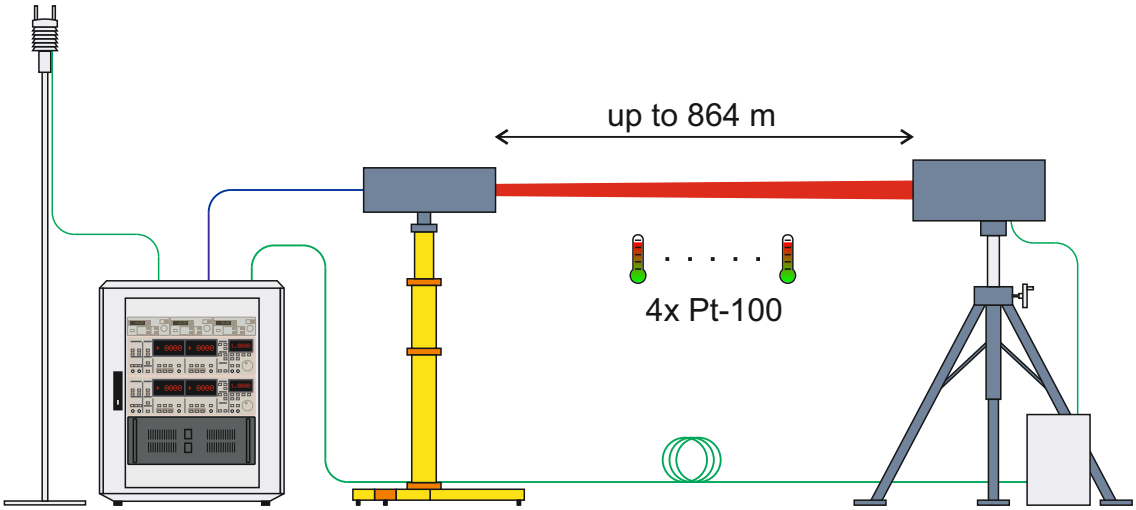

Figure 5: Schematic illustration of the experimental setup used in field measurements. Green wires indicate electrical cables and the blue wire optical fiber.

3.1 Optics

Detailed schematics of the built optics are presented in Figure 6. The laser beam was generated using a distributed feedback (DFB) laser (Toptica #LD-0770-0020-DFB-1). The laser has a nominal lasing wavelength of 770.1 nm that can be tuned within range from 769.1 nm to 771.2 nm by adjusting the laser current and temperature. The laser has a maximum optical output power of 15 mW, of which approximately 3.5 mW was used with 25 mA drive current. The TO-9 packed laser diode was mounted in a thermoelectric cooler (Eagleyard EYP-MNT-0000-0000-0000-CRM14-0001) that was used for temperature stabilisation and as a mechanical mount. The DFB laser was collimated by a coated aspheric lens (Thorlabs A230TM-B) which had a focal length of 4.51 mm. The resulting beam was roughly 2 by 6 mm in size, which is

more than the aperture size of the following optical components. In order to avoid excessive clipping, the beam was shaped to 2 by 4 mm in size using a pair of coated cylindrical lenses (Thorlabs LK13632-B, f = -7.7 mm and LJ1638L1-B, f = 22.2 mm) in telescope configuration. The plano-convex lens was mounted in normal direction and the plano-concave in reverse direction in order to reduce spherical aberration. The focal lengths of the lens pair were chosen as close to -3.93 ratio as possible for the same reason [50]. The laser diode and the lenses were mounted on a 30 mm Thorlabs cage system, which in return was mounted to a 60 mm cage system along with an optical isolator, a $\lambda/2$ plate and an electro-optic modulator (EOM). This configuration allowed an easy removal of the laser collimation package if, for example, changing the lenses were necessary.

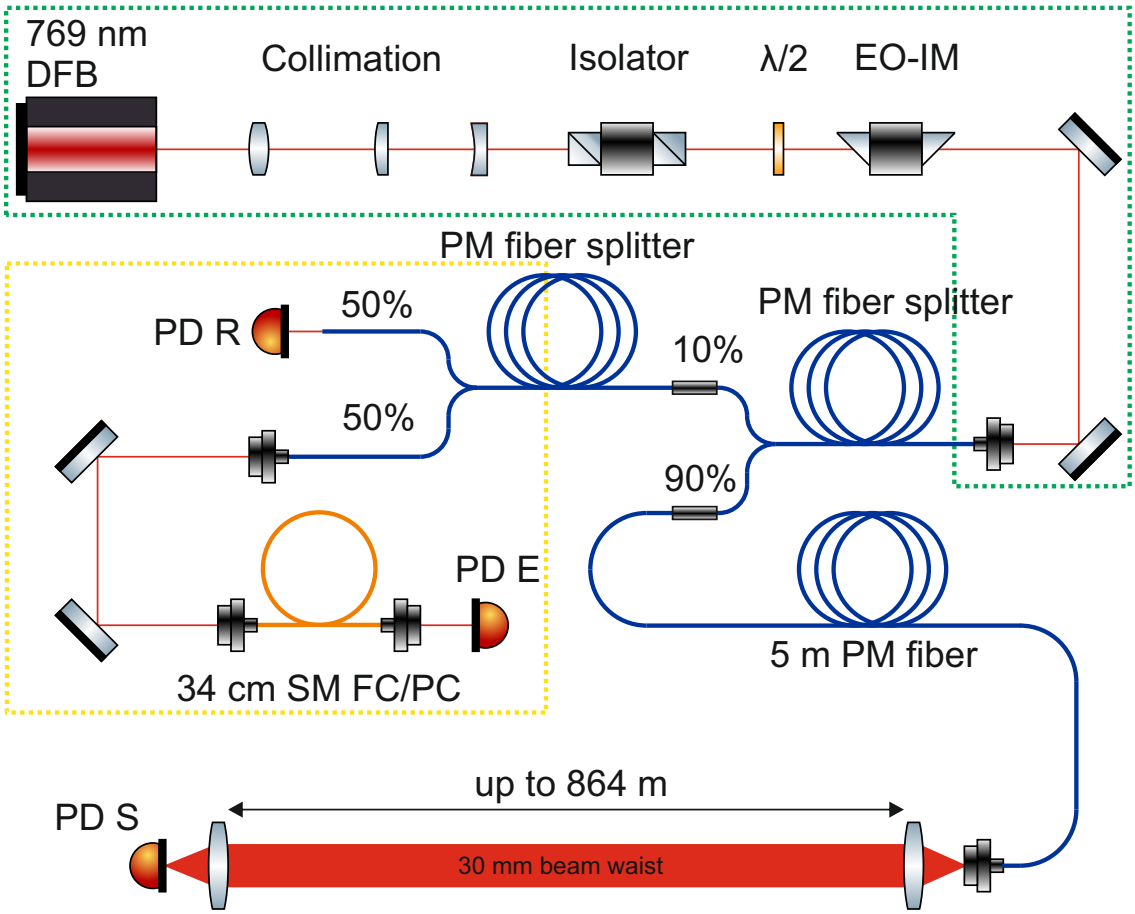

Figure 6: Schematic of the optics used in the experimental setup. PD R stands for reference photo diode, PD E for etalon photo diode and PD S for signal photo diode. PM stands for polarization maintaining and SM FC/PC for single mode fiber with FC/PC type connectors. The dashed lines separate the components that were mounted on different optical breadboards.

The optical isolator used is one of the wavelength tunable LINOS SV/SI series with 5 mm aperture and better than 30 dB isolation. The isolation specification

was confirmed by guiding the laser backwards through the isolator and adjusting the transmission to its minimum. The EOM used is a Conoptics Model 370. The modulator broke down during the beginning of field measurements, for somewhat unknown reasons, but was quickly replaced with similar Model 370 modulator.

The electro-optic modulation frequency was set to 10 kHz and the modulation voltages so that the resultant intensity modulation was $\sin^2(I)$ in shape and close to zero in its minimum. The $\lambda/2$ plate was used for polarization matching of the incident light to the EOM modulation axis. The high frequency modulation was used for lock-in detection of the optical signals. The wavelength modulation for scanning the absorption feature was performed by sweeping the current of the laser diode with a triangular waveform, the frequency of which was 0.5 Hz. One reason for the slow wavelength modulation was that the laser system was not able to follow any faster changes. This could be seen as irregularities in the measured absorption feature.

After passing the EOM, the laser light was coupled to a polarization maintaining 90:10 fiber splitter (Thorlabs PMC780-90B-APC) using two dielectric mirrors and a fixed fiber coupler (Thorlabs F240APC-780). The 10 % output of the splitter was then again split into two using a similar fiber splitter, but with 50:50 ratio (Thorlabs PMC780-50B-APC). The 90 % fiber output was used for measurement beam and the two weaker but equal 5 % outputs for reference detection and frequency measurement. The reference detection was necessary for intensity normalization of the absorption signal. Out of the initial 3.5 mW of optical power, 0.4 mW was coupled to the fiber. The free space optics caused losses of about 3 dB and the rest was lost in the fiber coupling most likely due to bad beam shape. The achieved power levels were sufficient for the measurements and actually beneficial, since, together with the large diameter of the measurement beam, the laser light then posed no risk to eye safety.

As long term stability was a crucial factor in the experiment, we focused most of the efforts trying to improve it. Invar rods were used in the cage system together with plenty of temperature stabilisation inside the rack cabinet as described in the next subsection. Although the cage system was well built and easy to adjust, it often caused severe optical feedback and etalon effects as all the components were strictly in line. When the reference detection was performed with sample rate of over 100 samples per second it mostly solved these problems, since the detection was then fast enough to fully normalize the signal baseline. However, the cylindrical lenses mounted before the isolator introduced some optical feedback to the laser diode. As a result, the frequency sweeps became non-linear.

Accurate knowledge of the frequency axis is often crucial in spectroscopy. Because of the optical feedback, the relative frequency of the laser could not be determined accurately solely by the drive current. For this reason, a fiber etalon was used to measure the frequency tuning rate. The etalon was formed by splicing a standard Thorlabs P1-780A-FC patch cable with FC/PC connectors to a length of 34 cm and coupled the laser from free-space into the fiber. Because of limited space, the etalon setup had to move on to a separate optical breadboard. Thus, the fiber coupled light had to be collimated with fixed fiber collimator (Thorlabs F220APC-780), adjusted with two gold plated mirrors and coupled again into the etalon fiber with a fixed collimator package (Thorlabs F220FC-780) as shown in Figure 6. The straight ends

of the FC/PC connectors of the etalon fiber with approximately 4 % reflectivity was enough to have a good visibility of the etalon effect as shown in Figure 7.

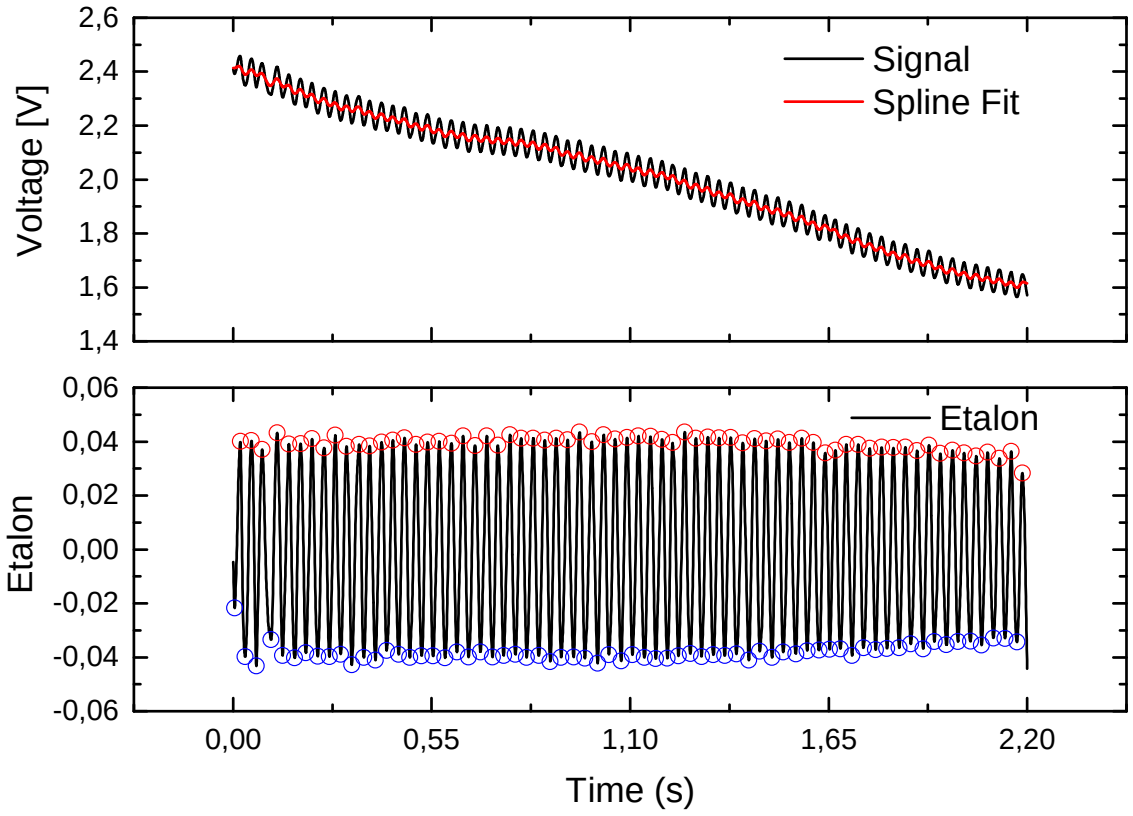

Figure 7: Measured etalon signal. Intensity dependent part has been removed from the lower graph for clarity. Upper graph shows the unprocessed signal and a smooth spline fit that was removed from the raw signal before peak detection. The tolerances for the spline fitting were chosen so that signal was most easily detectable for the peak detection. Red and blue dots are the detected peaks and valleys, respectively. The data is from the same absorption measurement as in Figures 13 and 14.

In order to use the etalon signal as a frequency discriminator, the free spectral range (FSR) of the etalon must be known. FSR can be calculated by

$$FSR = \frac{c}{2\,n\,l}, \tag{19}$$

where l is the length of the etalon. For the refractive index of fiber $n = 1.45$ and length $l = 0.34$ m the FSR is $\sim$ 300 MHz. The value used for the FSR in the measurements was 295.97 MHz, which is a refined approximation from the theoretical value based on the known absorption line width. From Figure 7 the length of the frequency sweep can be calculated to be 20.1 GHz or 0.67 cm^{-1}.

FSR is an excellent parameter for a relative frequency reference as it is almost insensitive to temperature variations. Although the length and the refractive index of the fiber change as a function of temperature, the relative change is of the order

of 10^{-6} that is well below the requirements. A more severe problem is the sensitivity of the resonance frequencies to temperature. As a reference, a solid etalon made of fused silica has a resonance frequency tuning rate of ~ 2.5 GHz/℃. It turned out that even a slightest air flow would distort the etalon signal, because the locations of the resonance peaks would then vary during the relatively slow laser wavelength tuning. To avoid this, the fiber was wrapped in thick thermal insulation.

The beam divergence on the intended 1 km measuring distance required extra attention when designing the transmission and receiving ends of the measurement beam. Using the far field approximation, Equation 20 can be used to describe the basic rules of divergence: a larger beam and a shorter wavelength diverges less.

$$\theta = \frac{\lambda}{\pi w_0} \tag{20}$$

$$w_s = \frac{f\lambda}{\pi w_0} \tag{21}$$

In the Equation 20 w_0 is the $1/e^2$ beam radius, usually referred as beam waist. When a Gaussian beam is focused by a lens with focal length f, the resultant spot radius is given by Equation 21 [5].

In the field measurement setup, the light was guided to the transmission head through a 5 meter long polarization maintaining fiber (Thorlabs P3-780PM-FC-5) that has a mode field diameter of 4.9 μm at 780 nm. The positioning of the fiber end was fine tuned with a Thorlabs NanoMax-TS XYZ-translator system. The light was then collimated with a high quality anti-reflection coated aspheric lens (A100-200LPX-DL-B) from Asphericon with a focal length of 200 mm and a diameter of 100 mm. According to the theoretical calculations and in ideal case, the initial beam would be 4 cm in diameter and after travelling 864 m 6 cm in diameter. At the receiving end, the light was focused to a 1 cm^2 silicon diode with an uncoated condenser lens (item #27-513 from Edmund optics) that had an 400 mm effective focal length and a diameter of 200 mm. The resultant beam size, according to Equation 21, would then be 7 μm. An exact confirmation to the beam diameter values is not available as the beam was not visible during daylight even with an infrared camera. During night time the camera was helpful and it was possible to see the beam size on the diode and before the condenser lens. When measuring over 864 m OPL, it was observed that the beam size on the diode was approximately 0.5 cm. The receiving diode was intentionally placed in front of the focal point so that the spot size would be larger. This was considered to minimize the effect of any spatial differences that diode might have in its response. On the condenser lens the beam diameter was quite close to 30 cm. In addition, the beam experienced heavy aberrations, which lets us assume that the fiber end in the Tx end was somewhat off the focal point of the aspheric lens in lateral direction. This, together with the saturation effect of the camera, would also explain the significantly larger beam waist.

3.2 Electronic hardware

All the sensitive optics, electronics and instruments were built inside a 18 unit rack cabinet that was in coarse temperature control by a thermostat heater and a manually operated outlet fan. The temperature inside the rack cabinet was monitored using four LM35 sensors from Analog Devices, which indicated that while the outdoor ambient air varied from 5 to 15 ℃, inside the air temperature stayed between 20 and 24 ℃ as shown in Figure 8. During a warm day the insides of the rack heated up because the ventilation was not powerful enough. On the other hand, during chilly nights the temperature dropped and the heater turned on, which can be seen by the sharp peaks in the inside temperatures. The peaks occurred either because the heater control had hysteresis or too much thermal delay. Either way, a better regulation could have been quite easily achieved by adding more powerful outlet fans, automatically controlled by the measurement computer so that they could have been turned off during cold weather and let the instruments heat the cabinet instead of the heater.

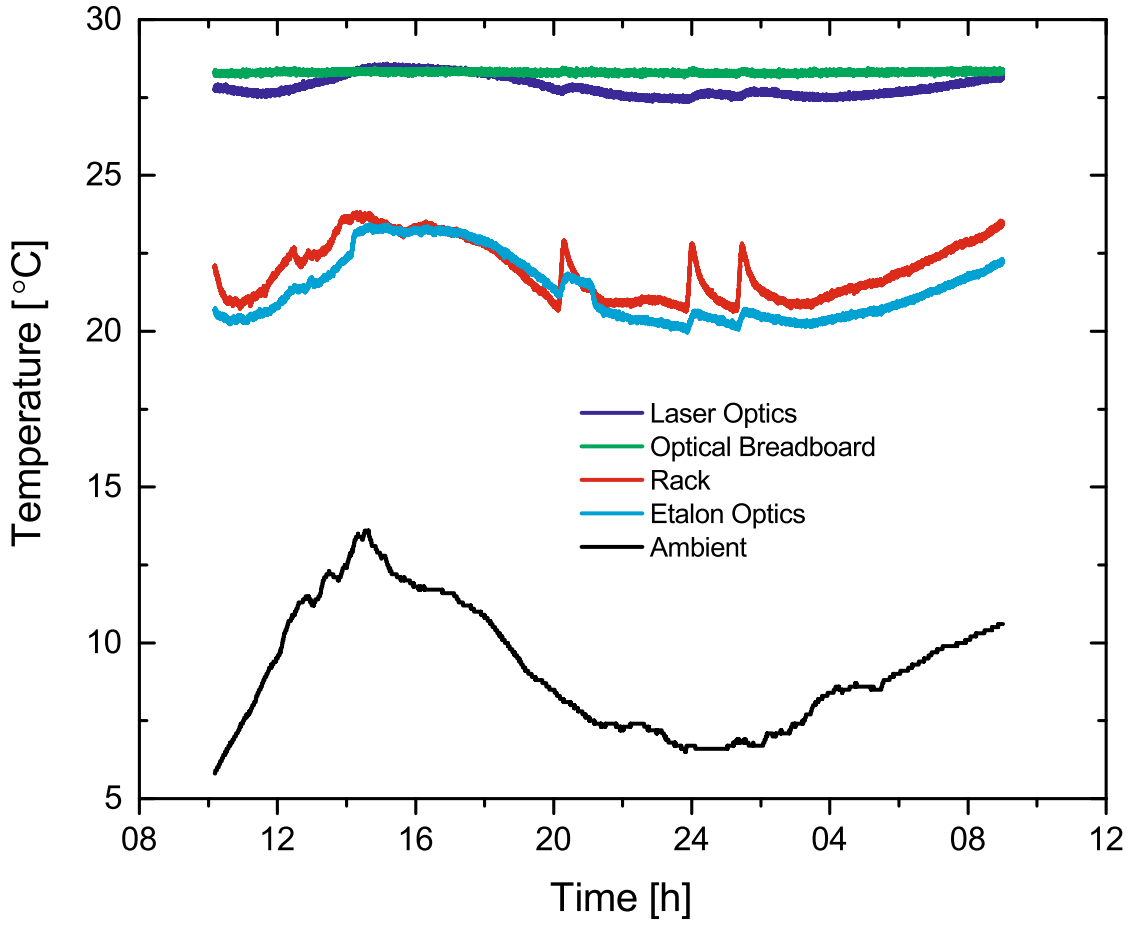

Figure 8: Recordings of temperatures inside and outside the rack cabinet on 29.9.2015.

The primary optics, encircled by the green dashed line in Figure 6, were mounted

on an optical breadboard, the temperature of which was regulated to ∼28.3 ℃ using a resistive heater, a 100k NTC thermistor and a PTC5000 controller from Wavelength Electronics. In addition, the optics were thermally insulated, which helped their temperature to stay within 1 ℃. The 'Laser Optics' curve of Figure 8, is the ambient air inside the insulation and 'Opical Breadboard' the regulated breadboard temperature. The graphs show that although the breadboard was well regulated, the insulation was not good enough to keep the optics in the same temperature. The secondary etalon optics, encircled by the yellow dashed line in Figure 6, were also mounted on an optical breadboard and lightly insulated but not regulated. Their temperature follows quite closely the temperature of the rack but more importantly, the double insulation of the etalon fiber helped significantly to improve its signal quality.

Other equipment in the rack cabinet included two Stanford Research SR830 lock-in amplifiers for signal and reference detection, Thorlabs drivers for the laser and TEC elements, signal generator for the EOM driver and a measurement computer with National Instruments PCI-6251 data acquisition card (DAQ) and LabVIEW software. Instead of using GPIB communication to read the data from the lock-in amplifiers, the X- and Y analog outputs were read directly with the DAQ card. In this way the sampling frequency of the lock-in signal could be increased, since the SR830 amplifiers have an update rate of only 512 Hz in the calculation of the R parameter, whereas the X and Y analogue outputs are updated with 100 kHz. In addition, it was possible to avoid using any external trigger signals in the data synchronization as the reading of etalon and measurement signal together with the laser current sweep could be performed on a single DAQ card.

Most of the setup development took place in a laboratory at MIKES. The laboratory facilities feature a temperature controlled 30 m long track, on which the beam was reflected back and forth with a high quality 4" metallic mirror from Altechna. For several reasons, the system could not be reliably calibrated indoors and the task was left for field measurements at Nummela. Difficulties were caused by the short absorption length of roughly 67 m, which is much less than the transition line selection was intended for. In addition, only minor 1 ℃ temperature changes were possible as otherwise the other instruments in the room might have suffered. To monitor the laboratory temperature along the absorption path, five Pt-100 sensors were placed over the path and a multiplexing digital multimeter (DMM) was used to measure their resistances. The DMM was read to the computer using GPIB.

In the field measurements, four MadgTech RTDTemp101A data loggers with stainless steel Pt-100 sensors, which were 15 cm long and 3 mm in diameter, were used to monitor ambient temperature along the optical path. The manufacturer promises that loggers have a calibrated accuracy of ±0.05 ℃, which was verified with comparison measurement in a water bath at MIKES. Additionally, the measurements required weather information about the pressure and relative humidity along the optical path. To perform these meteorological observations a Vaisala WXT 520, placed at the Tx end, was chosen as a main weather station and a Madgtech PRHTemp101A logger, placed at the RX end, as an additional information provider. Vaisala gives following accuracy specification for the WXT, which fulfil the pressure

and humidity requirements in Table 2: temperature ±0.3 °C, pressure ±0.5 hPa and relative humidity ±5 %. The accuracy specifications for the PRHTemp101A logger are not nearly as good in the case of pressure and humidity, therefore it was mainly used for temperature readings although it proved to fulfil its specification in comparison measurements at MIKES.

3.3 Software

National Instruments LabView was chosen for the programming environment as it allows effortless integration with measuring instruments and an earlier version of the software was already implemented on it. An active measurement, such as thermometry, often benefits from real time results. Although the implemented measurement software outputted preliminary temperature results that were used to monitor and adjust the measurement, its main purpose was to record high quality data for post processing. Figure 9 explains how the preliminary results and data recording were realized in the program.

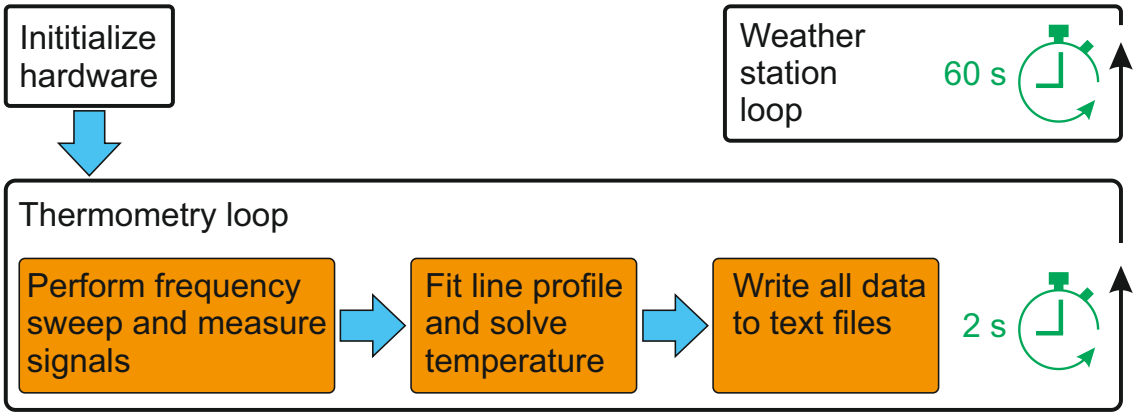

Figure 9: Functional realization of the LabView measurement program. After start up initialization the two loops start to run parallel with different repetition rates. The loop time of the thermometry loop is mainly determined by the speed of the frequency sweep.

At first, the program initialized the lock-in amplifiers and the PCI DAQ card to correct settings. The lock-in amplifier, used for reference detection, was set to single-ended input mode and the one for absorption signal to differential AC mode. The differential mode was highly beneficial because of the 900 m long cable, which was used for signal transmission from the receiving end to the transmission end, had then minimal effect on the signal quality. The increased voltage noise of a long transmission path was then only seen as an offset that was corrected programmatically by using auto-offset function on the SR830 when the laser source was turned off. This way the offset corrections were 0.00 % for the reference channel and 2.45 % for the signal channel. The offsets are expressed in percentage of the analogue output full scale that is ±10 V. In addition, a manual offset correction was used by adding

a constant value to the DAQ voltage measurement of the signal channel. The added value was -50mV for 432 m data and 30 mV for 864 m. The values were evaluated by examining the slope of the absorption profile baseline that was caused by offset. The change in the offset settings is logical as it was caused by the voltage noise which is likely to change as the cable was unwound from length of 432 m to 864 m. The time constants of the SR830's were set to 1 ms, filter slope to 18 dB/oct and channel sensitivities to 50 mV/nA. The phase settings were set using the auto-phase function of the lock-in amplifiers in the beginning of the measurement campaign and was then kept constant. All the setting for the lock-in amplifiers were held constant during measurements. The applied DAQ settings included sample rate and synchronization of the channels. We used 25 kHz sample rate which was down sampled by averaging blocks of data.

After the hardware initialization at program start up, the program runs a measurement routine and a WXT read routine in parallel loops. The measurement routine begins by creating frequency sweeps. Next, the sweep is performed while the analogue inputs of the DAQ card are simultaneously read to memory. The following steps are adjusting the centre frequency by tuning the laser temperature with TEC controller, calculating frequency axis from the etalon data, fitting Voigt profile to absorption data, solving for temperature and measuring rack temperatures. Writing data to text files and updating graphs is performed between each iteration of the main measurement loop.

The TEC tuning was implemented after the line centre was noted to experience some drifting. The actual line centre has a pressure-induced shift of -0.00273 MHz/Pa [43]. By noting that normal pressure variations are 100 hPa at maximum and the line half width is in the order of 1 GHz, the pressure shift can not account for the observed drift. Possible reasons are then drifting of the temperature and laser controller. A slight drawback from the TEC tuning was that it was based on the measured line centre. Thus, if the absorption line was lost for an extended period, for example because of heavy rain or condensing of the lenses, the control loop would most like drift to an extreme and its recovery would be slow. This behaviour was not an issue though.

Although not precise, the real-time data available was fundamental for successful measurements. We monitored most of the parameters included in the setup and with long-standing experience on the setup, various fine tunings could be performed along the measuring session. Key parameters included the absorption profile, residual of the fitting, temperature solution, etalon signal and rack temperatures. For example if the measurement beam would drift to the edges of the focusing receiver lens, it was immediately seen as increased noise on the absorption profile. Then it was possible to fine tune the XYZ-translator only by inspecting the profile.

4 Field measurements

The field measurements of this thesis were mainly carried out at the Nummela standard baseline in Vihti, Finland at the end of September 2015. Some early test were also carried out at the courtyard of MIKES some weeks before Nummela. The purpose of these tests were primarily to learn how the instruments would tolerate transporting, how well the rack unit would regulate its temperature and how difficult it would be to align the measurement beam in field conditions. Although no presentable data was recorded in these tests, they were vital for an efficient campaign in Nummela.

The Nummela standard baseline, managed by the Finnish Geospatial Research Institute (FGI), has become noteworthy on international scale for its stability [51]. The baseline is built on an esker and is surrounded closely by forest as seen in Figure 10b.

(a) 0 m observation pillar

(b) 24 m observation pillar

Figure 10: Photos from the Nummela standard baseline. In Figure 10a is the shelter of the first observation pillars under which the transmitting end equipment was located. In Figure 10b is a picture from the same place but in the direction of the baseline. Foremost is the 24 m observation pillar and its shelter. All the pillars further away were similar to this one and surrounded by fence starting from 216 m.

The esker is also a popular outdoor recreation area and encounters with locals were not avoided. Outsiders have free access to most of the baseline, which allows them to intentionally or unintentionally interfere with the measurements on the baseline. Fortunately, all the observation pillars and buildings are sheltered by locked fences and roofs as shown in Figure 10. During the nine days the instruments stood on the spot, we conducted test runs on the closer 72 m and 216 m observation pillars and actual measurements on the furthest 432 m and 864 m observation pillars. The seemingly arbitrary distances are multiples of 24 m long invar wire that the FGI has been calibrating at the Nummela baseline since its establishment in 1933 [51].

Outline of the Nummela standard baseline is depicted in Figure 11.

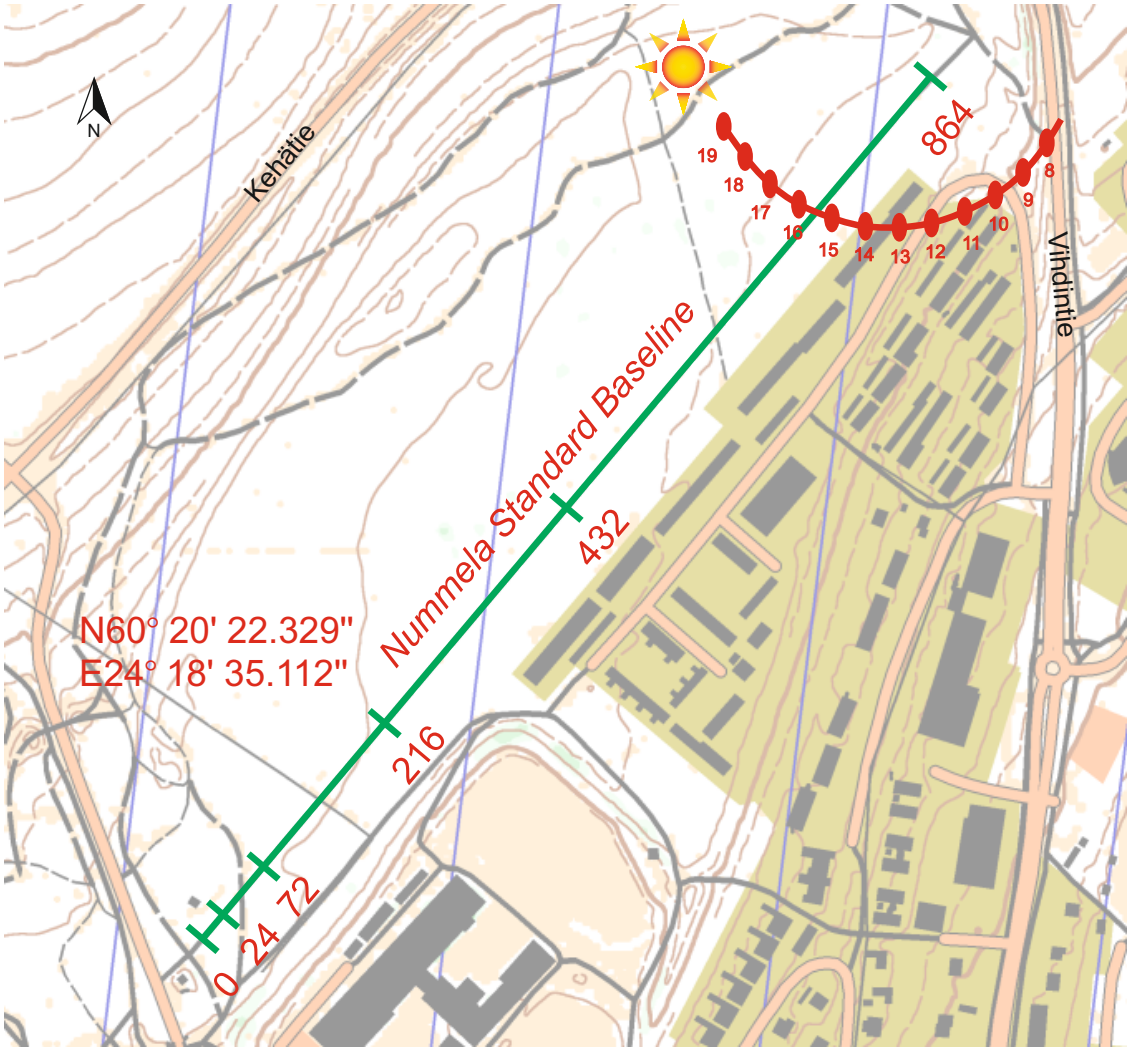

Figure 11: Outline of the Nummela standard baseline, including coordinates of the zero observation pillar, nominal distance marks for the other pillars and suns position with respect to time of day on 29.9.2015. The map is drawn to scale. All equipment except the Rx head and the temperature loggers were positioned under the shelter of the zero observation pillars.

The transmission end, including the rack unit, the transmission head and a computer desk, were positioned outdoors under the shelter of the first observation pillars in Figure 10a. The transmission head was aligned parallel with the optical path that is used by optical length measuring instruments. Transverse separation between the beams was below 30 cm along the whole measurement length. The primary weather station, Vaisala WXT 520, was positioned right next to the shelter, about 2 meters in height and 1.5 m away from the edge of the roof. Positioning of the weather station was limited by the USB-cable length, which the station used to connect to the computer.

The remote end, including receiver head, battery operated PRHTemp logger and analogue electronics for signal detection, was moved step by step from the closest pillar to the next as the measurements progressed. Information from receiving end to transmission end was carried as differential analogue voltage signal by standard CAT 6 Ethernet cable. Between the Tx and Rx ends, 3 to 4 battery operated resistance temperature detector (RTD) loggers using Pt-100 sensors were placed to monitor the ambient air. The loggers were positioned roughly equally along the measurement path and horizontally within 2 meters of the laser beam. They were hanged on poles at a height of 1.5 m and sheltered by small platforms lined with aluminium foil so that the sensors were not exposed to direct sunlight. During the final days of the campaign the positioning of the sensors had to be relaxed as one of the loggers was stolen during a night and losing any more was not hoped-for. The stolen logger was not located behind the fences since a more equal spacing of the loggers was desired than the protected areas provided.

The original plan was to perform simultaneous measurements with a group of length metrologists from PTB, Germany. Unfortunately, the time schedules did not match as well as planned and the breakdown of the EOM made the one recorded dataset unreliable. However, even better method to validate and evaluate the temperature measurements was offered by the FGI. The FGI let us use one of their most reliable tacheometers, a commercial EDM for most precise radial length surveying. The specific model was TC2003 n:o 439351 for which the reading resolution is in the order of 10^{-7}. At this scale, the environmental variations affecting the refractive index of air are easily seen in the measured distance. So, by using the tacheometer to measure the same path as the optical temperature measurement and recording the tacheometer readings with a constant and known refractive index, the experimental temperature measurements together with the pressure and humidity readings of the weather station can be used to correct the length measurand. The fundamental reference for the accuracy of the temperature measurements would then be the distance between the observation pillars on the baseline which undoubtedly is constant.

A usual measurement day started by downloading data from the previous evening. In practise, the loggers had to be collected and the data downloaded from the loggers and the computer. The data were always analysed on separate, more powerful, computers. After collecting the data, the optics were refined if necessary and moved to the next observation pillar if the results on the current distance were sufficient. For example, quite often the lenses of the Tx and Rx heads were wet out of condensation

and the alignment of the measurement beam needed fine tuning. The problem with the alignment was not most likely mechanical but optical caused by refractive index gradients of the air. This could be seen especially well with the telescopic sight of the tacheometer. The alignment of the tacheometer always drifted to the same direction as the measurement beam, and quivering of the air was clearly visible through the sight of the tacheometer. These slight alignment difficulties could have been solved by the closed loop piezo controller that was only tested in the laboratory. After the measurement was running again, the setup was let to measure overnight or if the plan was to use the tacheometer that day its readings would be recorded manually every ten minutes, since there where no automated routine readily available for data logging.

The goal of the measurement campaign was to collect all possible data and use the following weeks to analyse it in-depth. Four good dataset were recorded from four successive days from distances of 432 m and 864 m. In order to give an general impression of the measurement conditions, Figure 12 displays observations of a weather station in Nuuksio, Espoo. The weather station at Nuuksio is located some 15 km South-East from the baseline and managed by the Finnish Meteorological Institute[4] (FMI) which kindly provided the data for us. Rainfall is not plotted since there was only a short one hour burst of rain at 15 o'clock on 1.10.2015. Although the absorption profile was still visible during rain, a low uncertainty profile fitting with the current setup was impossible due to heavy interference of the rain. The effect of the interferences will be further discussed in Subsection 5.

The collected data and its recording intervals are summarised in Table 4.

Table 4: The table summarises the recorded data and their measurement intervals.

Parameter group	Measurement interval	No. of samples per measurement
Voigt Parameters	2 s	1
Vaisala Weather Station	60 s	1
Tacheometer	10 min	5
MadgeTech loggers	15 s	1
Rack temperatures	2 s	1
Raw etalon signal	2 s	4000
Etalon peaks and valleys	2 s	200
Absorption profile	2 s	1000
Voigt profile	2 s	1000
Frequency axis	2 s	1000
Raw absorption signal	2 s	1000
Raw reference signal	2 s	1000

[4]Further information on FMI available from their website: http://ilmatieteenlaitos.fi/mennyt-saa-ja-ilmastotilastot

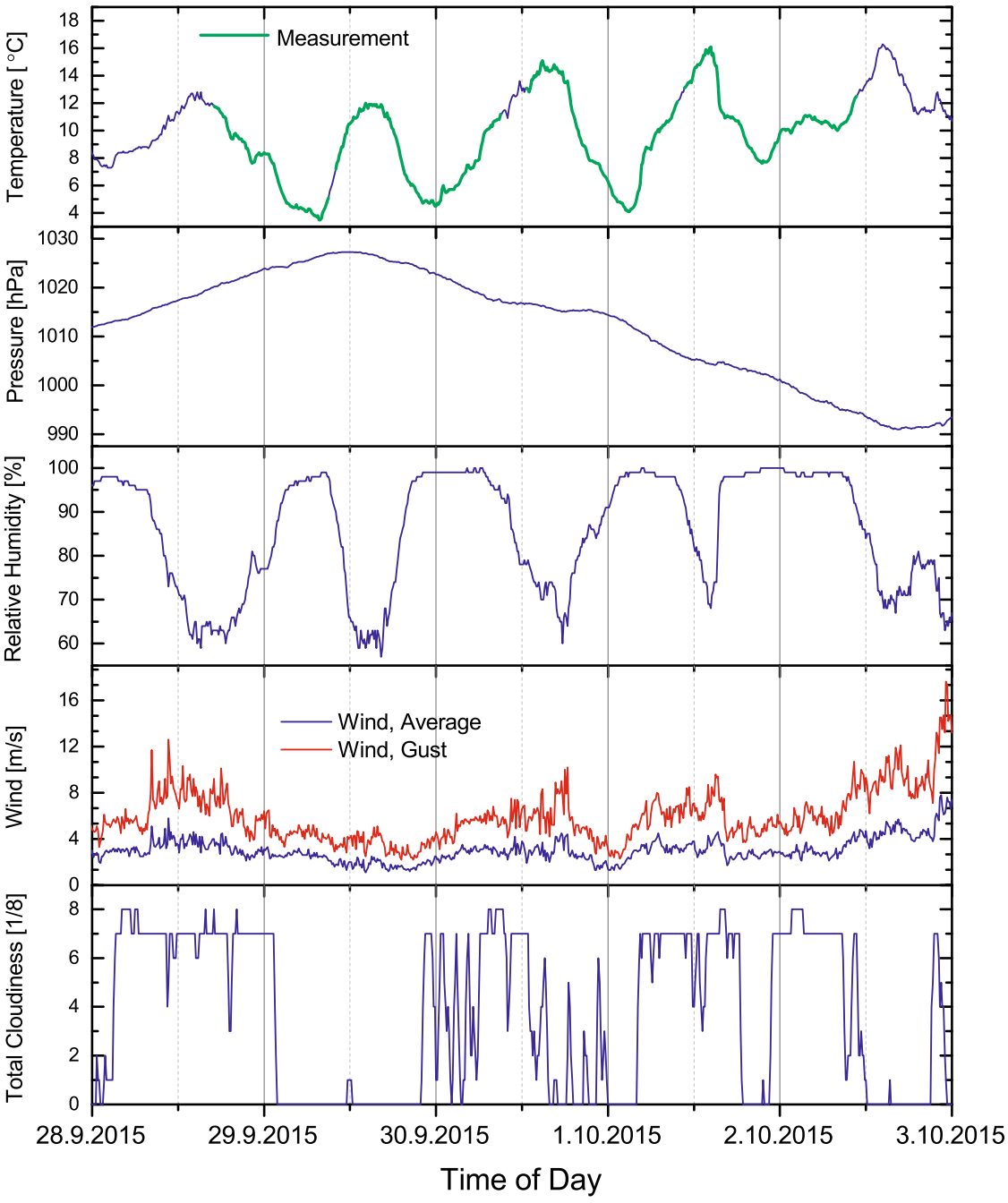

Figure 12: Weather data from FMI's weather station in Nuuksio, Espoo, located some 15 km South-East from the baseline. The green parts of the temperature graph highlight the time intervals of the measurements.

5 Data analysis

During the field measurements the LabView routine recorded all data that were necessary to determine the temperature starting from the raw DAQ signals. The data were then analysed and processed with Matlab using methods described in this section. Practically, the analyses included all the same steps as in the real-time LabView program. However, unlike with LabView, it was possible add more features to the routine and conduct more detailed step-by-step analysis of the sensitive parameters.

This section is organized in the same order as the analysis process. First, the frequency axis was determined and a line-profile fitted to recorded absorption feature in order to obtain the line area along with other parameters. Next, because the fitting procedure was found to result in false line parameters in case of noisy signal, an outlier removing algorithm was used to process the line area results. Secondly, the fundamental constants describing the spectral line intensity were deduced by referencing the spectroscopic data to a theoretical model given in Section 2. Thirdly, the final temperature results were solved according to Equation 17 and appropriate corrections to the tacheometer measurements are given.

5.1 Line area

Although the real-time implementation of the non-linear frequency sweep characterisation was successful, the analysis was performed again in order to examine its sensitivity to certain parameters. The processing of the etalon data began by removing the laser intensity dependent part from the data. The result was then run through an interpolating peak and valley detection that gave the number N and the locations of the maxima and minima as illustrated in Figure 7. The difference in frequency of each half wave would be FSR/2, so a vector [FSR/2 2·FSR/2 3·FSR/2 ... N·FSR/2] would give the relative frequency of the sweep. A spline curve was then fitted to this measured frequency data in order to smooth out any noise related inaccuracies. Since wave number is more practical unit in spectroscopy than frequency, the fitted data were converted into wave numbers and interpolated on a linear scale so that the frequency was defined at the same points in time as the absorption data.

The characterisation of the frequency sweep was performed for each sweep individually. Figure 13 presents an example of the non-linearity of the frequency sweep, the form of which could vary drastically between sweeps. Smoothing the frequency data was not clearly beneficial. For some sweeps it gave better results and other worse, therefore a moderate smoothing was applied as seen in Figure 13 to remove much of the noise.

The greatest challenge in making high accuracy and low uncertainty thermometry was fitting a line-profile to the measurement data. On a fundamental level the difficulty lies in accurate description of the line-profile with a function. In practise however, these subtle details are often hidden by system noise, as was the case with the measurements in this thesis. During daytime the air was filled with flying insects and falling debris that would interfere with the beam. Naturally, the problem got worse as the measurement was moved to further observation pillars. Interestingly,

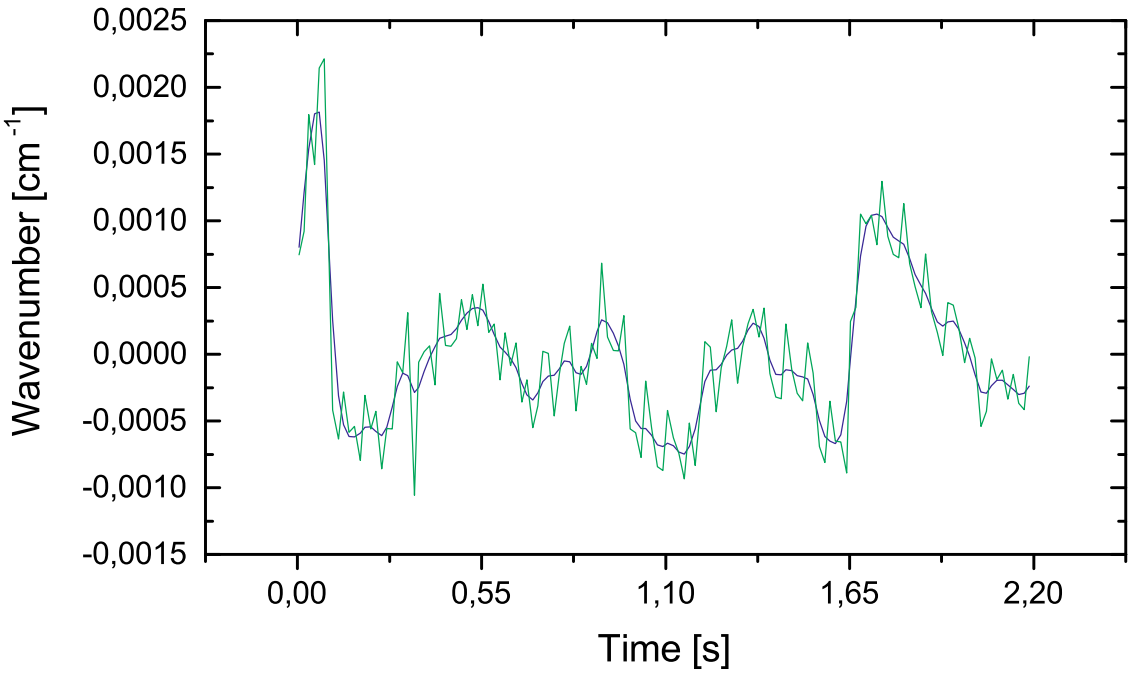

Figure 13: An example of the nonlinearity of the frequency sweep. The data is from the same absorption measurement as in Figures 7 and 14. The curves present the direct frequency measurement and a smoother spline fitting. Linear part has been removed from both curves for clarity. The total length of the sweep is 0.66 cm^{-1}.

far less disturbances were observed during night time, which could be explained by less active insects and stiller air. Figures 14, 15 and 16 present examples of excellent, slightly disturbed and heavily disturbed absorption signals. Although the beam was only visible in darkness, night time still was not a preferable measurements time for practical reasons.

In order to minimise the effect of the disturbances we used a robust non-linear least-squares fitting method with bisquare weighting from Matlab Curve Fitting Toolbox[5]. The bisquare method gives a weight for each data point based on how far the point is from the fitted line and then minimises the weighted sum of squares. Points far from the line, which are in this case mostly due to disturbances, get reduced weight and points near the line get full weight. If a point lies farther from the line what would be expected by random chance it gets zero weight. The robust method uses an iteratively re-weighted least-squares algorithm that re-evaluates the weightings each round until certain tolerance in convergence or iteration limit is reached. An even more elaborate method would have been to assume a direction for all the interferences, as they always occur in the same direction due to the decreased transmittance the debris cause. However this would have required some extensive Matlab coding, which was out of the scope of this thesis. The non-linear

[5]Online documentation available: http://se.mathworks.com/help/curvefit/least-squares-fitting.html?refresh=true#bq_5kr9-4

line-profile equations were written as described in Section 2.2 with an added first order polynomial to account for the offset and slope of the baseline. The fitted parameters are listed in Table 5.

Table 5: The fitted line parameters, discussed in Section 2, and their units. Parameters which are not listed here were fixed.

Parameter	Symbol	Unit
Line area	A	cm^{-1}
Lorentzian width	γ_L	cm^{-1}
Centre wave number	ν_0	cm^{-1}
Offset	a_0	-
Slope	a_1	-

The LabView routine used the Voigt profile for fitting as it could be implemented more effortlessly than the Galatry profile and the results were only meant as preliminary. The Matlab routine used the Galatry profile as it provided a better fit and its fitting performed significantly faster than the implemented approximation of the Voigt profile. For a reference, Figures 14 - 16 present a comparison of fitting profiles on absorption features of different quality. Figure 14 has no disturbances and can thus be used to clearly demonstrates that the Galatry profile describes the line-profile very well compared to Voigt and Lorentzian profiles. In Figure 15 something has intersected the beam when the laser frequency was right on top of the feature and on the right tail. In this case, the interferences were well recognized by the robust fitting procedure and the deduced line parameters were acceptable. In Figure 16 the intersections are similar in strength as in Figure 15, but occur on a more critical point of the profile. The robust fitting function was not able to detect the peak on the left side of the profile, which led the routine to a totally incorrect outcome.

The line areas, obtained from the fitting procedure, were then filtered using methods based on the goodness of the Galatry fit and Hampel identifier. The Matlab's curve fitting function, used for the line-profile fitting, outputted two parameters that were suitable for excluding unreliable profile fits: sum of squares due to error (sse) and measure of first-order optimality (fopt). If either of these values exceeded a defined threshold the corresponding measurement was excluded. For example, the disturbed absorption signal in Figure 15 would not result in rejection by these criteria, but the one in Figure 16 would. If for some reason a single measurement point was not identified as an outlier by the goodness of the fit, but was still a clear outlier in statistical sense, a Hampel identifier was used to detect and exclude the outlier. The Hampel identifier calculates a median and a standard deviation of a window composed of the sample and a defined amount of surrounding samples. It then marks the sample point as an outlier if it differs from the median more than a defined threshold. After these exclusion processes, the data experienced noise close to normal distribution accountable for random change. The complete set of

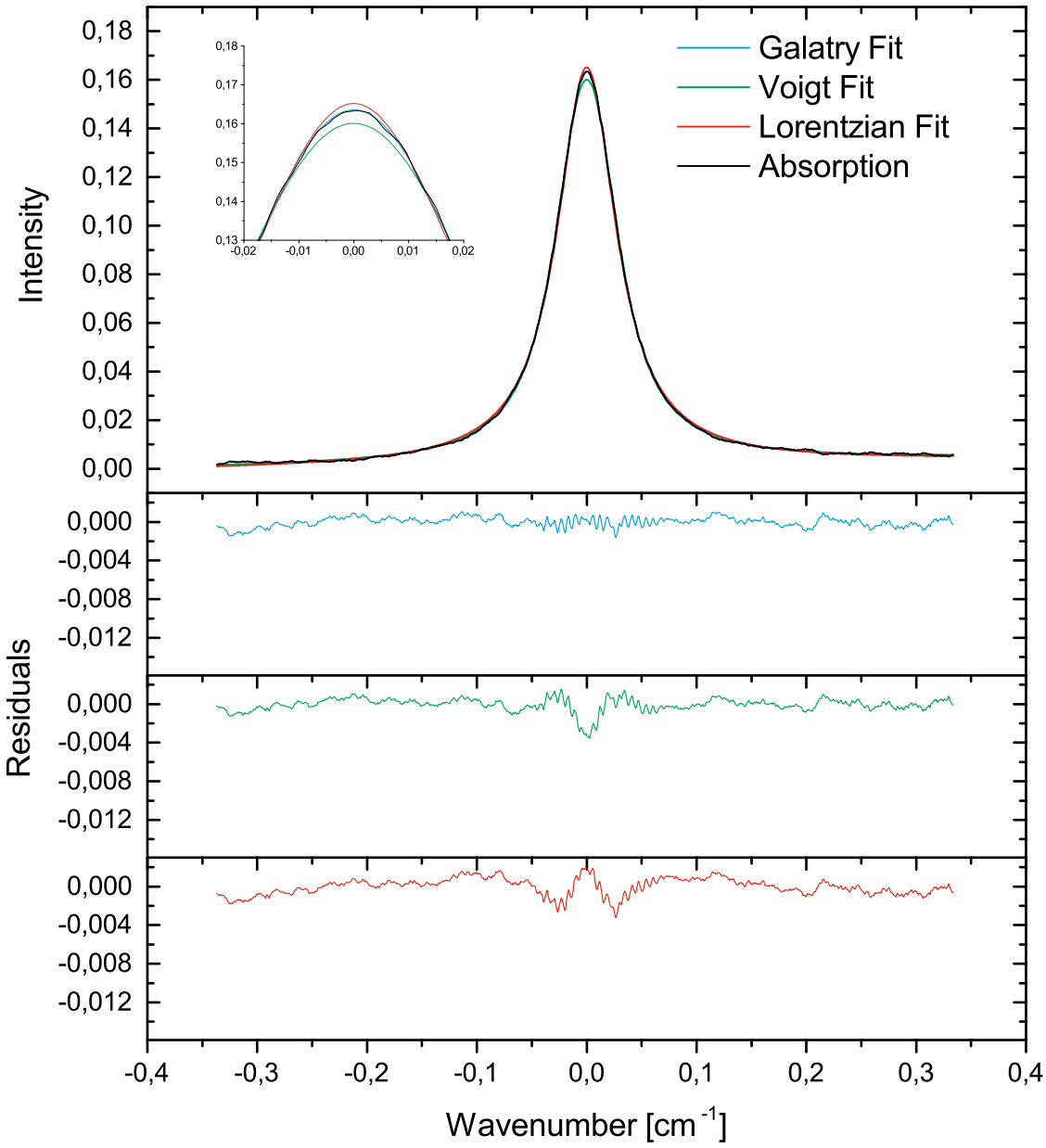

Figure 14: An example of non-interfered absorption measurement. The residuals of different line-profile fits are plotted on the lower figures. The absorption data were recorded at 29.9.2015 11:42:22 at Nummela on 432 meter path length.

outlier removal results is presented in Appendix A. In Figure 17 the results from measurements on 29.9.2015 are presented, which is used as an example throughout this thesis. In the results, black dots indicate the unprocessed data, blue circles the excluded points based on sse criterion, red circles based on the fopt and green circles by the Hampel identifier.

Table 6 lists the used exclusion criteria and the number of excluded points by each criterion. The data from 864 m OPL experiences far more disturbances, which

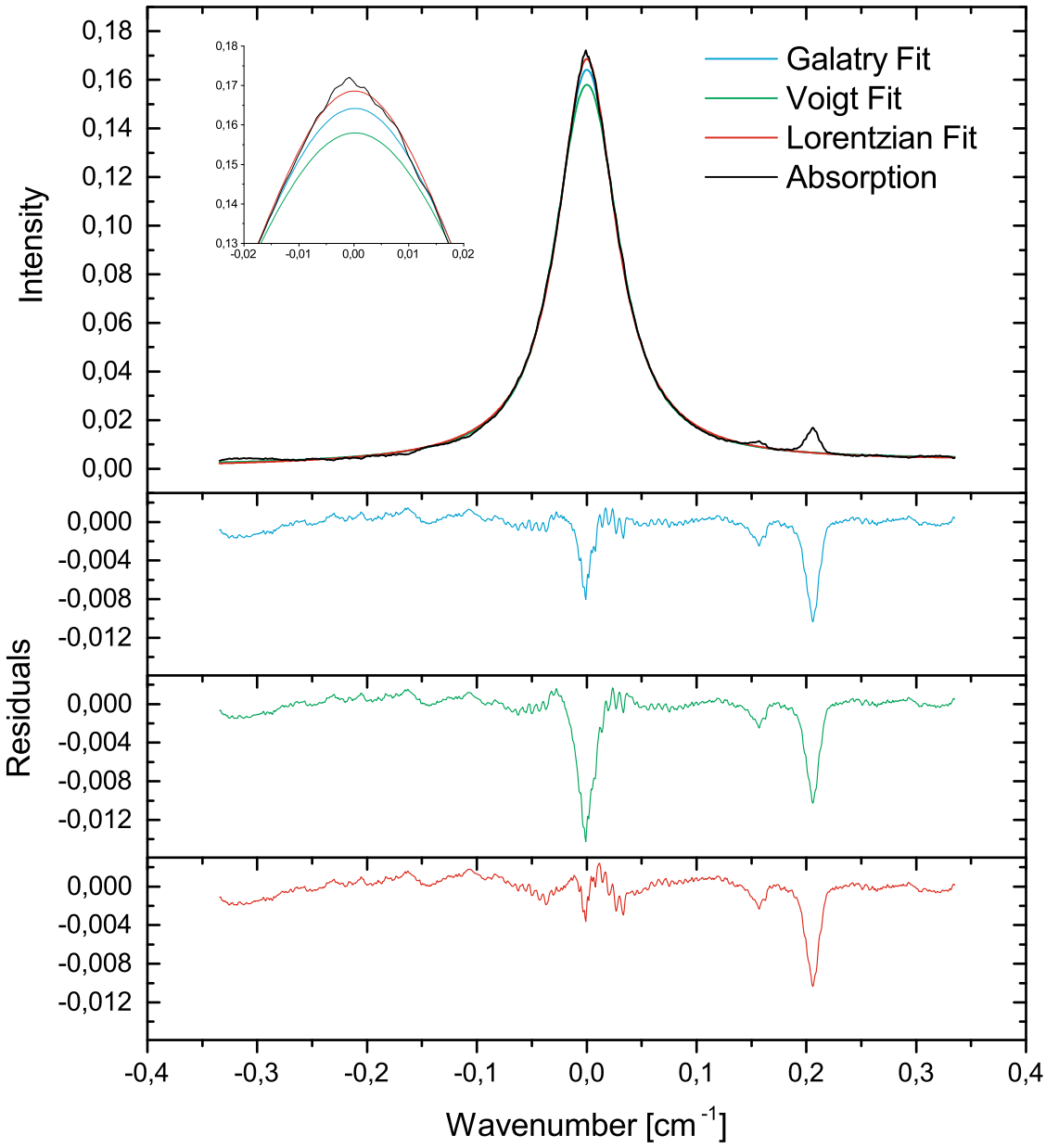

Figure 15: An example of interfered absorption measurement. The residuals of different line-profile fits are plotted on the lower figures. Peaks on the tails of the profile are not as critical as the one right on top of the peak. The fitting function did well on this profile and was not excluded as an outlier. The absorption data were recorded at 29.9.2015 11:24:40 at Nummela on 432 meter path length.

is why the sse threshold had to be relaxed. Otherwise more than 70 % of the data would have been rejected although it was suitable for spectroscopic thermometry. The increased noise on 864 m was quite expected as more beam interruptions are likely to happen, and keeping the alignment to the receiver was more difficult. Short time intervals, such as in Figure 17 where high rates of outliers based on sse criterion

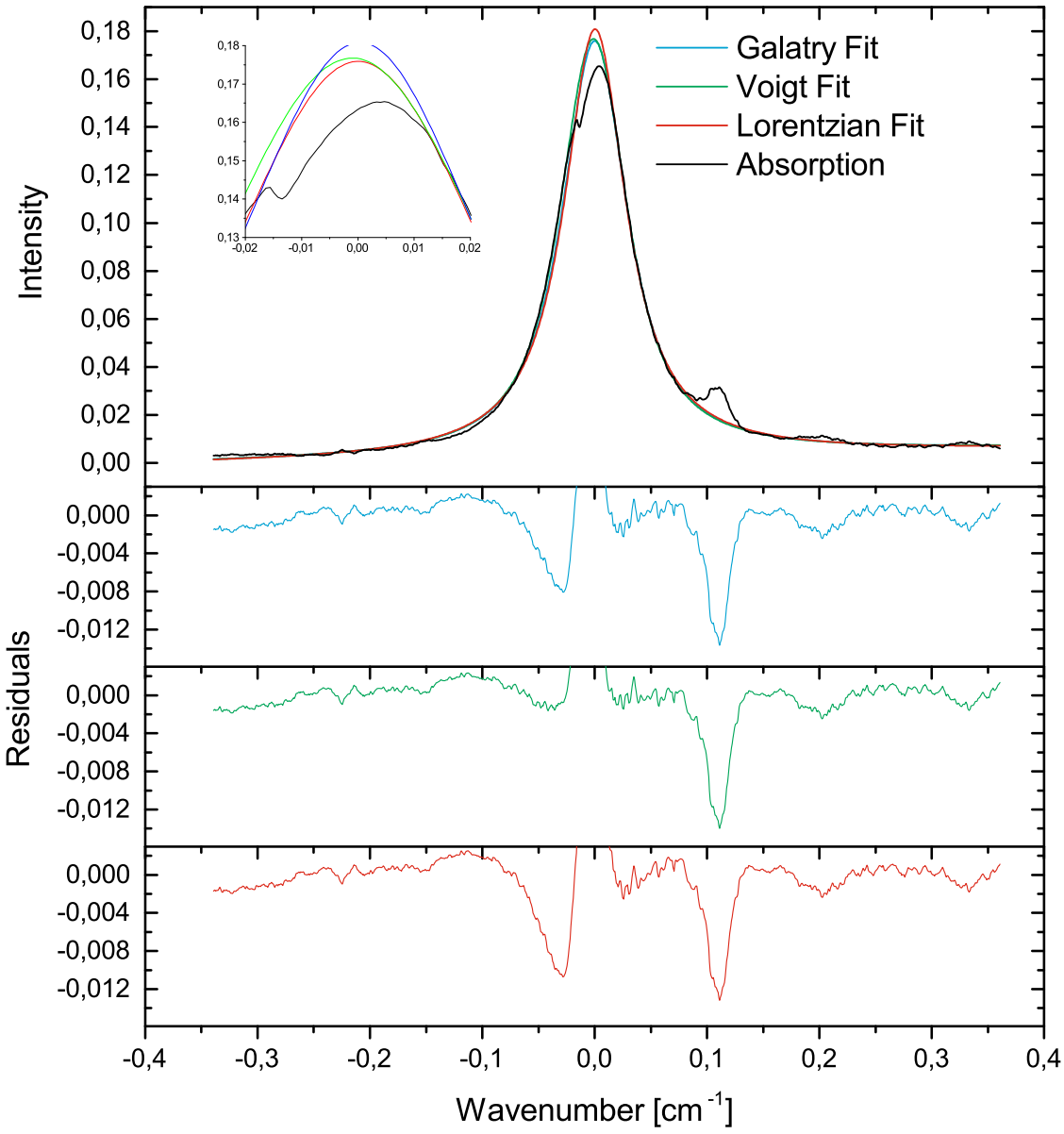

Figure 16: An example of interfered absorption measurement. The residuals of different line-profile fits are plotted on the lower figures. Peaks on the tails of the profile are not as critical as the one on top of the absorption. The fitting function did not do well on this profile and it was excluded as an outlier by first-order optimality criterion. The absorption data were recorded at 29.9.2015 11:52:15 at Nummela on 432 meter path length.

occur, are points when the beam alignment went slightly off and was clipped by the receiver aperture. These situations remained brief as the beam was readjusted as soon as the situation was noted. An exception to this is the night time on 1.10.2015 when the measurement was free running without operator control.

One more noteworthy blackout in the data was caused by rain on 1.10.2015

Table 6: Outlier exclusion criteria and results. The same data are presented graphically in Figures A1 - A4. For the 432 m data the sse threshold is $3 \cdot 10^{-3}$, fopt threshold 10^{-6} and the Hampel windows size 600 points and threshold 3. For the 864 m data the sse threshold is 10^{-3} and the other parameters are the same.

28.9.2015 @ 432 m	No. points	Percentage %
fopt	48	0.3
sse	187	1.3
Hampel	962	6.5
Total	1197	8.1

29.9.2015 @ 432 m	No. points	Percentage %
fopt	171	0.5
sse	1002	3.2
Hampel	460	1.5
Total	1633	5.2

30.9.2015 @ 864 m	No. points	Percentage %
fopt	1108	4.6
sse	4432	18.2
Hampel	264	1.9
Total	5804	25

1.10.2015 @ 432 m	No. points	Percentage %
fopt	2173	6.0
sse	15141	41
Hampel	325	0.9
Total	17639	48

around 15-16 o'clock, seen in Figure A4. Although the absorption feature was still distinguishable, it was far too weak and noisy for spectroscopy. In addition, the assumptions of the density of absorbing molecules most likely had failed at that point and the temperature solution would have been false.

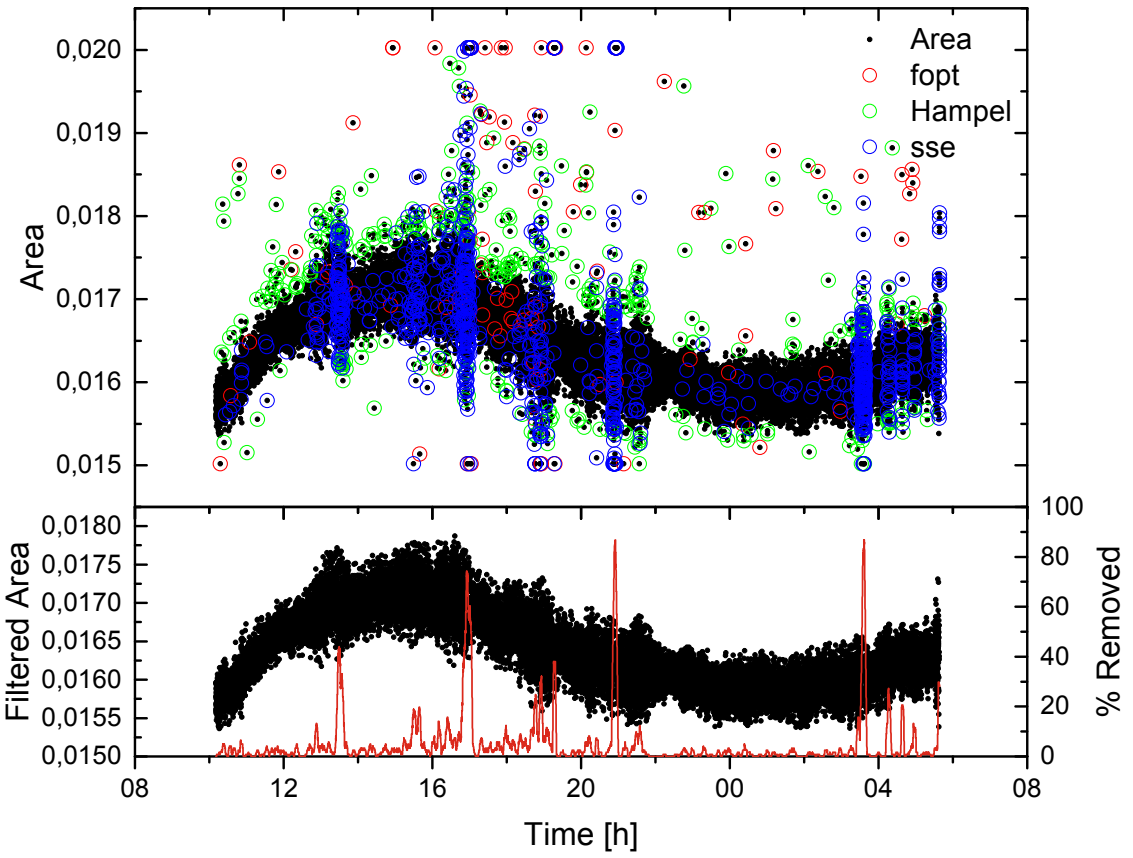

Figure 17: Outlier exclusion results on the 29.9.2015 data. Blue circles indicate the excluded points based on sse criterion, red circles based on the fopt and green circles by the Hampel identifier. On the lower graph is the result of the filtering and percentage of excluded points inside a four minute time frame.

5.2 Calibration

The temperature Equation 17 requires a knowledge of the physical constants $S'_{\eta\eta'}(T_{ref})$ and E'_{η} that are the spectral line intensity at the reference temperature and the lower-state energy. Although these values can be obtained from the HITRAN database, it is necessary to calibrate the setup by determining $S'_{\eta\eta'}(T_{ref})$ and E'_{η} directly from observations. In this way all the temperature dependencies inaccuracies of the system will be accounted for. The calibration values were computed by minimising the sum of squares of $A - A(T, p, RH, S'_{\eta\eta'}(T_{ref}), E'_{\eta})$ with respect to $S'_{\eta\eta'}(T_{ref})$ and E'_{η}, where A is the line area determined by the Galatry fit and $A(T, p, RH, S'_{\eta\eta'}(T_{ref}), E'_{\eta})$ is the theoretical line area.

Calculation of the theoretical line area requires knowledge of the absorbing gas temperature. An approximation of the temperature was acquired with the electronic temperature sensors along the optical path. Since spectroscopic thermometry gives the average temperature, the best correspondence could be found by calculating the average of all the electronic sensors with one half weighting for the ones located at

end points of the optical path. In addition, the choice of reference temperature was tested by performing the calibration for all possible sensor combinations. In this way, we could discover information on how sensitive the calibration is to the reference selection and give an uncertainty estimate for the instrument. The best possible scenario would have been to calibrate the setup once in tightly controlled laboratory environment and use the obtained values for all the field measurements. This goal had to be relaxed because of various reasons and the calibration values were derived from the data of the field measurements. The full list of results of the calibration is given in Appendix B and a summary in Table 7. The used calibration values are listed at the bottom of Table 7. The lower state energy was held constant for all the measurements but the reference line intensity had to be readjusted for the two different distances. The reason for this is discussed later on in this subsection.

Table 7: The calibrated values of the reference spectral line intensity and the lower state energy. The literature values are from HITRAN 2012 database. The calibrated values for each day are the plain results of whole data set using weighted average of the electronic sensors as reference. On the bottom of the table are the weighted averages that were used to present the results in Section 6. RSD stands for relative standard deviation that is the standard deviation divided my the arithmetic average of the sample data. Line intensities S_0 are in the units of $10^{-25}\mathrm{cm}^{-1}/(\mathrm{molecule\ cm}^{-2})$ and lower state energies in cm^{-1}. ΔT designates total temperature change over the time period.

Dataset	Time period	ΔT	$S'_{\eta\eta'}(T_{ref})$	RSD	E'_{η}	RSD
HITRAN	-	-	1.099	-	1248	-
28.9.2015 @ 432 m	17:07-02:14	5 °C	.8970	0.2	1232	0.4
29.9.2015 @ 432 m	10:11-05:35	7 °C	.8840	0.8	1167	2.6
30.9.2015 @ 864 m	12:43-03:53	9 °C	.9010	0.5	1236	1.8
1.10.2015 @ 864 m	11:20-23:47	6 °C	.8987	0.4	1209	2.2
Average			.8952		1211	
Values for 432 m			.8905		1211	
Values for 864 m			.8999		1211	

The values shown for each day in Table 7 are the weighted averages of the sensor array. The respective relative standard deviations (RSD) describes the variations between different sensor combinations. As expected, the RSD values are higher for cloudless days, which can be seen by comparing the results with the weather information in Figure 12. The listings in Appendix B show that variations between reference sensor combinations are quite significant. This gives reason to question the sensors usability as a reference. Since there were at worse only five sensor along a distance of 864 m, the average may not describe the true average temperature well enough. In addition, only the weather station was even close to meteorological standards

which allows us to suspect how closely the sensors resembled the temperature of the ambient air. For example, the sun was at least partially shining on most of the days which could easily lead the sensors to heat up over the true ambient temperature. On the other hand wind might cool them down as they were not wind protected. Such effects were tried to be minimised by placing the sensors under an aluminium foil covered platform and place them on mostly shadowed areas.

The calibration results for each measurement session, presented in the upper part of Table 7, deviate from HITRAN values at most by 20 % percent in the case of $S'_{\eta\eta'}(T_{ref})$ and at most by 7 % in the case of E'_{η}. Between the datasets the deviations are 1 % and 4 % percentage, respectively. Since the setup was not designed to improve or to match the HITRAN database, the difference to HITRAN values is not as interesting as the spread between datasets. To better understand the tolerances allowed in the calibration, numerical simulations were conducted for the sensitivity of the temperature solution to the parameters $S'_{\eta\eta'}(T_{ref})$ and E'_{η}. First of all, $S'_{\eta\eta'}(T_{ref})$ and E'_{η} are not independent but linked by an exponential relationship as can be seen from Equation 17. Secondly, although both parameters contribute to the offset and the sensitivity of the line area to temperature translation, they have different sensitivities and opposite signs. For example, a 1 % increase in line strength will create -0.7 ℃ offset and 1 % increase in lower-state energy will create +0.2 ℃ offset. In order to better demonstrate the effect of variation in the calibration parameters, the spectroscopic temperature of the first measurement day was solved for each of the four value pairs. By default, all of these solutions should be equal and the variation in $S'_{\eta\eta'}(T_{ref})$ and E'_{η} be covered by noise and other uncertainties. However, the differences are clearly visible as seen in Figure 18. The data set from 29.9.2015 differs most in gain and 1.10.2015 most in offset. This is in harmony with results in Table 7.

The method of using a single measurement session as calibration reference was clearly not successful. The next best choice is to use the data from all four days collectively to determine the values that best fit the whole data. Instead of the simple arithmetic average of all days given in Table 7, the line strength values were determined separately as a distance specific average and the energy value as an average of all four days. This choice was justified by examining closely the calibration tables in Appendix B. The line strengths on 864 m are systematically higher by some 0.8 % than on 432 m for corresponding energy values. If a simple average of all four days would be used it would cause 0.3 ℃ offset. The difference can be understood qualitatively by considering the density of interferences in the absorption profile caused by falling debris and insects. It was already seen in the previous subsection (Table 6) that the absorption features on longer distances experience far more disturbances. When the disturbances lie on top of the profile, the fitting algorithm can not distinguish them from the real data and the fitting results systematically in a larger line area. When this occurs statistically often, the line area is systematically increased on average.

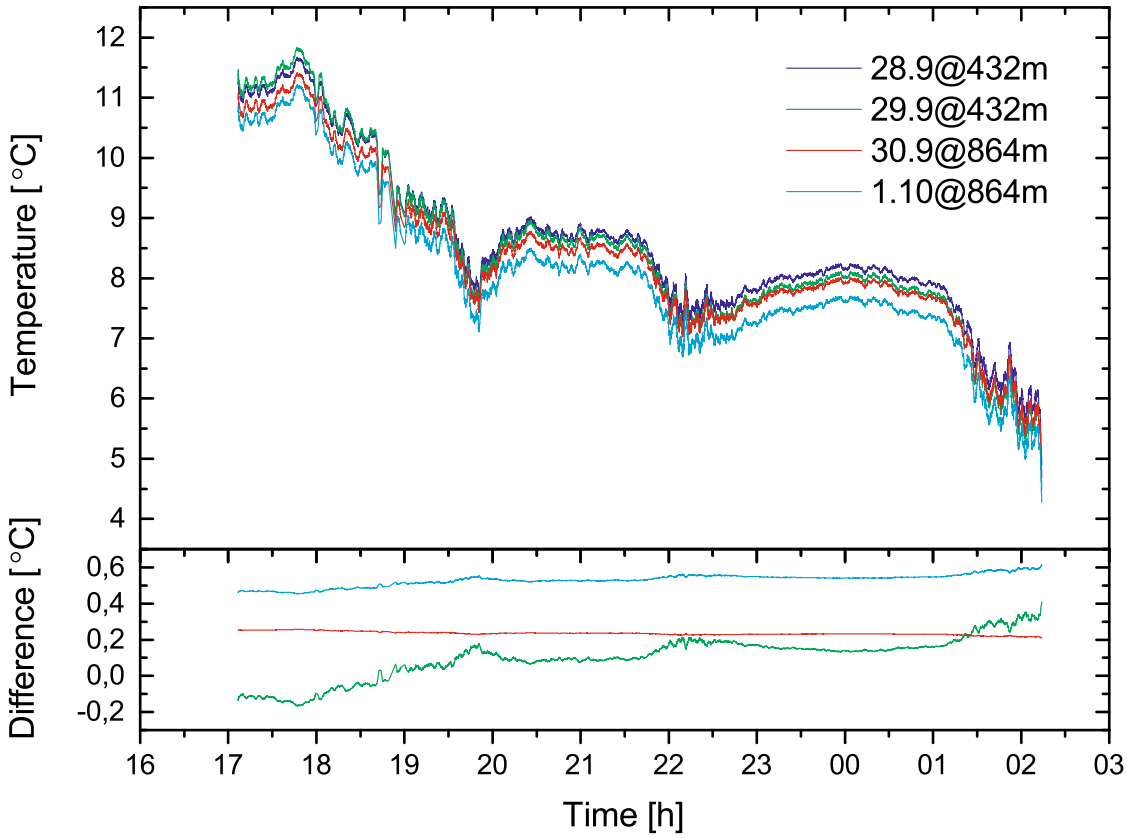

Figure 18: Spectroscopic temperature of 28.9.2015 solved with different calibration values from Table 7. The lower graph presents the differences of each days solution to the 28.9.2015 solution.

5.3 Temperature and distance

The spectroscopic temperature T was solved from Equation 17 using Matlabs numerical zero finder function *fzero*[6]. The simple interpolation based solver was a great choice as a close estimate to the solution was always available and the error function behaves well around the solution. With the additional help of parallel computing the temperature equations could be solved for a whole dataset in less than five seconds. For application purposes the data were smoothed with standard moving average filter of 2 min window size. Since the filter could not handle not-a-number (NaN) values, resultant of the excluding process, the NaN values were temporarily replaced with interpolated values. The results are presented in the next Section 6.

In EDM measurements the line of sight distance from the instrument to the retroreflector prism is referred to as slope distance. The slope distance is often reduced to a horizontal or a vertical distance by accounting for the elevation difference between the two points of interest. However, in the scope of this thesis, only slope distances were of interest. The smoothed temperature data and the weather information of

[6]Online documentation available: http://se.mathworks.com/help/matlab/ref/fzero.html

the Vaisala weather station was used for correcting the slope distances recorded with the Leica tacheometer. Three types of corrections were applied: first velocity correction, scale correction and constant correction. By default an EDM deduces the slope distance according to the following equation

$$d' = \frac{c}{n_{ref}} \frac{\Delta t'}{2}, \tag{22}$$

where d' is the distance displayed on the EDM instrument, c is the speed of light in vacuum, $\Delta t'$ the measured flight time of the signal to the reflector and back and n_{ref} the reference refractive index of the instrument. The reference refractive index is instrument specific, fixed by the manufacturer so that at certain conditions that best represent the expected measurement situation, the instrument displays an accurate reading [30]. When the conditions are not met, which in general is the case, one must apply the first velocity correction K', given in Equation 23, where n_L is the actual refractive index determined, for example, with the equations in Section 1.2.

$$K' = \left(\frac{n_{ref} - n_L}{n_L} \right) d' \tag{23}$$

The scale and the constant correction, d_0 and d_1 respectively, are instrument specific calibrated corrections. When these together with the first velocity correction are applied, the correct distance d is given in simplified form as

$$d = \frac{n_{ref}}{n_L} d'(1 + d_1) + d_0. \tag{24}$$

For the Leica TC2003 tacheometer, used in the field measurements, the correction constants are given in Table 8.

Table 8: Correction constant for the Leica TC2003 no. 439351 tacheometer. The values were provided by FGI.

Correction	Symbol	Value
Reference refractive index	n_{ref}	1.0002818
Scale correction	a_0	2.35 mm/km
Constant correction	a_1	0.35 mm

6 Results

The results, presented in this section, were acquired during the field measurements at Nummela standard baseline, described in Section 4. The primary goal of the outdoor measurement campaign was to demonstrate that the chosen method of spectroscopic thermometry is capable of producing accurate results over long distances. This was accomplished by comparing the spectroscopic thermometer to an ensemble of conventional Pt-100 and other electronic temperature sensors. However, since we had at worse only five sensors distributed over a distance of 864 m, the interpretation of correct average temperature close to or below 100 mK level is vague. The results are summarised and discussed in Subsection 6.1 and presented as a whole in Appendix C.

To address the ambiguity of correct temperature, we used the Nummela standard baseline as a guaranteed stable reference and transformed the reliability of the thermometers into distance measurements with a help of a tacheometer. Tacheometer is a type of EDM that bases its operation on the transit time of 850 nm laser pulses. Thus, the length measure is proportional to the refractive index of air, which in turn is a function of temperature, pressure, humidity and wavelength as discussed in Section 1.2. A refractive index compensation for the distance measurements was executed in two different ways: using the average temperature of the electrical sensors and using Oxytherm – the developed spectroscopic instrument. A summary of the results is given and discussed in Subsection 6.2 and presented as a whole in Appendix D.

6.1 Temperature

Temperature results for four successive days for distances of 432 m and 864 m, are presented as a whole in Appendix C and two most representative samples in figures 19 and 20. Examination of the results can be embarked on by directly comparing Oxytherm to the average of the electronic sensors. Overall, when taking into consideration the uncertainties in both methods, Oxytherm can be considered as reliable and accurate as an array of a few electronic sensors in determining the average ambient temperature over long distances in non-rainy days. Moreover, as Oxytherm has many improvement possibilities, as will be discussed in Section 7, the Oxytherm has potential to perform even better than electronic sensors, as was already proven in laboratory experiments [25]. The most distinguishable differences between the spectroscopic and electronic results can be seen in Figure C1. In the beginning of the data and around midnight the temperatures clearly differ from each other. For now, we do not have data to support the spectroscopic results so the deviation must be accounted for some unknown factors, or considered real. On the data set of the 29^{th} day in Figure 19, a similar offset can be observed during night time. The 29^{th} day was especially difficult day due to relatively strong sunlight which caused instruments and sensors to heat more than in favourable conditions. The electronic sensors deviate from each other up to 2 ℃ during that day. We thereby claim that the night time data is more reliable and the observed deviation is accounted for by

the uncertainty in the calibration values. The results of the 864 m distance on 30th and 1st day, in figures C3, C4 and 20, follow tightly the electronic reference data in limits of estimated uncertainty. The break in data around 16 o'clock on 1.10.2015 was caused by rain, of which Oxytherm is not able to tolerate. On both days also the effect of a cold night can be seen. The temperature readings are quite widely spread similarly to a sunny day, which lets us assume that a cold cloudless night can be nearly as challenging as a sunny day. This observation is also supported by [30] and explained by the heat transfer between air and ground, which is found to be similar during cloudless days and nights, although opposite in direction.

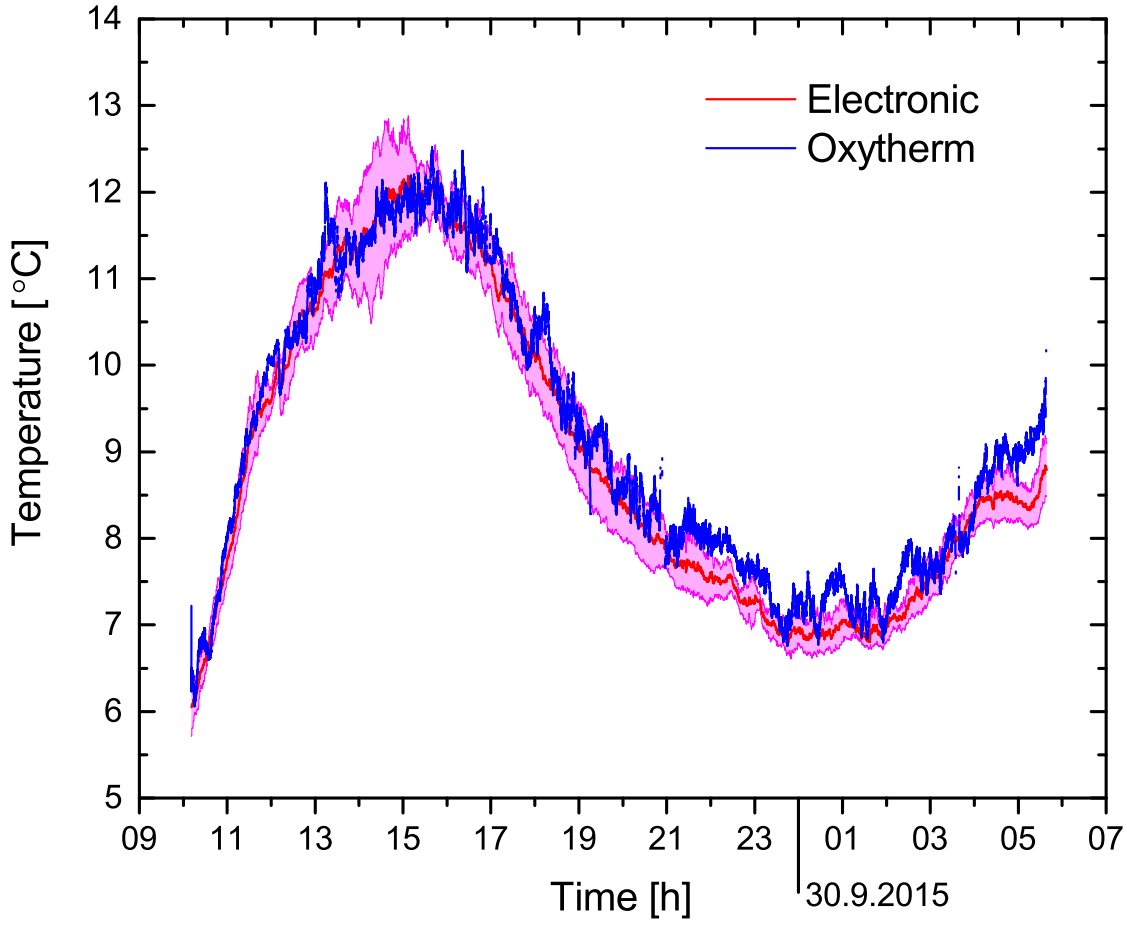

Figure 19: Temperature results from measurements that began on 29.9.2015 at Nummela standard baseline on 432 m distance. The red line and its standard deviation is the weighted average of electronic sensors as described in Section 5. The blue line is the spectroscopic temperature with 2 minute averaging time. The points excluded in line area processing (Figure 17) are not plotted in this figure.

The spectroscopic temperature was solved using calibration parameters that best fit all of the recorded data as discussed in Section 5.2. This method unfortunately leaves us no independent results. Thus aspects, such as the systems transportability, can not be truly evaluated. However, based on our hands on experience we assess that

the laser system is robust to transport. Resting on the uncertainty of the calibration, given in Section 5, we give a conservative ±0.3 ℃ uncertainty estimate for the accuracy of Oxytherm measurements. We estimate that this could be improved to the level of ±0.1 ℃ with improvements that are discussed later in Section 7. For example, in the current setup, drifting of the Rx signal offset causes changes in the temperature that are estimated to be in the order of 50 mK.

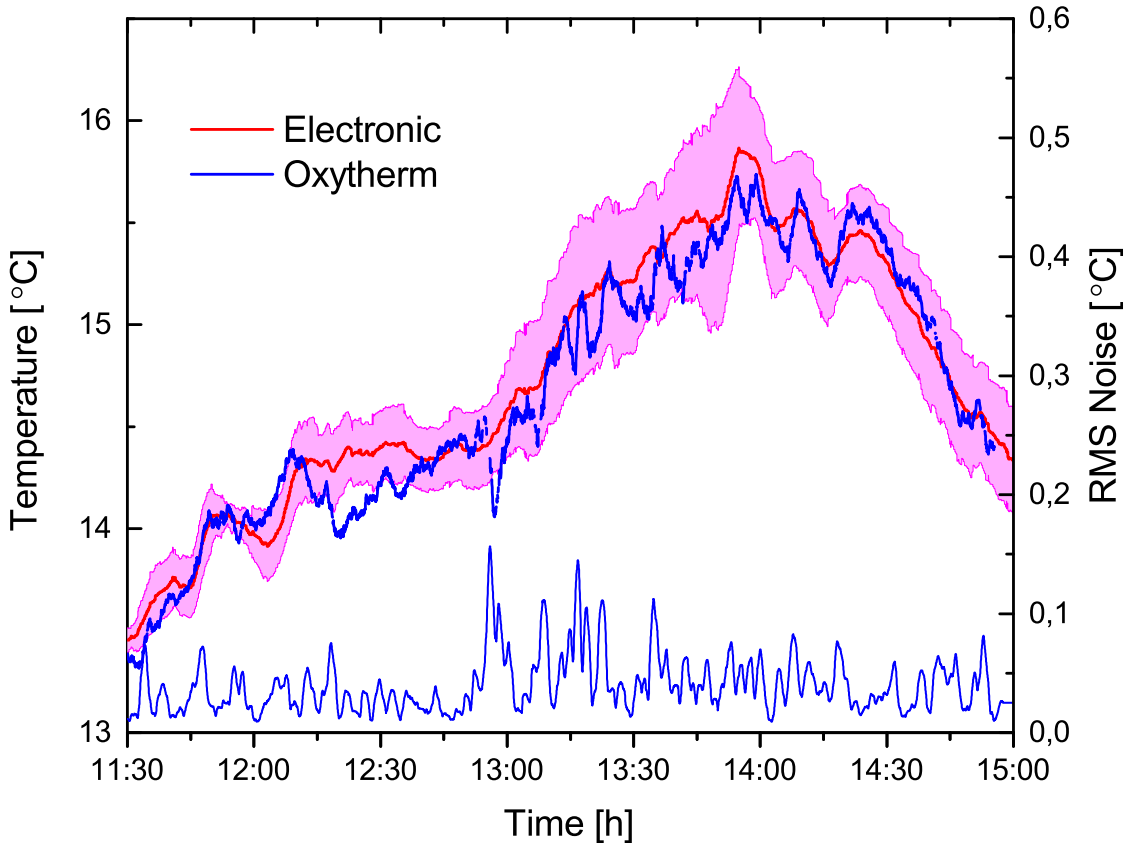

Figure 20: Part of the temperature results from measurements that began on 10.1.2015 at Nummela standard baseline on 864 m distance, presented as measure of the top performance of the current setup. The red line and its standard deviation is the weighted average of electronic sensors as described in Section 5. The blue line is the spectroscopic temperature with 2 minute averaging time. The points excluded in line area processing (Figure A4) are not plotted in this figure. The RMS noise is the moving standard deviation, calculated from the averaged spectroscopic data with 2 minute window size.

In Figure 20 the beginning of the measurement session on 1.10.2015 at 864 m is given as an example of top performance of the current setup. The weather at that time interval was considered fairly favourable, allowing the system noise to be evaluated. As seen in Figure 20, Oxytherm can reach RMS noise of 50 mK with 120 s sample time, whereas the average of the sensor array experiences RMS noise of 20 mK. Based on the conducted indoors tests in stable conditions, it is safe to assume

that most of the noise, seen by the sensors, is real temperature noise and Oxytherm is thus reaching close to that limit. In addition, the response time of the 3 mm diameter stainless steel Pt-100 sensors was not studied in this work. However, it is safe to assume that sensors with less mass would have resulted in higher noise. RMS noise is calculated as a standard deviation of 120 s sample of data. For non-averaged spectroscopic data the RMS noise is 300 mK with 2 s sample time. The following is considered as favourable conditions: low temperature gradients, few insects or flying debris in the beam path and a clouded sky. High temperature gradients will hamper the beam pointing and introduce higher observed noise that can not be distinguished from the system noise. Anything intersecting the measurement beam will affect the absorption profile fitting and measured temperature. In unfavourable conditions the Oxytherm experiences RMS noise in the order of 150 mK or more while the sensors have no significant increase in noise. The Oxytherm RMS noise estimate can be compared to an earlier setup, that was based on two line ratio measurement [25]. A 7 mK RMS noise was reported on 67 m OPL and in laboratory environment with the same 120 s sample time. Although the reported noise is significantly smaller, the conditions and distance were very different. Characterising the long distance setup in similar conditions would not be possible in practise and real temperature changes will almost always increase the RMS noise. We therefore conclude that the achievable well below 100 mK RMS noise outdoors on a 864 m OPL, having still room for improvements, is an excellent result.

6.2 Refractive index compensation

The comparison measurements with the tacheometer for three successive days for distances of 432 m and 864 m are presented as a whole in Appendix D and summarized in this subsection with an example of the measurements on 29$^{\text{th}}$ that has been used as an example through out this thesis. The comparison measurements with the tacheometer confirm that the implementations of spectroscopic and electronic thermometry were successful. As can be seen from the figures in Appendix D and Figure 21, both methods provide corrections that well compensate the change in the refractive index of air on the available precision scale. For example, in the lower part of Figure 21 the measured slope distance changes in total by 2 mm (4.6 ppm) solely due to the ambient conditions. As the air temperature increases, the measured distance decreases. Applying the weather correction results in standard deviation of 0.15 mm for spectroscopic and 0.08 mm for electronic corrections. For the results on the 864 m observation pillar, given in the Appendix D, the standard deviations of both correction methods are close to 0.15 mm. This can be interpreted so that the spectroscopic method performs relatively better on longer distances compared to few electronic sensors. The deviation of the uncorrected distances from the calibrated is greater for the 864 m because of the scale correction of the EDM.

Although the spectroscopic correction experiences more noise, on average it provides slightly better compensation. Taking into account the uncertainties, the difference can not be stated for sure though. Even though our main interest was not to perform distance metrology in absolute sense, it is noteworthy that on average

the Oxytherm results, in Table 9, are within the expanded total standard uncertainty (95%) of 0.26 mm of the calibrated slope distances, whereas the conventional sensors fail on this part. Table 9 lists the difference of the average results and the calibrated slope distances of the baseline, which is also indicated by the arrows in the corresponding figures. The systematic error in the results for each day is easily explained by the inaccuracies of the tacheometer and its calibration. The

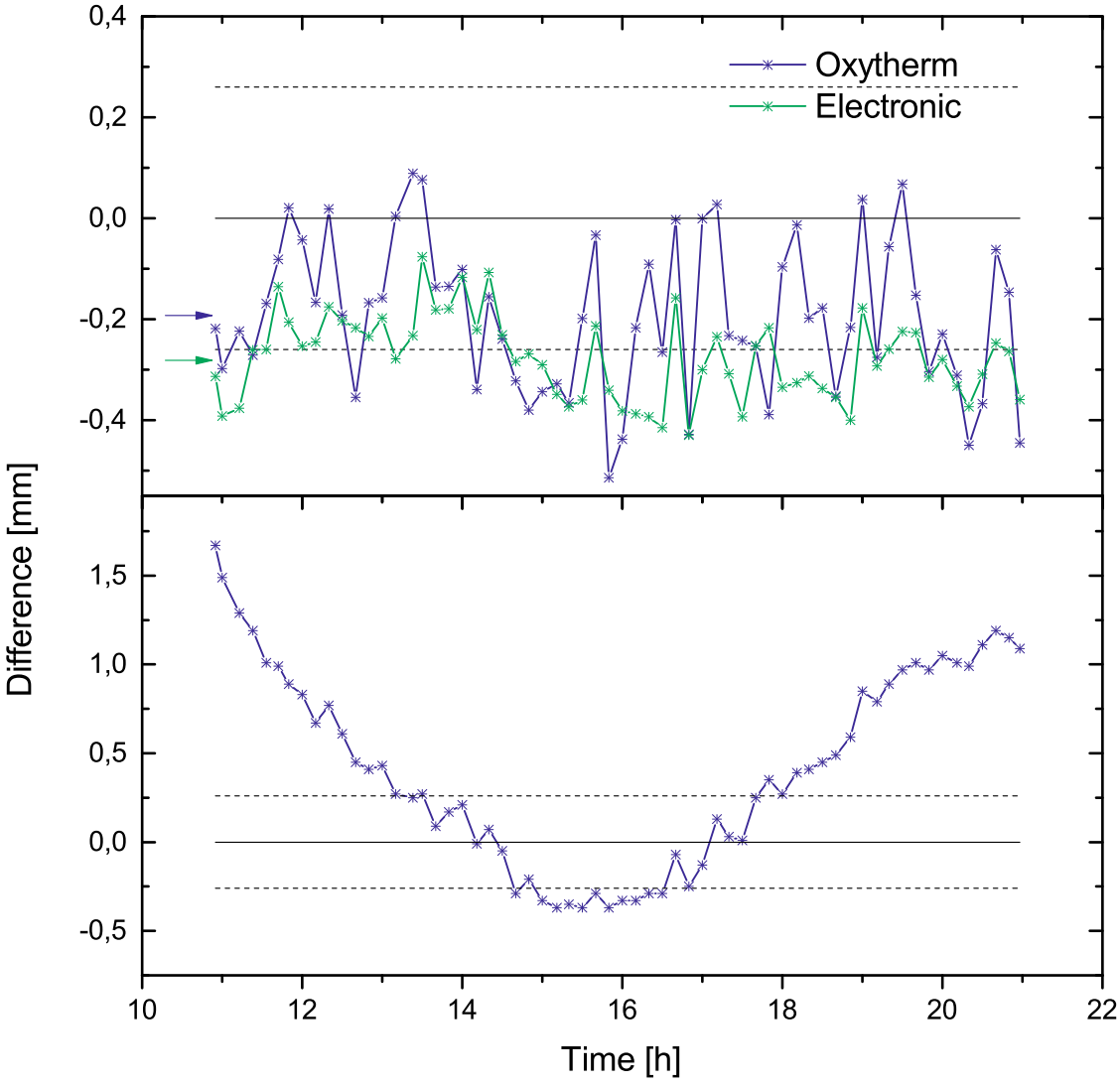

Figure 21: Slope distances of the Nummela standard baseline on 432 m path length between observation pillars 0-432. The measurements were conducted on 29.9.2015 with Leica TC2003 tacheometer. The upper graph present the difference of the calibrated slope distance to the corrected slope distances and the lower graph the difference to the uncorrected slope distances. The arrows indicate the mean values of the respective data. The dashed lines are the 95% confidence intervals of the calibrated slope distance.

manufacturer promises an accuracy of $\pm(1\,\mathrm{mm} + 1\,\mathrm{ppm})$ for the instrument, which includes consideration of several error mechanisms such as some of the ones listed in Table 12.1 of [30]. Especially, FGI has noted that the calibrated scale factor can change even daily by more than the uncertainty estimate of an individual calibration would allow. Related to the error source considerations, the approximative formula for the refractive index of air was tested against the accurate version, provided by FGI. The difference was found to be below 0.01 mm, which is insignificant for the results presented in this thesis. Overall, given that the weather was not especially favourable for baseline measurements, the results can be considered excellent as this is the first time a spectroscopic method of thermometry has been used for a long distance measurement in outdoor environment.

Table 9: The averaged results of baseline slope distances, measured with Leica TC2003 No. 439351 tacheometer, with respect to the calibrated slope distances. The calibrations were performed by FGI on 7-9 September and November 9-11, 2015 with the same instrument and in favourable weather conditions. The average expanded total standard uncertainty (95%) of the calibrated slope distances is 0.26 mm, which is not scale-dependent. The calibration results are traceable to the SI unit metre through the used Väisälä interference comparator and the quartz metre system [52].

Date	Calibrated [mm]	Spectroscopic [mm]	Electronic [mm]
29.9.2015	432099.03 ±0.26	+0.19	+0.28
30.9.2015	864132.56 ±0.26	-0.20	-0.33
1.10.2015	864132.56 ±0.26	-0.17	-0.23

7 Conclusions

A thermometer, based on method of direct oxygen absorption spectroscopy, has been constructed, described and experimentally demonstrated in real field conditions in a typical distance measurement configuration for the first time. The chosen method is capable of determining the average temperature of air traversed by the measurement beam up to distances of 864 m. When combined with an EDM or other optical length measuring device the method provides potentially excellent spatial and temporal overlap with the EDM measurement beam and therefore, accurate air temperature for refractive index compensation. The instrument has proven to measure the air temperature to an estimated uncertainty of $\pm$300 mK with RMS noise below 100 mK for 120 s averaging time and up to 864 m in distance. The results have been reliably confirmed by providing refractive index corrections for a tacheometer measuring the slope distances of the Nummela standard baseline and comparing the results to an array of electronic thermometers.

Although the spectroscopy-based method experiences larger uncertainty and higher noise compared to the electronic sensors, on average it provided slightly better compensation of the refractive index of air. A sub ppm standard deviation was achieved in the length measures, which is at the limit of the EDM accuracy and resolution. Validating temperature results of higher accuracy would have required more sophisticated distance measurement.

The greatest challenge limiting the accuracy of the spectroscopic thermometer was obtaining the line parameters from the absorption profile. The problem originated from flying debris and insects intersecting the measurement beam, and occasionally also from bad beam pointing or turbulences, causing poor signal to noise ratio. Although we used a robust line-profile fitting method that minimises the effect of outliers, the difference of favourable and unfavourable conditions are clearly visible in the data as higher and lower noise levels even though clearly poor line-profile fits were excluded. In addition, since beam intersection by any cause always causes increase in the measured absorption, a systematic error in the measured line area was found when more disturbances were present. This effect is dependent on the measurement distance since the probability of intersection naturally changes accordingly. For the above-mentioned reason, we had to use different reference line intensity value for the 432 m and 864 m results. Without this, a $\sim$ 500 mK offset would have resulted.

A secondary reason for high uncertainty was that a reliable enough calibration of the setup could not be performed. The calibration would have required a similar optical device from which the temperature could have been deduced, or extremely favourable weather so that an array of electronic sensors placed along the optical path would have resulted in closer approximation of the average temperature. Neither of these were available, which is why we had to rely the calibration on the average of all measurement days.

For the disadvantages of the current setup we have several refinement ideas to propose: The effect of disturbances in the absorption feature could be analysed theoretically and a model to predict it on different distances could be derived. Or, the robust fitting routine could be modified to assume that the disturbances always

occur to the same direction. Also, some other simpler software methods could be implemented, such as averaging the measured absorption features with a median filter instead of the fitted line areas. However, even better would be to employ a second frequency locked laser diode to measure only the disturbances, which could then be removed from the absorption feature. This laser should be coupled to the same optical path and could be detected, for example, with wavelength selective optics or on different lock-in frequency. The laser system could be made more robust by using less free space components and, especially, a fibre coupled laser diode with integrated TEC element. Moreover, an auto offset function for the lock-in detection could be implemented to account for varying offsets. A closed-loop pointing control of the measurement beam should also be employed. Last, the temperature regulation of the rack unit could be improved quite easily.

Overall, the project goal of constructing a state-of-the-art spectroscopic thermometer for long distances was achieved.

Acknowledgement

This work is supported by the European Metrology Research Programme (EMRP). The EMRP is jointly funded by the EMRP participating countries within EURAMET and the European Union.

References

[1] L. Michalski, *Temperature measurement*. John Wiley & Sons, 2 ed., 2001.

[2] P. R. N. Childs, J. R. Greenwood, and C. A. Long, "Review of temperature measurement," *Review of Scientific Instruments*, vol. 71, no. 8, pp. 2959–2978, 2000.

[3] V. Korpelainen and A. Lassila, "Acoustic method for determination of the effective temperature and refractive index of air in accurate length interferometry," *Optical Engineering*, vol. 43, no. 10, pp. 2400–2409, 2004.

[4] D. Pavia, G. Lampman, G. Kriz, and J. Vyvyan, *Introduction to spectroscopy*. Cengage Learning, 5 ed., 2014.

[5] W. Demtröder, *Laser Spectroscopy Vol. 1: Basic Principles*. Springer-Verlag, 4 ed., 2008.

[6] W. Demtröder, *Laser Spectroscopy Vol. 2: Experimental Techniques*. Springer-Verlag, 4 ed., 2008.

[7] M. G. Allen, "Diode laser absorption sensors for gas-dynamic and combustion flows," *Measurement Science and Technology*, vol. 9, no. 4, pp. 545–562, 1998.

[8] M. Arroyo and R. Hanson, "Absorption measurements of water-vapor concentration, temperature, and line-shape parameters using a tunable ingaasp diode laser," *Applied Optics*, vol. 32, no. 30, pp. 6104–6116, 1993.

[9] D. Baer, M. Newfield, N. Gopaul, and R. Hanson, "Multiplexed diode-laser sensor system for simultaneous H_2O, O_2, and temperature measurements," *Optics Letters*, vol. 19, no. 22, pp. 1900–1902, 1994.

[10] T. Cai, H. Jia, G. Wang, W. Chen, and X. Gao, "A sensor for measurements of temperature and water concentration using a single tunable diode laser near 1.4 μm," *Sensors and Actuators A: Physical*, vol. 152, no. 1, pp. 5–12, 2009.

[11] V. Ebert, T. Fernholz, C. Giesemann, H. Pitz, H. Teichert, J. Wolfrum, and H. Jaritz, "Simultaneous diode-laser-based *in situ* detection of multiple species and temperature in a gas-fired power plant," *Proceedings of the Combustion Institute*, vol. 28, no. 1, pp. 423–430, 2000.

[12] A. Farooq, J. B. Jeffries, and R. K. Hanson, "*In situ* combustion measurements of H_2O and temperature near 2.5 μm using tunable diode laser absorption," *Measurement Science and Technology*, vol. 19, no. 7, p. 075604, 2008.

[13] J. T. Liu, J. B. Jeffries, and R. K. Hanson, "Large-modulation-depth 2f spectroscopy with diode lasers for rapid temperature and species measurements in gases with blended and broadened spectra," *Applied Optics*, vol. 43, no. 35, pp. 6500–6509, 2004.

[14] J. T. Liu, G. B. Rieker, J. B. Jeffries, M. R. Gruber, C. D. Carter, T. Mathur, and R. K. Hanson, "Near-infrared diode laser absorption diagnostic for temperature and water vapor in a scramjet combustor," *Applied Optics*, vol. 44, no. 31, pp. 6701–6711, 2005.

[15] G. Rieker, H. Li, X. Liu, J. Liu, J. Jeffries, R. Hanson, M. Allen, S. Wehe, P. Mulhall, H. Kindle, *et al.*, "Rapid measurements of temperature and H_2O concentration in IC engines with a spark plug-mounted diode laser sensor," *Proceedings of the Combustion Institute*, vol. 31, no. 2, pp. 3041–3049, 2007.

[16] G. B. Rieker, J. B. Jeffries, and R. K. Hanson, "Calibration-free wavelength-modulation spectroscopy for measurements of gas temperature and concentration in harsh environments," *Applied Optics*, vol. 48, no. 29, pp. 5546–5560, 2009.

[17] S. T. Sanders, J. Wang, J. B. Jeffries, and R. K. Hanson, "Diode-laser absorption sensor for line-of-sight gas temperature distributions," *Applied Optics*, vol. 40, no. 24, pp. 4404–4415, 2001.

[18] J. Shao, L. Lathdavong, P. Kluczynski, S. Lundqvist, and O. Axner, "Methodology for temperature measurements in water vapor using wavelength-modulation tunable diode laser absorption spectrometry in the telecom C-band," *Applied Physics B*, vol. 97, no. 3, pp. 727–748, 2009.

[19] J. A. Silver and D. J. Kane, "Diode laser measurements of concentration and temperature in microgravity combustion," *Measurement Science and Technology*, vol. 10, no. 10, pp. 845–852, 1999.

[20] H. Teichert, T. Fernholz, and V. Ebert, "Simultaneous in situ measurement of CO, H_2O, and gas temperatures in a full-sized coal-fired power plant by near-infrared diode lasers," *Applied Optics*, vol. 42, no. 12, pp. 2043–2051, 2003.

[21] X. Zhou, X. Liu, J. B. Jeffries, and R. Hanson, "Development of a sensor for temperature and water concentration in combustion gases using a single tunable diode laser," *Measurement Science and Technology*, vol. 14, no. 8, p. 1459, 2003.

[22] X. Zhou, J. Jeffries, and R. Hanson, "Development of a fast temperature sensor for combustion gases using a single tunable diode laser," *Applied Physics B*, vol. 81, no. 5, pp. 711–722, 2005.

[23] V. Spagnolo, L. Dong, A. A. Kosterev, D. Thomazy, J. H. Doty III, F. K. Tittel, *et al.*, "Modulation cancellation method for measurements of small temperature differences in a gas," *Optics Letters*, vol. 36, no. 4, pp. 460–462, 2011.

[24] T. Hieta and M. Merimaa, "Spectroscopic measurement of air temperature," *International Journal of Thermophysics*, vol. 31, no. 8, pp. 1710–1718, 2010.

[25] T. Hieta, M. Merimaa, M. Vainio, J. Seppä, and A. Lassila, "High-precision diode-laser-based temperature measurement for air refractive index compensation," *Applied Optics*, vol. 50, no. 31, pp. 5990–5998, 2011.

[26] F. Pollinger *et al.*, "Metrology for long distance surveying: A joint attempt to improve traceability of long distance measurements," *International Association of Geodesy Symposia*, vol. 143, pp. 1–6, 2015.

[27] G. Bönsch and E. Potulski, "Measurement of the refractive index of air and comparison with modified edlén's formulae," *Metrologia*, vol. 35, no. 2, pp. 133–139, 1998.

[28] P. E. Ciddor, "Refractive index of air: new equations for the visible and near infrared," *Applied Optics*, vol. 35, no. 9, pp. 1566–1573, 1996.

[29] P. E. Ciddor and R. J. Hill, "Refractive index of air. 2. group index," *Applied Optics*, vol. 38, no. 9, pp. 1663–1667, 1999.

[30] J. M. Rueger, *Electronic distance measurement: an introduction*. Springer-Verlag Berlin Heidelberg, fourth ed., 1996.

[31] F. Pollinger, T. Hieta, M. Vainio, N. R. Doloca, A. Abou-Zeid, K. Meiners-Hagen, and M. Merimaa, "Effective humidity in length measurements: comparison of three approaches," *Measurement Science and Technology*, vol. 23, no. 2, p. 025503, 2012.

[32] F. Pollinger, T. Meyer, J. Beyer, N. R. Doloca, W. Schellin, W. Niemeier, J. Jokela, P. Häkli, A. Abou-Zeid, and K. Meiners-Hagen, "The upgraded PTB 600 m baseline: a high-accuracy reference for the calibration and the development of long distance measurement devices," *Measurement Science and Technology*, vol. 23, no. 9, p. 094018, 2012.

[33] The International Association of Geodesy (IAG), "Recommendations for long distance measurements, Resolution 3", Available: http://www.gfy.ku.dk/~iag/HB2000/part2/iag_res.htm, Accessed: 2015-12-01.

[34] L. S. Rothman, C. Rinsland, A. Goldman, S. Massie, D. Edwards, J. Flaud, A. Perrin, C. Camy-Peyret, V. Dana, J.-Y. Mandin, *et al.*, "The HITRAN molecular spectroscopic database and HAWKS (HITRAN atmospheric workstation): 1996 edition," *Journal of Quantitative Spectroscopy and Radiative Transfer*, vol. 60, no. 5, pp. 665–710, 1998.

[35] S. Abrarov, B. M. Quine, and R. K. Jagpal, "High-accuracy approximation of the complex probability function by fourier expansion of exponential multiplier," *Computer Physics Communications*, vol. 181, no. 5, pp. 876–882, 2010.

[36] J. Humlíček, "Optimized computation of the Voigt and complex probability functions," *Journal of Quantitative Spectroscopy and Radiative Transfer*, vol. 27, no. 4, pp. 437–444, 1982.

[37] J. Wang, *Dicke narrowing and speed-dependent effects in dispersion signals: Influence on assessment of concentration and spectral parameters by noise-immune cavity-enhanced optical heterodyne molecular spectrometry*. Doctoral dissertation, Umeå Universitet, 2013.

[38] L. Galatry, "Simultaneous effect of doppler and foreign gas broadening on spectral lines," *Physical Review*, vol. 122, no. 4, pp. 1218–1223, 1961.

[39] P. L. Varghese and R. K. Hanson, "Collisional narrowing effects on spectral line shapes measured at high resolution," *Applied Optics*, vol. 23, no. 14, pp. 2376–2385, 1984.

[40] P. Maddaloni, P. Malara, and P. De Natale, "Simulation of Dicke-narrowed molecular spectra recorded by off-axis high-finesse optical cavities," *Molecular Physics*, vol. 108, no. 6, pp. 749–755, 2010.

[41] D. R. Lide, *CRC handbook of chemistry and physics*. CRC Press, 2010.

[42] J. R. Welty, C. E. Wicks, G. Rorrer, and R. E. Wilson, *Fundamentals of Momentum, Meat, and Mass Transfer*. John Wiley & Sons, 2008.

[43] D. J. Robichaud, J. T. Hodges, L. R. Brown, D. Lisak, P. Masłowski, L. Y. Yeung, M. Okumura, and C. E. Miller, "Experimental intensity and lineshape parameters of the oxygen A-band using frequency-stabilized cavity ring-down spectroscopy," *Journal of Molecular Spectroscopy*, vol. 248, no. 1, pp. 1–13, 2008.

[44] P. Duggan, P. Sinclair, R. Berman, A. May, and J. R. Drummond, "Testing Lineshape Models: Measurements $\nu = 1 - 0$ CO Broadened by He and Ar," *Journal of Molecular Spectroscopy*, vol. 186, no. 1, pp. 90–98, 1997.

[45] R. Gamache, S. Kennedy, R. Hawkins, and L. Rothman, "Total internal partition sums for molecules in the terrestrial atmosphere," *Journal of Molecular Structure*, vol. 517, pp. 407–425, 2000.

[46] A. L. Buck, "New equations for computing vapor pressure and enhancement factor," *Journal of Applied Meteorology*, vol. 20, no. 12, pp. 1527–1532, 1981.

[47] T. Hieta, *Applied diode laser spectroscopy and characterization of optical fiber nonlinearity*. Doctoral dissertation, Aalto University, 2011.

[48] R. Schermaul and R. C. Learner, "Precise line parameters and transition probability of the atmospheric a band of molecular oxygen 16 o 2," *Journal of Quantitative Spectroscopy and Radiative Transfer*, vol. 61, no. 6, pp. 781–794, 1999.

[49] L. Rothman *et al.*, "The HITRAN2012 molecular spectroscopic database," *Journal of Quantitative Spectroscopy and Radiative Transfer*, vol. 130, pp. 4–50, 2013.

[50] IDEX Optics & Photonics, "Fundamental Optics", Available online: http://marketplace.idexop.com/store/SupportDocuments/Fundamental_Optics_OverviewWEB.pdf, Accessed: 2015-11-17.

[51] J. Jokela *et al.*, *Length in Geodesy–On Metrological Traceability of a Geospatial Measurand*. PhD thesis, Aalto University, 2014.

[52] Finnish Geospatial Research Institute FGI, "Certificate of Calibration no. 24/2015".

A Outlier removal

Results of the outlier removal, described in Subsection 5.1.

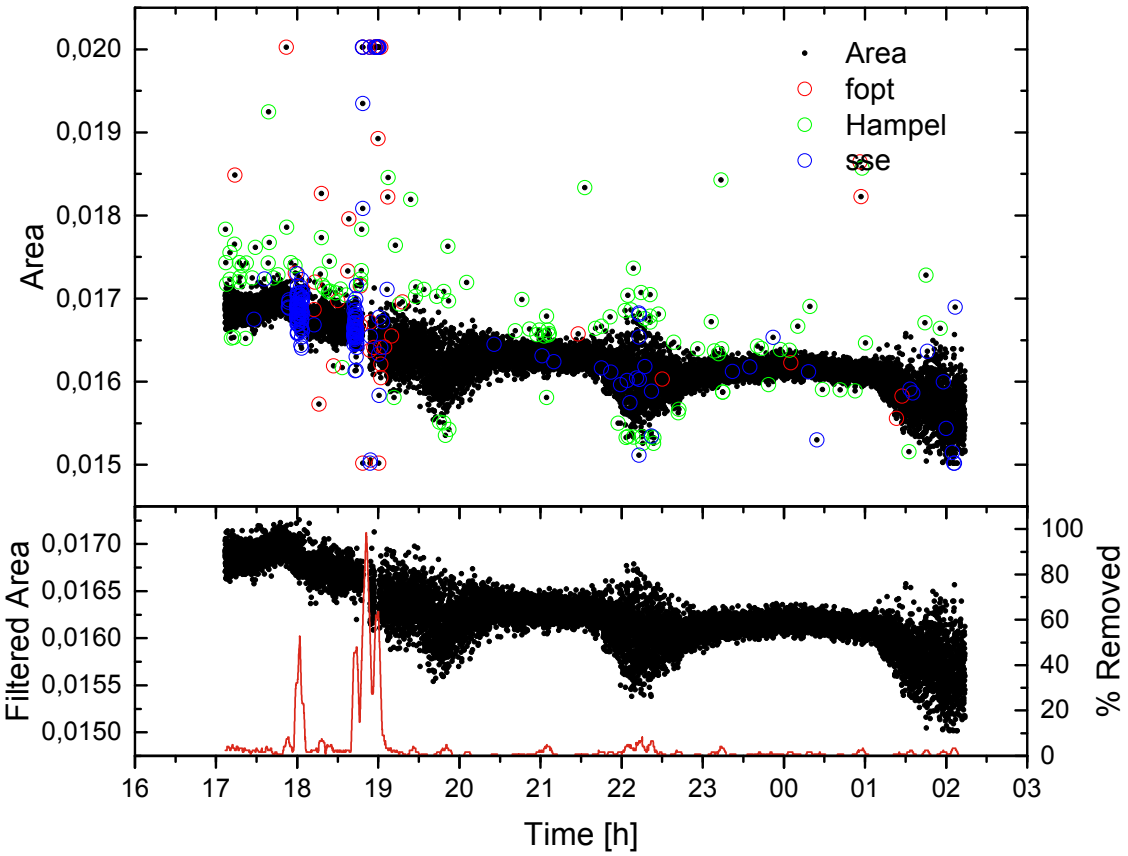

Figure A1: Outlier exclusion results on the 28.9.2015 data. The blue circles indicate the excluded points based on sse criterion, the red circles based on the fopt and the green circles by the Hampel identifier. On the lower graph is the result of the filtering and percentage of excluded points inside a four minute time frame.

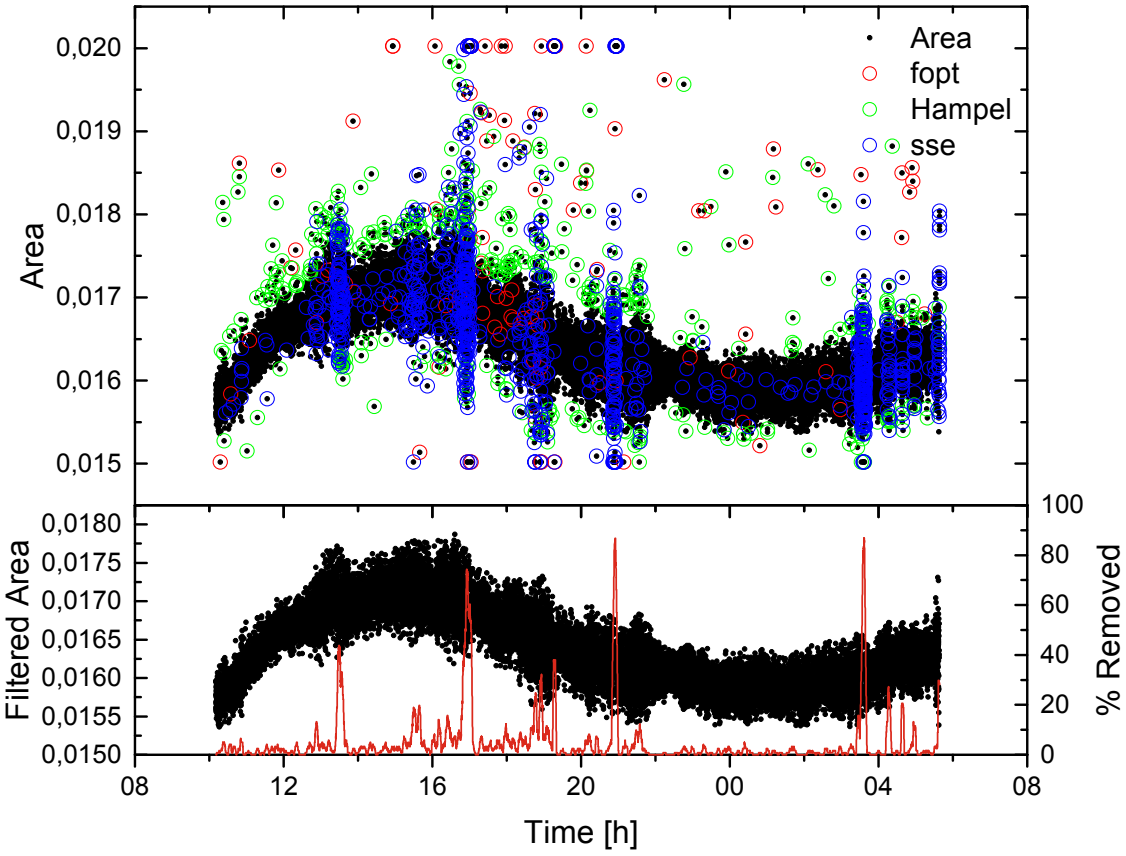

Figure A2: Outlier exclusion results on the 29.9.2015 data. The blue circles indicate the excluded points based on sse criterion, the red circles based on the fopt and the green circles by the Hampel identifier. On the lower graph is the result of the filtering and percentage of excluded points inside a four minute time frame.

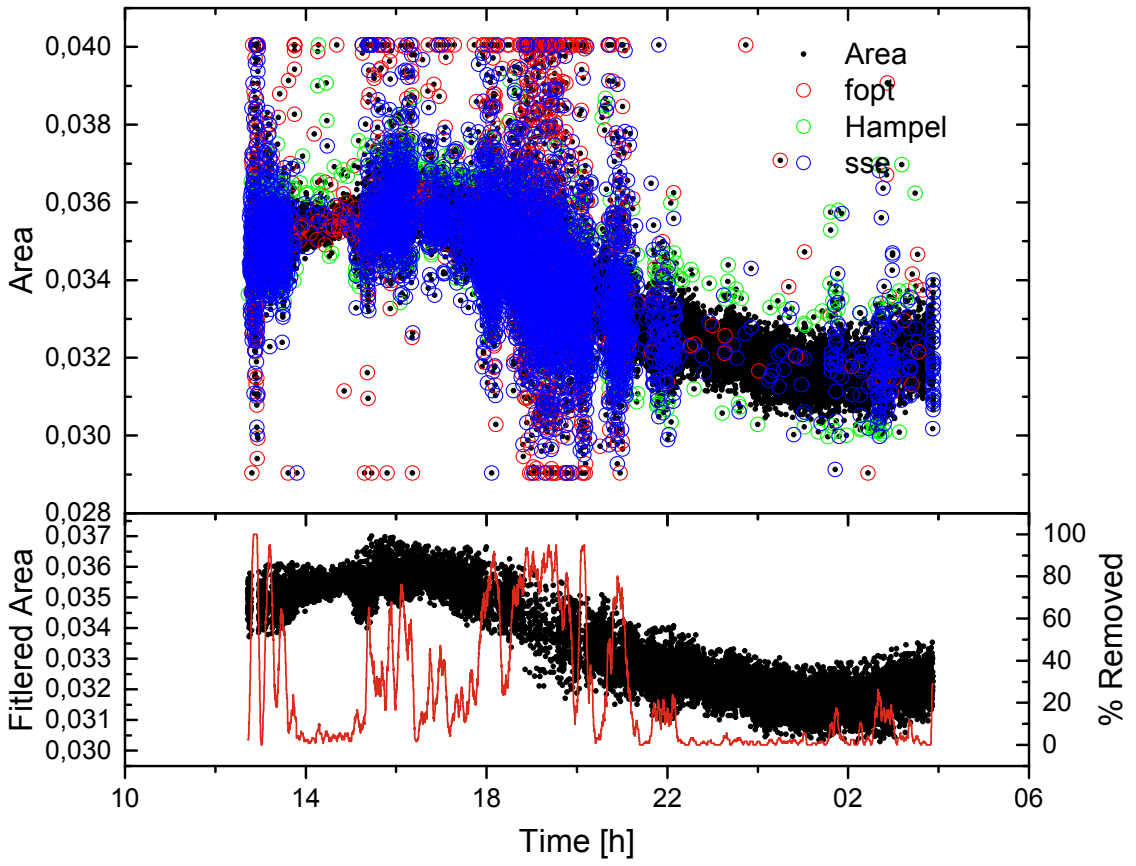

Figure A3: Outlier exclusion results on the 30.9.2015 data. The blue circles indicate the excluded points based on sse criterion, the red circles based on the fopt and the green circles by the Hampel identifier. On the lower graph is the result of the filtering and percentage of excluded points inside a four minute time frame.

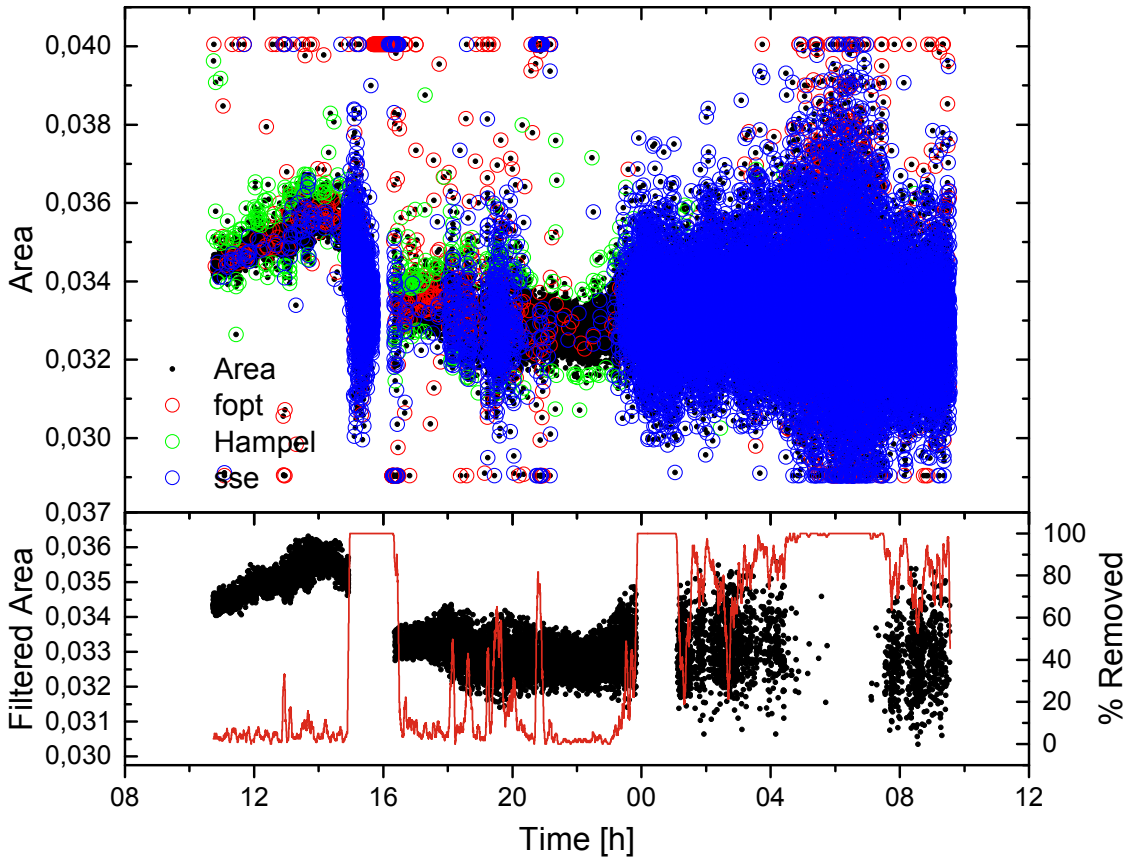

Figure A4: Outlier exclusion results on the 1.10.2015 data. The blue circles indicate the excluded points based on sse criterion, the red circles based on the fopt and the green circles by the Hampel identifier. On the lower graph is the result of the filtering and percentage of excluded points inside a four minute time frame. The blackout in the data around 15-16 o'clock was caused by rain.

B Calibrations

Full list of the calibration results, discussed in Subsection 5.2 is presented in this appendix. In the following tables 'Sensor Weights' columns show the weighting given for each electronic sensor when calculating their average. The sensors are numbered in same order they were placed on the baseline, T1 being closest to the Tx end. T1 is always the Vaisala WXT 520 weather station and the last one the MadgTech PRHTemp logger. In between are the MadgTech Pt-100 loggers, one of which was stolen during the first measurements on 864 m.

Table B1: Calibration values from time interval 28.9.2015 17:07:04 to 29.9.2015 02:14:06 on 432 m path length with all possible reference sensor combinations.

Parameters		Sensor Weights					
S0	En	T2	T3	T4	T5	T1	T6
.8970	1232	1	1	1	1	0.5	0.5
.8964	1229	1	1	1	1	0.5	0
.8973	1232	1	1	1	1	0	0.5
.8966	1229	1	1	1	1	0	0
.8969	1233	1	1	1	0	0.5	0.5
.8961	1230	1	1	1	0	0.5	0
.8973	1234	1	1	1	0	0	0.5
.8964	1230	1	1	1	0	0	0
.8969	1231	1	1	0	1	0.5	0.5
.8961	1227	1	1	0	1	0.5	0
.8973	1232	1	1	0	1	0	0.5
.8965	1227	1	1	0	1	0	0
.8968	1233	1	1	0	0	0.5	0.5
.8957	1228	1	1	0	0	0.5	0
.8974	1234	1	1	0	0	0	0.5
.8960	1228	1	1	0	0	0	0
.8979	1233	1	0	1	1	0.5	0.5
.8973	1230	1	0	1	1	0.5	0
.8985	1234	1	0	1	1	0	0.5
.8978	1230	1	0	1	1	0	0
.8981	1236	1	0	1	0	0.5	0.5
.8973	1232	1	0	1	0	0.5	0
.8991	1238	1	0	1	0	0	0.5
.8981	1233	1	0	1	0	0	0
.8980	1231	1	0	0	1	0.5	0.5
.8972	1227	1	0	0	1	0.5	0
.8989	1233	1	0	0	1	0	0.5
.8981	1228	1	0	0	1	0	0
.8985	1235	1	0	0	0	0.5	0.5
.8973	1229	1	0	0	0	0.5	0
.9002	1239	1	0	0	0	0	0.5

.8989	1230	1	0	0	0	0	0
.8962	1231	0	1	1	1	0.5	0.5
.8954	1228	0	1	1	1	0.5	0
.8965	1232	0	1	1	1	0	0.5
.8955	1228	0	1	1	1	0	0
.8958	1233	0	1	1	0	0.5	0.5
.8945	1228	0	1	1	0	0.5	0
.8962	1234	0	1	1	0	0	0.5
.8945	1228	0	1	1	0	0	0
.8959	1230	0	1	0	1	0.5	0.5
.8947	1225	0	1	0	1	0.5	0
.8963	1231	0	1	0	1	0	0.5
.8948	1224	0	1	0	1	0	0
.8952	1231	0	1	0	0	0.5	0.5
.8929	1224	0	1	0	0	0.5	0
.8957	1234	0	1	0	0	0	0.5
.8919	1221	0	1	0	0	0	0
.8972	1232	0	0	1	1	0.5	0.5
.8962	1228	0	0	1	1	0.5	0
.8979	1234	0	0	1	1	0	0.5
.8968	1229	0	0	1	1	0	0
.8972	1236	0	0	1	0	0.5	0.5
.8956	1230	0	0	1	0	0.5	0
.8985	1240	0	0	1	0	0	0.5
.8962	1231	0	0	1	0	0	0
.8970	1230	0	0	0	1	0.5	0.5
.8955	1223	0	0	0	1	0.5	0
.8984	1233	0	0	0	1	0	0.5
.8966	1222	0	0	0	1	0	0
.8967	1234	0	0	0	0	0.5	0.5
.8921	1217	0	0	0	0	0.5	0
.9012	1250	0	0	0	0	0	0.5
.8967	1231						

Table B2: Calibration values from time interval 29.9.2015 10:11:16 to 30.9.2015 05:35:19 on 432 m path length with all possible reference sensor combinations.

Parameters		Sensor Weights					
S0	En	T2	T3	T4	T5	T1	T6
.8840	1167	1	1	1	1	0.5	0.5
.8833	1166	1	1	1	1	0.5	0
.8878	1184	1	1	1	1	0	0.5
.8875	1185	1	1	1	1	0	0
.8811	1154	1	1	1	0	0.5	0.5
.8799	1150	1	1	1	0	0.5	0
.8854	1173	1	1	1	0	0	0.5
.8846	1172	1	1	1	0	0	0
.8819	1160	1	1	0	1	0.5	0.5
.8807	1157	1	1	0	1	0.5	0
.8864	1180	1	1	0	1	0	0.5
.8857	1181	1	1	0	1	0	0
.8775	1140	1	1	0	0	0.5	0.5
.8751	1133	1	1	0	0	0.5	0
.8826	1164	1	1	0	0	0	0.5
.8806	1160	1	1	0	0	0	0
.8834	1163	1	0	1	1	0.5	0.5
.8824	1160	1	0	1	1	0.5	0
.8882	1184	1	0	1	1	0	0.5
.8878	1184	1	0	1	1	0	0
.8793	1144	1	0	1	0	0.5	0.5
.8772	1137	1	0	1	0	0.5	0
.8849	1168	1	0	1	0	0	0.5
.8834	1164	1	0	1	0	0	0
.8804	1152	1	0	0	1	0.5	0.5
.8784	1146	1	0	0	1	0.5	0
.8863	1178	1	0	0	1	0	0.5
.8851	1178	1	0	0	1	0	0
.8731	1119	1	0	0	0	0.5	0.5
.8677	1099	1	0	0	0	0.5	0
.8796	1149	1	0	0	0	0	0.5
.8736	1129	1	0	0	0	0	0
.8858	1173	0	1	1	1	0.5	0.5
.8853	1172	0	1	1	1	0.5	0
.8912	1196	0	1	1	1	0	0.5
.8914	1199	0	1	1	1	0	0
.8826	1157	0	1	1	0	0.5	0.5
.8812	1153	0	1	1	0	0.5	0
.8891	1185	0	1	1	0	0	0.5
.8889	1187	0	1	1	0	0	0

.8836	1165	0	1	0	1	0.5	0.5
.8823	1162	0	1	0	1	0.5	0
.8905	1195	0	1	0	1	0	0.5
.8906	1200	0	1	0	1	0	0
.8777	1138	0	1	0	0	0.5	0.5
.8740	1126	0	1	0	0	0.5	0
.8866	1177	0	1	0	0	0	0.5
.8849	1177	0	1	0	0	0	0
.8857	1169	0	0	1	1	0.5	0.5
.8849	1168	0	0	1	1	0.5	0
.8933	1201	0	0	1	1	0	0.5
.8942	1208	0	0	1	1	0	0
.8808	1144	0	0	1	0	0.5	0.5
.8780	1134	0	0	1	0	0.5	0
.8912	1186	0	0	1	0	0	0.5
.8919	1192	0	0	1	0	0	0
.8823	1156	0	0	0	1	0.5	0.5
.8798	1149	0	0	0	1	0.5	0
.8937	1205	0	0	0	1	0	0.5
.8957	1220	0	0	0	1	0	0
.8700	1096	0	0	0	0	0.5	0.5
.8534	1027	0	0	0	0	0.5	0
.8881	1169	0	0	0	0	0	0.5
.8832	1162						

Table B3: Calibration values from time interval 30.9.2015 12:43:26 to 1.10.2015 03:52:53 on 864 m path length with all possible reference sensor combinations.

Parameters		Sensor weights				
S0	En	T2	T3	T4	T1	T5
.9010	1236	1	1	1	0.5	0.5
.8994	1226	1	1	1	0.5	0
.9025	1237	1	1	1	0	0.5
.9009	1225	1	1	1	0	0
.8995	1236	1	1	0	0.5	0.5
.8970	1222	1	1	0	0.5	0
.9013	1237	1	1	0	0	0.5
.8987	1220	1	1	0	0	0
.9035	1253	1	0	1	0.5	0.5
.9017	1243	1	0	1	0.5	0
.9061	1258	1	0	1	0	0.5
.9047	1247	1	0	1	0	0
.9025	1262	1	0	0	0.5	0.5
.8991	1247	1	0	0	0.5	0
.9067	1274	1	0	0	0	0.5
.9038	1257	1	0	0	0	0
.8999	1228	0	1	1	0.5	0.5
.8976	1214	0	1	1	0.5	0
.9017	1227	0	1	1	0	0.5
.8993	1209	0	1	1	0	0
.8973	1225	0	1	0	0.5	0.5
.8927	1199	0	1	0	0.5	0
.8994	1222	0	1	0	0	0.5
.8936	1184	0	1	0	0	0
.9030	1250	0	0	1	0.5	0.5
.9001	1232	0	0	1	0.5	0
.9071	1256	0	0	1	0	0.5
.9048	1233	0	0	1	0	0
.9006	1265	0	0	0	0.5	0.5
.8890	1221	0	0	0	0.5	0
.9104	1297	0	0	0	0	0.5
.9008	1237					

Table B4: Calibration values from time interval 1.10.2015 11:21:48 to 1.10.2015 23:47:35 on 864 m path length with all possible reference sensor combinations.

Parameters		Sensor weights				
S0	En	T2	T3	T4	T1	T5
.8987	1209	1	1	1	0.5	0.5
.8972	1200	1	1	1	0.5	0
.8988	1205	1	1	1	0	0.5
.8971	1195	1	1	1	0	0
.9001	1219	1	1	0	0.5	0.5
.8983	1209	1	1	0	0.5	0
.9007	1216	1	1	0	0	0.5
.8985	1203	1	1	0	0	0
.9006	1227	1	0	1	0.5	0.5
.8988	1218	1	0	1	0.5	0
.9013	1225	1	0	1	0	0.5
.8992	1214	1	0	1	0	0
.9038	1252	1	0	0	0.5	0.5
.9017	1245	1	0	0	0.5	0
.9061	1259	1	0	0	0	0.5
.9042	1252	1	0	0	0	0
.8968	1194	0	1	1	0.5	0.5
.8945	1180	0	1	1	0.5	0
.8966	1186	0	1	1	0	0.5
.8936	1167	0	1	1	0	0
.8981	1203	0	1	0	0.5	0.5
.8945	1182	0	1	0	0.5	0
.8982	1192	0	1	0	0	0.5
.8930	1157	0	1	0	0	0
.8987	1213	0	0	1	0.5	0.5
.8953	1195	0	0	1	0.5	0
.8991	1206	0	0	1	0	0.5
.8941	1176	0	0	1	0	0
.9031	1250	0	0	0	0.5	0.5
.8962	1226	0	0	0	0.5	0
.9095	1270	0	0	0	0	0.5
.8989	1211					

C Temperature results

A full set of temperature results from the measurement campaign at the Nummela standard baseline is given in this appendix.

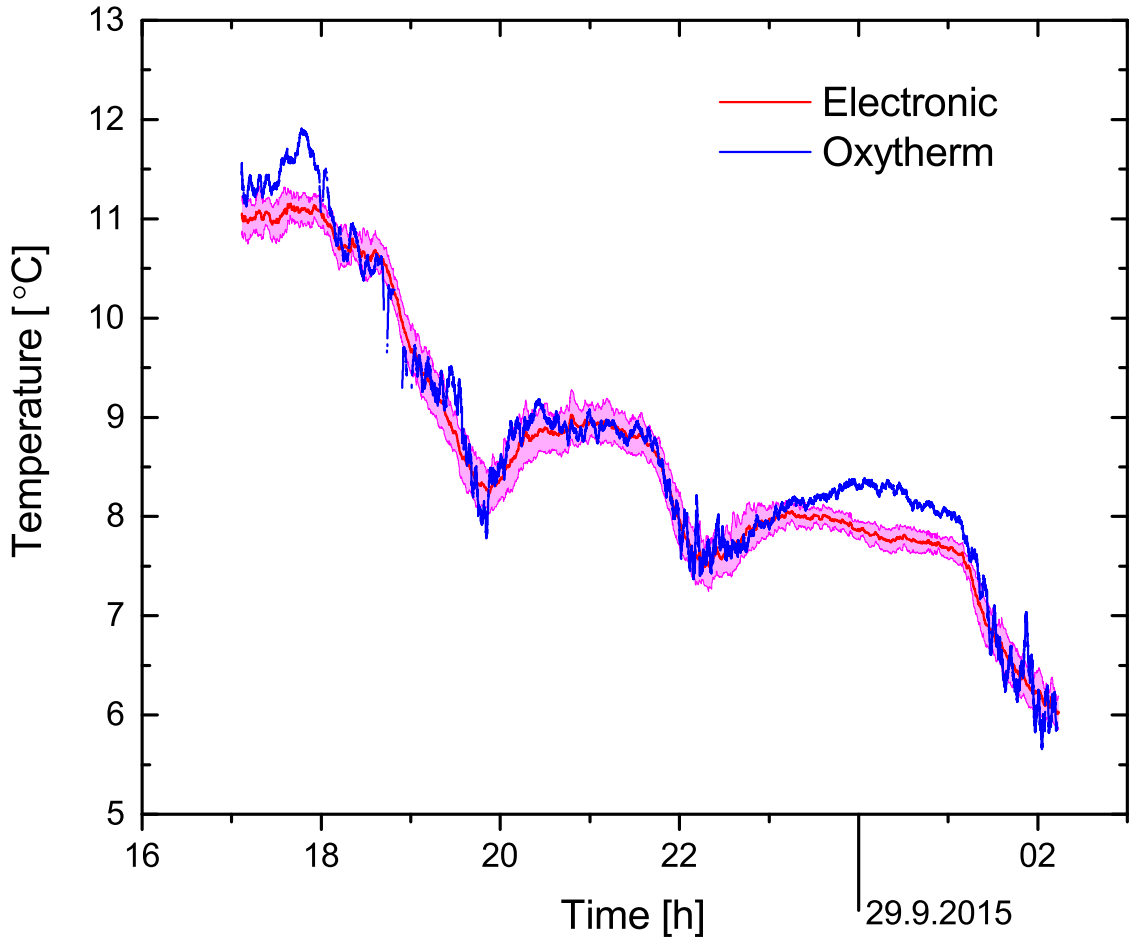

Figure C1: Temperature results from measurements that began on 28.9.2015 at Nummela standard baseline on 432 m distance. The red line and its standard deviation is the weighted average of electronic sensors as described in Section 5. The blue line is the spectroscopic temperature with 2 minute averaging time. The points excluded in line area processing (Figure A1) are not plotted in this figure.

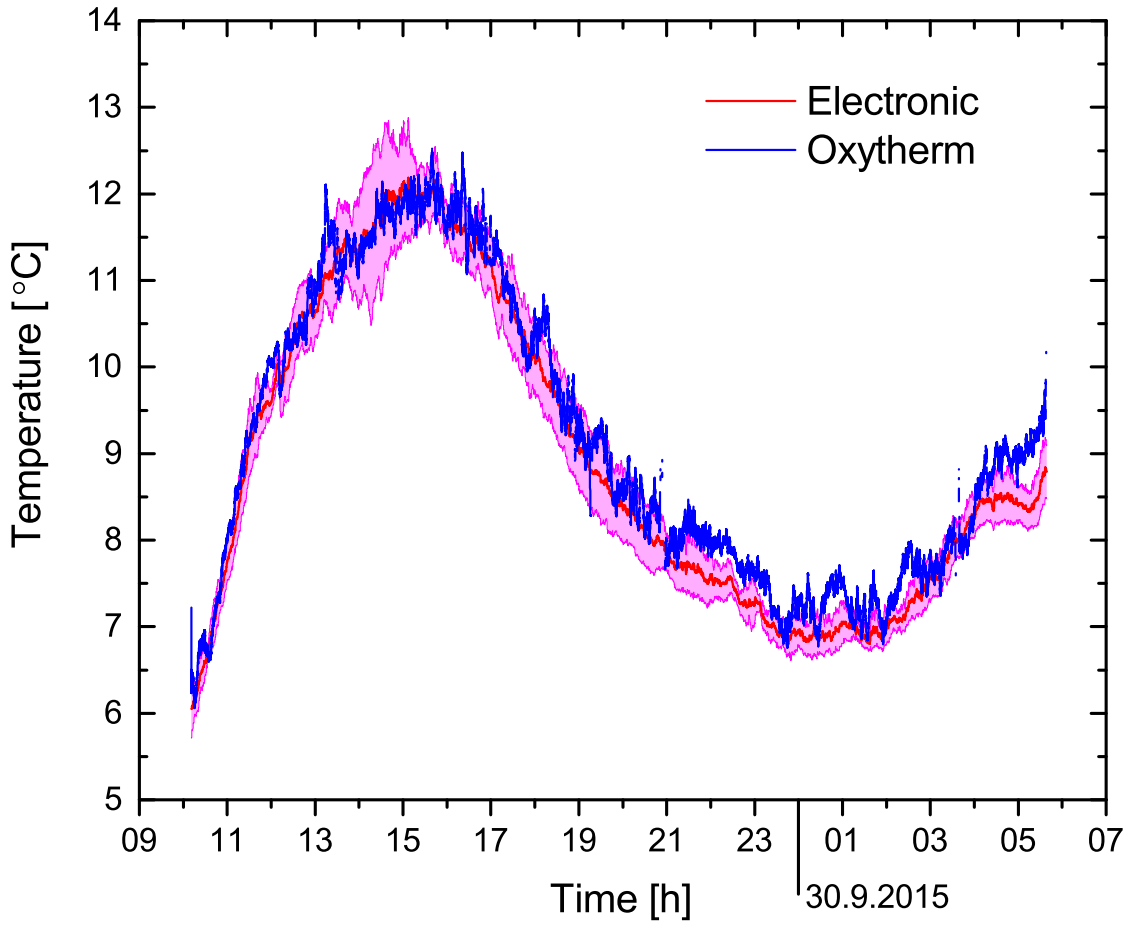

Figure C2: Temperature results from measurements that began on 29.9.2015 at Nummela standard baseline on 432 m distance. The red line and its standard deviation is the weighted average of electronic sensors as described in Section 5. The blue line is the spectroscopic temperature with 2 minute averaging time. The points excluded in line area processing (Figure A2) are not plotted in this figure.

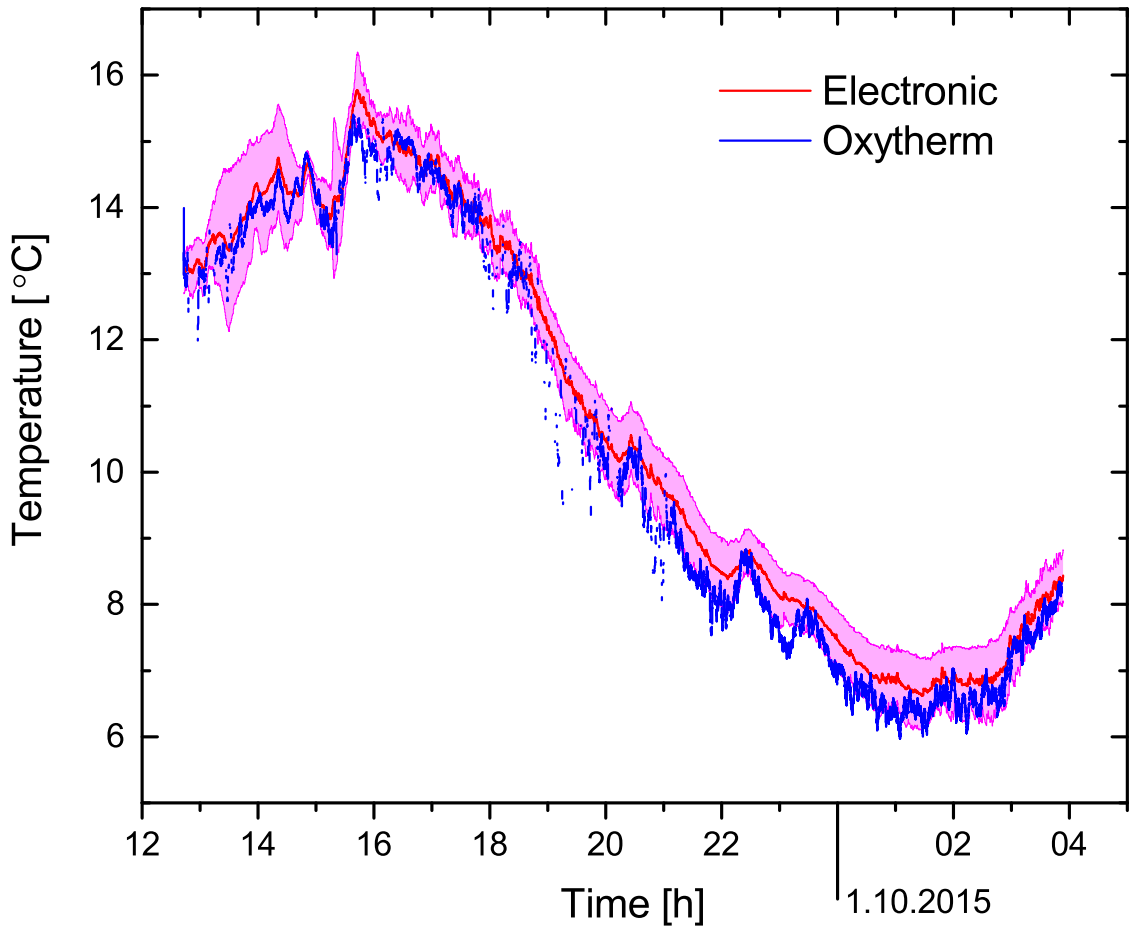

Figure C3: Temperature results from measurements that began on 30.9.2015 at Nummela standard baseline on 864 m distance. The red line and its standard deviation is the weighted average of electronic sensors as described in Section 5. The blue line is the spectroscopic temperature with 2 minute averaging time. The points excluded in line area processing (Figure A3) are not plotted in this figure.

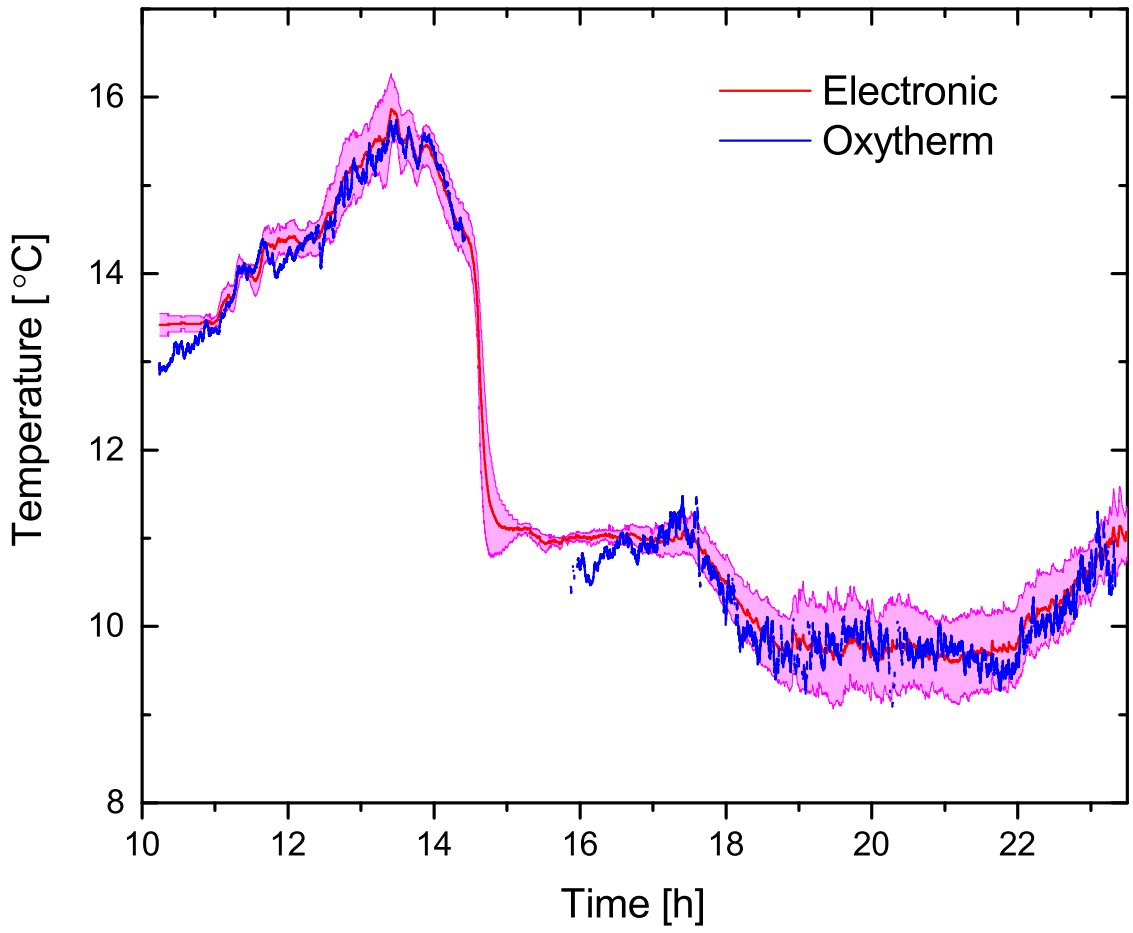

Figure C4: Temperature results from measurements that began on 1.10.2015 at Nummela standard baseline on 864 m distance. The red line and its standard deviation is the weighted average of electronic sensors as described in Section 5. The blue line is the spectroscopic temperature with 2 minute averaging time. The points excluded in line area processing (Figure A4) are not plotted in this figure.

D Distance results

A full set of distance results from the measurement campaign at the Nummela standard baseline is given in this appendix.

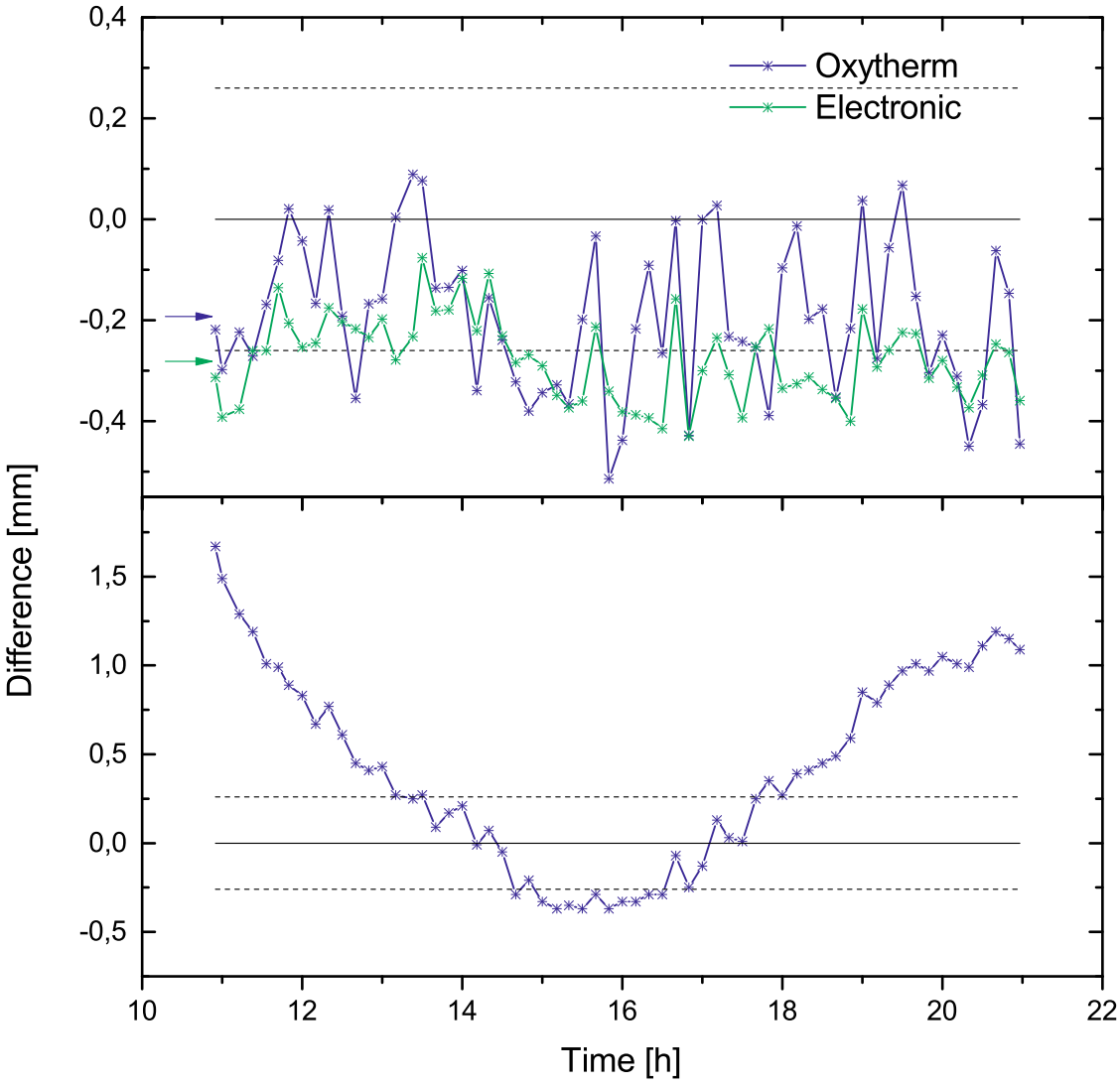

Figure D1: Slope distances of the Nummela standard baseline on 432 m path length between observation pillars 0-432. The measurements were conducted on 29.9.2015 with Leica TC2003 tacheometer. The upper graph presents the difference of the calibrated slope distance to the corrected slope distances and the lower graph the difference to the uncorrected slope distances. The arrows indicate the mean values of the respective data. The dashed lines are the 95% confidence intervals of the calibrated slope distance.

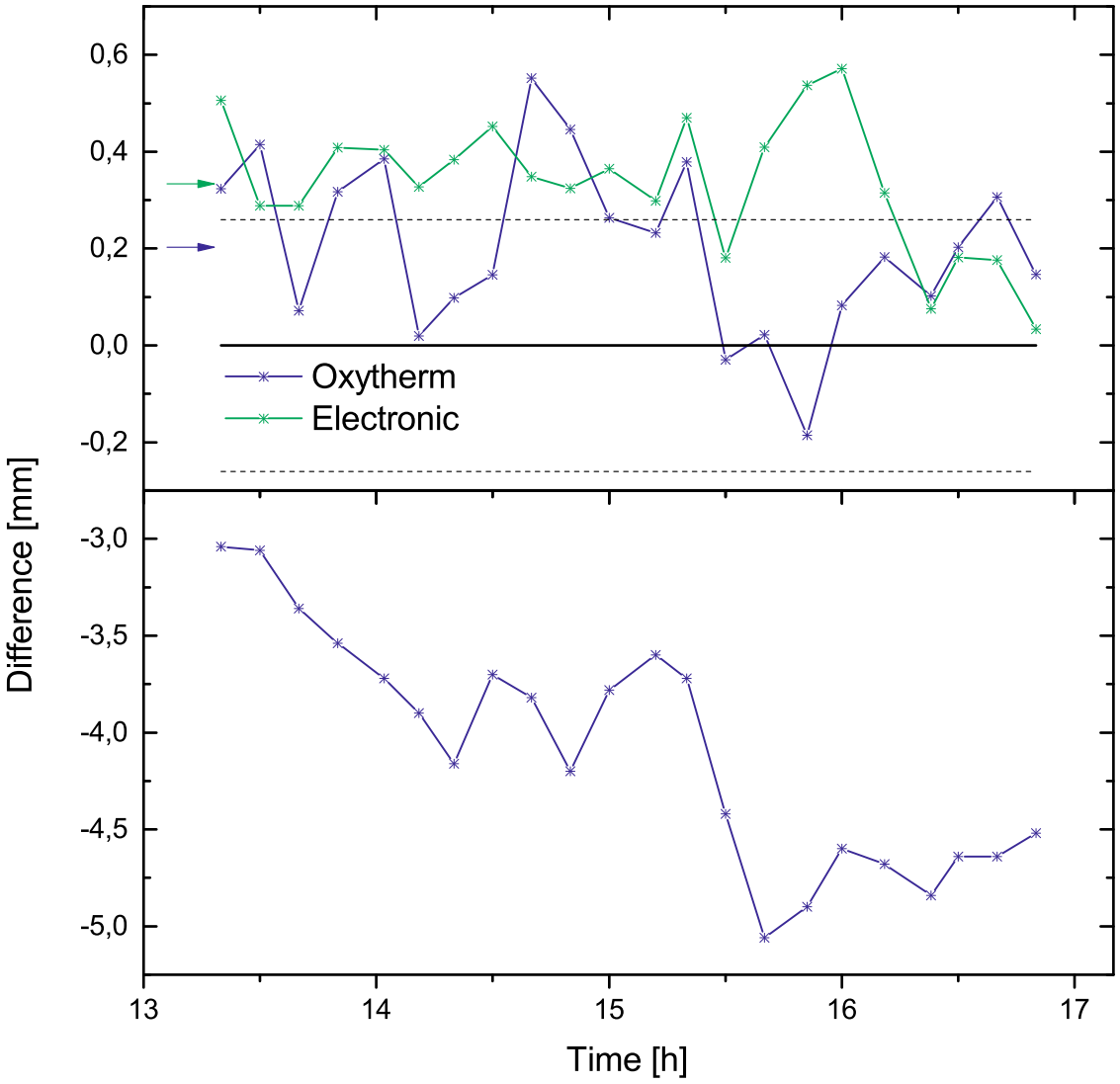

Figure D2: Slope distances of the Nummela standard baseline on 864 m path length between observation pillars 0-864. The measurements were conducted on 30.9.2015 with Leica TC2003 tacheometer. The upper graph presents the difference of the calibrated slope distance to the corrected slope distances and the lower graph the difference to the uncorrected slope distances. The arrows indicate the mean values of the respective data. The dashed lines are the 95% confidence intervals of the calibrated slope distance.

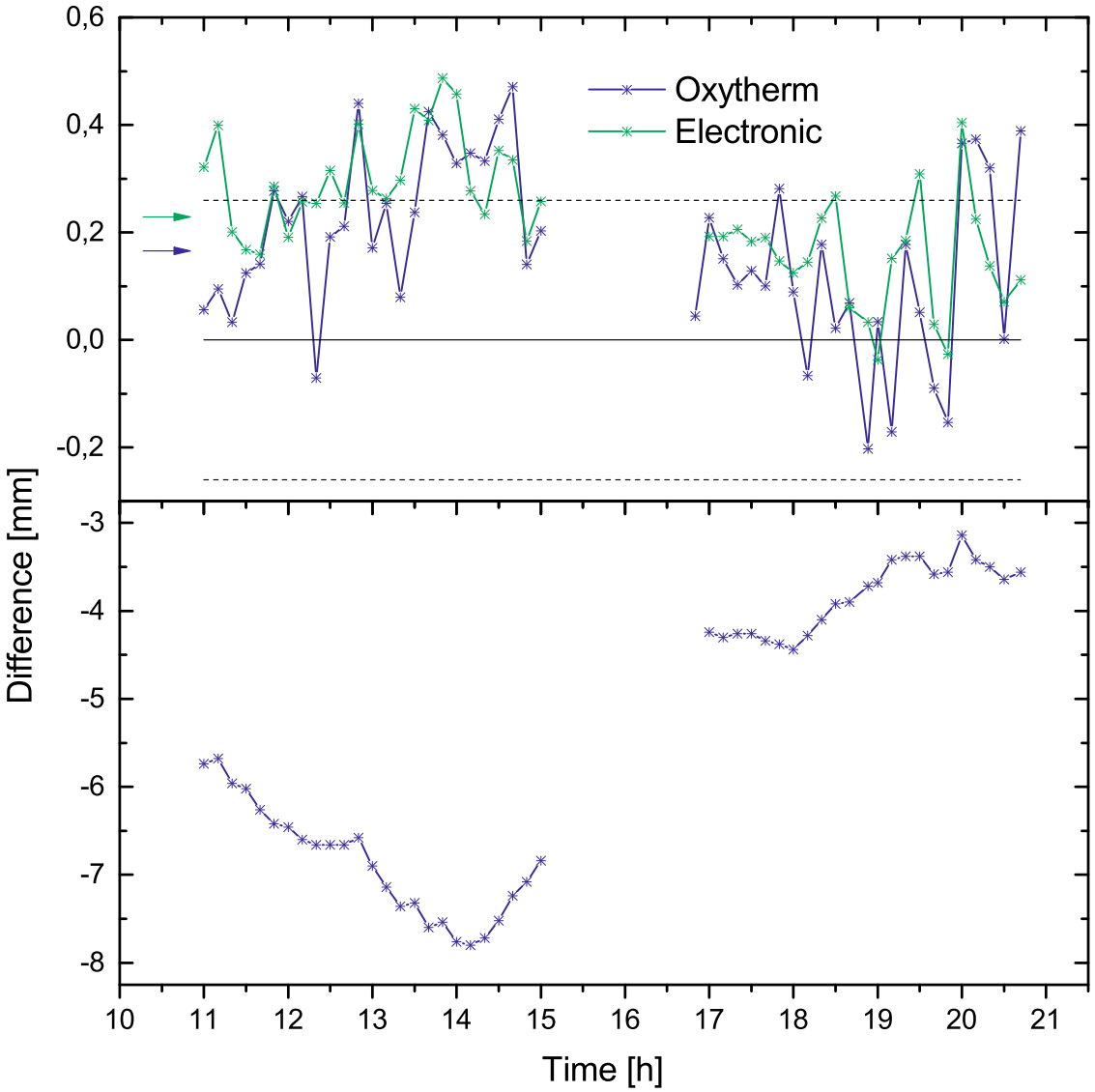

Figure D3: Slope distances of the Nummela standard baseline on 864 m path length between observation pillars 0-864. The measurements were conducted on 1.10.2015 with Leica TC2003 tacheometer. The upper graph presents the difference of the calibrated slope distance to the corrected slope distances and the lower graph the difference to the uncorrected slope distances. The arrows indicate the mean values of the respective data. The dashed lines are the 95% confidence intervals of the calibrated slope distance.